ALL-SOLID-STATE FRONT-ILLUMINATED TITANIA NANOTUBE-BASED DYE-SENSITIZED SOLAR-CELLS

LI KANGLE

B. Sci. (Hons.), NUS

A THESIS SUBMITTED

FOR THE DEGREE OF DOCTOR OF PHILOSOPHY

DEPARTMENT OF MATERIALS SCIENCE AND ENGINEERING

NATIONAL UNIVERSITY OF SINGAPORE

2012

Acknowledgment

First and foremost, I am heartily thankful to my supervisor, A/P Stefan Adams, whose encouragement, and support from the initial to the final level enabled me to develop an understanding of the project. I am grateful to his invaluable advice, support, detailed instructions and guidance throughout of years of my study. It is extremely pleasant to work with him.

I would like to express my utmost thanks to Dr. Xie Zhibin in giving me demonstrations and for his valuable guidance in support of my lab work. I would also like to express my gratitude to Dr. Wang Qing for the valuable advice on impedance fitting of dye-sensitized solar cells, Prof. John Wang and A/P Dan Blackwood for allowing me using their lab facilities. The support from the students and staffs in their research group is mostly appreciated.

I will take this opportunity to appreciate the friendship and support from my group colleagues Dr. Prasada Rao, Dr. Thieu Duc Tho, Dr. Zhou Yongkai, Chen Maohua, Gu Wenyi and To Tran Thinh. I would also like to extend my thanks to other friends Mei Xiaoguang, Fan Benhu, Cho Swee Jen, Neo Chin Yong, Sun Kuan, Sun Jian, and Dr. Zhang Hongmei.

Last, but not least, I am especially grateful to my family members for their unconditional love, encouragement and support.

Table of Contents

Summary

The thesis aims to provide a systematic study of fabricating and characterizing front-illuminated titania nanotube-based dye-sensitized cells with a focus on all-solid state heterojunction cells. By the time I started this project, the fabrication techniques of back-illuminated nanotube-based dye-sensitized solar cells were well developed, and some pioneering works have been undertaken on producing an all-solid-state nanoparticle-based dye-sensitized heterojunction cell. In order to achieve my project goals, I have developed a novel and highly reliable method to transfer nanotubular TiO_2 structures onto FTO, and used this unique structure for the application in all-solid-state dye-sensitized solar cells. A highly efficient and stable solid state solar cell could finally be achieved by solution casting of CuSCN-based hole-conducting materials (HTM) into this nanotube array. Optimisation of the conductivity by Ni^{2+} doping and of the pore penetration via additives controlling the CuSCN particle size proved essential for the favourable performance of the produced solar cells. Front-illuminated nanotube-based dye-sensitized solar cells (FI-NT-DSCs) and solid-state heterojunction cells (FI-NT-SSDSCs) with light conversion efficiency up to 6.1% and 2% are fabricated respectively. The cell photovoltaic performance of FI-NT-SSDSC can last for at least two months with proper sealing technique.

The first chapter gives a historical perspective of the development of solar cell technologies including silicon-based and nanostructured solar cells over the past two centuries. Since the introduction of mesoporous nanoparticular titania by O'Regan and M. Grätzel in 1991, the optimization of dye-sensitized solar cells are investigated.

A record conversion efficiency of 12% was obtained. Dye-sensitized solar cell (DSC) is therefore one of the cost-effective alternatives to silicon-based solar cells. A replacement of nanoparticle photoelectrode by nanotube structure utilizes the unique nanotube texture with excellent charge transport property along tube length direction without sacrificing effective light absorption area. Moreover, well-ordered and vertically oriented structure is beneficial for pore-filling when solution casting method is applied to introduce solid-state hole transporting medium. Other than that, a higher charge collection efficiency of titania nanotube, which can mitigate the fast recombination process, is another motivation to replace nanoparticles in all-solid-state dye-sensitized solar cells (SSDSCs).

The fundamental theory employed in the fabrication and characterisation of NT-SSDSCs is summarized in Chapter 2, explaining the key terms and parameters used in dye-sensitized solar cells study. This includes a discussion of nanotube growth and detachment mechanisms, as well as a brief summary on the theory of impedance spectroscopy and equivalent circuit models used to fit DSCs.

The experimental section (chapter 3) contains the essence of my hand-on experience in fabricating dye-sensitized solar cells that are not mentioned in published papers typically. Besides an overview of the employed characterisation techniques, it basically includes the recipes for preparation of photoelectrode and hole-transporting medium, as well as dye-loading and cell assembly developed or refined in the course of the project. This is the part where I spent most of the time in my PhD project.

Chapter 4 presents my results on titania nanotube growth by anodizing a Ti foil. This comprises a systematic study on how anodization conditions, electrolyte composition and post-anodization treatment influence the morphology of the fabricated titania nanotube arrays. These nanotube arrays then act as photoelectrode in dye-sensitized solar cells. Using nanotube arrays as grown on Ti foils restricts the solar cell design to back-illuminated cells with their efficiency reduced by light absorption and scattering in the electrolyte or hole-conductor. To make full use of unique nanotube structure, two types of front-illuminated DSCs are produced as described in this chapter: In the first approach Ti thin films are sputtered on TCO followed by anodization, while the second – more successful – approach is based on the detachment and transfer of nanotube membranes from Ti foil to TCO.

Chapter 5 focuses on the optimization of the CuSCN hole-conductor for the SSDSCs. Additives or dopings such as triethylammonium thiocyanate (THT), α-CuSCN and $Ni(SCN)_2$ greatly improves the conductivity and/or pore-filling of the hole-transporting medium into the mesoporous anatase nanostructures. The significant role of THT additive is prominent in cell stability test. The optimized solution is cast into nanotube to make front-illuminated nanotube-based dye-sensitized heterojunction cell. The Al_2O_3 coating and length effect on cell performance and stability over 2 months are also studied.

List of Tables

List of Figures

List of Abbreviations

AN	Acetonitrile
CV	Cyclic voltammetry
DSC	Dye-sensitized solar-cells
EG	Ethylene glycol
EIS	Electrochemical impedance spectroscopy
FI-NT-DSC	Front-illuminated nanotube-based dye-sensitized solar cell
FI-NT-SSDSC	Front-illuminated nanotube-based solid-state dye-sensitized heterojunction cell
HTM	Hole-transporting medium
IPCE	Incident photon-to-electron conversion efficiency
IPA	Iso propyl alcohol
GAXRD	Grazing angle X-ray diffraction
NP	Nanoparticle
N3	cis-bis(isothiocyanato)bis(2,2'-bipyridyl-4,4'-dicarboxylato)-ruthenium(II)
N719	$RuL_2(NCS)_2$:2TBA (L = 2,2'-bipyridyl-4,4'-dicarboxylic acid)
NT	Nanotube
PS	Dipropyl sulfide = 1-(Propylsulfanyl)propane
PMII	3-methyl-1-propyl imidazolium iodide
SSDSC	All-solid-state dye-sensitized solar-cells
SEM	Scanning electron microscopy
STC	Standard testing condition, AM1.5, 1 sun illumination
TCO	Transparent conducting oxide
TIP	Titanium isopropoxide
tBP	tert-butyl-pyridine
THT	Triethylammonium thiocyanate (originally termed Triethylamine hydrothiocyanate)
VN	Veronitrile
XRD	X-ray diffraction

List of Symbols

C_{sc}	Space charge capacitance
C_{μ}	Chemical capacitance
D_{amb}	Ambipolar diffusion coefficient
e	Charge of an electron
f(E)	Fermi-Dirac distribution function
g(E)	Distribution of trap states
R_{ct}	Charge transfer resistance
R_t	Charge transport resistance
N_A	Avogadro constant
N_d	Dopant concentration
ε_0	Permittivity
V_{fb}	Flat band potential
k_B	Boltzmann constant
T	Temperature
E_c	Conduction band edge energy
μ_n	Electrochemical potential
ΔG	Activation Energy
F	Faraday's constant
R	Molar gas constant
k_{ox} /k_{red}	Charge transfer constant of oxidation or reduction process
τ_n	Electron life time
m_c	Characteristic energy of the exponential trap state distribution
L_n	Effective diffusion coefficient
J_{00}	Dark exchange current density per unit film thickness
T_{TCO}	Effective transmittance of the TCO substrate
ϕ	Incident photon flux
rpm	Rounds per minute

Chapter 1 *Introduction*

1.1 Solar cells

Since the second industrial revolution in 1870s, electronic devices are widely used in our daily life. Electricity as the major energy source becomes more and more demanding. It is hard to imagine life without electricity when mankind gets used to enjoying all the convenience it brings to us. At the same time, we certainly cannot forget the lesson learnt from Chernobyl and Fukushima-ken disasters. Until a proper and safe way is developed to utilize nuclear energy, other more clean, safe and sustainable energy forms are favourable. As an important sustainable energy source, photovoltaic energy conversion will become indispensable in the future. [1]

Photovoltaic (PV) is a method of generating electrical power by converting solar radiation into direct current electricity using semiconductors that exhibit the photovoltaic effect, i.e. the creation of a potential (or a corresponding electric current) in a material upon exposure to light. The photovoltaic effect was first observed by Alexandre-Edmond Becquerel in 1839. A brief history of photovoltaic solar energy conversion technology is given in Table 1-1 [2]. Though the photovoltaic effect is directly related to the photoelectric effect, the two processes are different and should be distinguished. In the photoelectric effect, electrons are ejected from a material's surface upon exposure to radiation of sufficient energy. The photovoltaic effect is different in that the generated electrons are transferred between different bands (i.e.,

from the valence to conduction bands) within the material, resulting in the buildup of a potential between two electrodes. In most photovoltaic applications the radiation is sunlight and for this reason the devices are known as solar cells. Photovoltaic power generation employs solar panels composed of a number of cells containing a photovoltaic material. Due to the growing demand for renewable energy sources, the manufacturing of solar cells and photovoltaic arrays has advanced considerably in recent years.

Table 1-1: History of photovoltaic solar energy conversion. Adapted from T. Markvart [3]

1839	Becquerel discovers the photo galvanic effect
1873	Smith observes photo conducting effect in selenium
1876	Adams and Day observe photovoltaic effect in selenium
1900	Planck postulates the quantum nature of light
1930	Quantum theory of solids proposed by Wilson
1940	Mott and Schottky develop the theory of solid state rectifier (diode)
1949	Bardeen, Brattain and Shockley invent the transistor
1954	Chapin, Fuller and Pearson announce a solar cell efficiency of 6% in silicon solar cells
1958	First use of solar cells on an orbiting satellite Vanguard

Standard single crystal silicon solar cells usually consist of a p-n junction structure. A depletion region at the junction is balanced by the concentration gradient of charge carriers. Local electrochemical equilibrium is therefore established. At this moment, the solar cell functions as a diode. While the load is present, the potential bias creates a current which is exponentially dependent on bias. This effect is named as dark current for solar cells without sunlight. For an ideal diode, when the light is shining on the solar cell, it could transmit through the materials, get reflected or be absorbed depending on the wavelength of the light. In a p-n junction, an electron-hole

pair is excited when light is absorbed by the material. Therefore, the photocurrent generated by a solar cell under illumination at short circuit condition is controlled by the incident light intensity. Fig. 1-1a shows a typical equivalent circuit of an ideal solar cell: The output current is related to photo-generated current as well as to the dark current and leakage current passing through shunt resistance. Hereby, the equivalent circuit could be interpreted and current vs. voltage (IV) curve is expressed in equation 1.1.

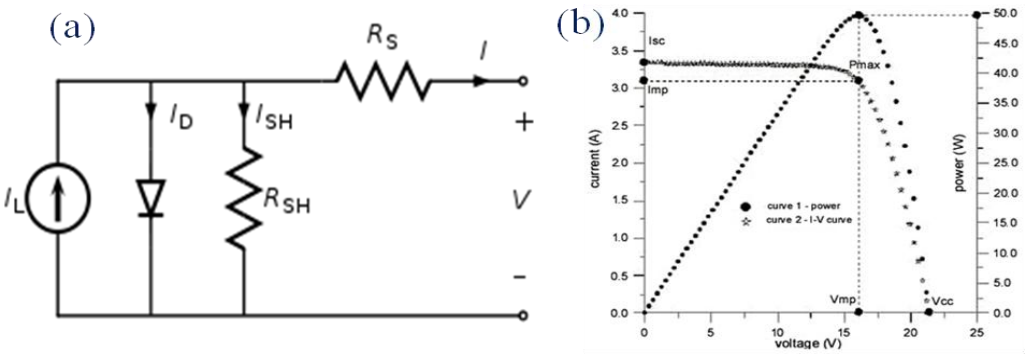

Figure 1-1: (a) Equivalent circuit of an ideal solar cell. [1] I_L is photo-current; I_D refers to diode forward current. R_{SH} is shunt resistance. R_s is series resistance; (b) A typical IV curve of a Si-based solar cell module measured under 1 sun illumination. The cell light conversion efficiency is defined as the ratio between maximum output power and input power.

$$I = I_L - I_0\left\{\exp\left[\frac{q(V+IR_S)}{nkT}\right] - 1\right\} - \frac{V+IR_S}{R_{SH}} \qquad (1.1)$$

If the output voltage is V and series resistance is R_s, the voltage cross diode and shunt resistance would be consistent and equals to $V+ I\cdot R_s$. This formula demonstrates the I-V characteristic of solar cell under illumination including the effect of series and shunt resistance on I-V curve. Generally, the efficiency of a solar cell is determined by the ratio of maximum output power to input power. The standard terrestrial solar spectrum is defined as the AM 1.5 spectrum normalized so

that the integrated irradiance is 100 mW/cm^2, where air mass is defined as the optical path length to sun divided by the optical path length if the sun is directly overhead. Ideally upon illumination, open-circuit voltage of a solar cell is defined as the measured voltage when current flow tends to be zero, while short-circuit current is the current flow without bias potential. A maximum output power of the cell could be observed as load voltage scans from short circuit to open circuit condition. The J_{mp} and V_{mp} should be very close to J_{sc} and V_{oc} so as to obtain a large fill factor (FF) which describes the squareness of the curve and is simply defined as $FF=J_{mp}V_{mp}/J_{sc}V_{oc}$. (see Fig. 1-1b)

1.2 Dye-sensitized solar cells (DSC)

The success of the first chemical syntheses of dyes, such as mauveine, alizarin or indigo, induced the development of the chemical industry in the second half of the 19^{th} century. In 1837, Daguerre made the first photographic images, introducing at the same time the idea to use light for the storage of information. With the following development of colour photography, the importance of the control of energetic and spectral properties of dyes became evident. At the same time, the role of chlorophyll in photosynthesis demonstrated the potential of dyes for harvesting of energy from sunlight. The dream to capture the free energy available from sunlight by the intermediate of dyes to produce electricity or chemical fuels (such as hydrogen) motivates more and more scientists to study on photovoltaic device for many decades.[4]

In 1960s, the mechanism of dye sensitization was first clearly understood: the electron injection from a photo-excited state of the dye molecule into the conduction band of the n-type semiconductor makes it possible to convert light energy into electric energy (DSC) or information (photograph) [5, 6],. Following the work of Namba and Hishiki, [7] Tributsch and Gerischer et al. [8, 9, 10] on zinc oxide, the efficiency (~0.1%, a typical output power of 125 $\mu W/cm2$) is limited by the poor dye anchorage (mostly physisorbed) and weak light absorption (in the order of 1 to 2%) of the dye monolayer on the planar surface. Thicker dye layers increased the resistance of the system without adding to the current generation.

At that time most of the studies involved electrochemical measurements of sensitized photocurrents at single-crystal wide-bandgap semiconductor electrodes. While these early studies set the theoretical framework, the real breakthrough was achieved by O'Regan and Grätzel who used nanocrystalline TiO_2 electrodes in 1990. [11] With such mesoporous films the effective surface for sensitizer adsorption was roughly 1000 times that of a planar electrode. The material of choice has been anatase although alternative wide band gap oxides such as ZnO and Nb_2O_5 have also been investigated. The energy level of conductive band should match with lowest unoccupied molecular orbital (LUMO) level of the dye molecules so as to allow electron injection into anatase. A wide band gap favours suppression of charge recombination. Additionally, the fast charge transport ought to balance out the electron loss due to recombination. [11] Soon, dye-sensitized solar cells based on this concept yielded promising solar-to-electricity conversion efficiencies. [4,12]

The dye-sensitized solar cells proved a technically and commercially

promising alternative concept to replace the thin-film solar cell. Charge separation and light absorption take place in two different materials. The dye sensitizer absorbs light and therefore injects the excited electron to mesoporous semiconductor. Charge separation is fulfilled at the interface of dye and wide band gap semiconductor. Nearly quantitative conversion of incident photon into electric current is achieved over a large spectral range extending from the UV to the near IR region. Overall solar to current conversion efficiencies exceeding 10% have been achieved. [13] The dye-sensitized solar cell (DSC) is therefore one of the cost-effective alternatives to silicon-based solar cells. A replacement of nanoparticle photoelectrode by nanotube structure utilizes the unique nanotube texture with excellent charge transport property along tube length direction without sacrificing effective light absorption area. Moreover, well-ordered and vertically oriented structure is beneficial for pore-filling when solution casting method is applied to introduce solid-state hole-transporting medium. Other than that, a higher charge collection efficiency of titania nanotube, which can mitigate the fast recombination process, is another motivation to replace nanoparticles in all-solid-state dye-sensitized solar cells (SSDSCs). To understand the advantage of front-illuminated nanotube-based solid-state dye-sensitized solar cells, a brief introduction of titania nanotube and inorganic hole-transporting medium is given in the subsequent subsections.

1.2.1 Nanotube on transparent conductive glass

TiO_2 nanotubes arrays have been produced by a variety of methods. These include: using a template of nanoporous alumina [14–16], sol-gel transcription processes using

organogelator templates [17,18], seeded growth mechanisms [19], and hydrothermal techniques [20-22]. Anodization of Ti in a fluoride-based electrolyte offers superior control over the nanotube dimensions when compared to previous methods. [23–26]

In 1999, *Zwilling et al.* achieved self-organized porous TiO_2 by anodizing a Ti-based alloy in an acidic, fluoride-based electrolyte [27,28]. In 2001, *Gong et al.* fabricated self-organized, highly uniform TiO_2 nanotube arrays by anodizing Ti in an aqueous dilute HF electrolyte [29,30]. The maximum length of nanotube arrays in the first synthesis generation was approximately 500 nm. In subsequent work, the second-generation, the nanotube array length was increased to approximately 7 μm by proper control of the anodization electrolyte pH thereby reducing the chemical dissolution of TiO_2 during anodization [31,32]; the pH should be high but remain acidic (~5.5). In later work, the third-generation, TiO_2 nanotube arrays with lengths of up to approximately 1000 μm were achieved using a non-aqueous, polar organic electrolyte such as formamide, dimethylsulfoxide, ethylene glycol or diethylene glycol [23,33].

With a titanium anode and a platinum cathode immersed in an aqueous electrolyte of dilute acid to which a small dc potential is applied the surface layer is sufficiently resistive to prevent current flow. Increasing the applied potential produces no additional current flow until a threshold level is reached where the electric field intensity within the barrier is sufficient to force oxygen ions to diffuse across it, producing an ionic current. These oxygen ions react with the metal and increase the thickness and/or density of the oxide barrier. This process of high-field ionic conduction is central to anodization. Of course, the same process liberates

hydrogen gas from the cathode. Since the electrical resistance of the layer increases in proportion to its thickness and since the rate of oxide growth is proportional to the current density, the thinner portions of the layer carry more current than the thicker ones. Hence, a thin section grows faster than a thick one, creating an even more uniform layer. [34]

By controlling the various anodization parameters it is possible to vary the tube-to-tube connectivity and hence packing density of the nanotubes within an array. Maximum nanotube packing density is achieved using an ethylene glycol electrolyte; the nanotube coordination number is usually six, i.e. each nanotube is surrounded by six others, with strong bonding between adjacent tubes. This structure is most useful for achieving a mechanically robust, i.e. non-fragile, membrane of uniform pore size suitable for use in filtration applications [35,36]. This inspired the first method of detaching anodized nanotube membrane so as to use as the photoelectrode in front-illuminated nanotube-based dye-sensitized solar cells.

Pioneering works have been done by *Grimes et al.* who used an electrolyte composition of 0.3 wt% ammonium fluoride and 2 vol% water in ethylene glycol for membrane fabrication. Anodization is done at room temperature with a platinum foil cathode. A nanotube about 220 μm long with pore size 125 nm and standard deviation of 10 nm resulted when anodization was performed at 60 V for 72 h. The as-anodized samples were then dipped in ethyl alcohol and subjected to ultrasonic agitation until the nanotube array film separated from the underlying Ti substrate. The compressive stress at the barrier layer-metal interface facilitates detachment from the substrate.

Figure 1-2: A stable, mechanically robust nanotube array membrane after critical point drying. The 200 µm thick membrane, 120 nm pore diameter, is about 2.5 cm × 4.5 cm [35]

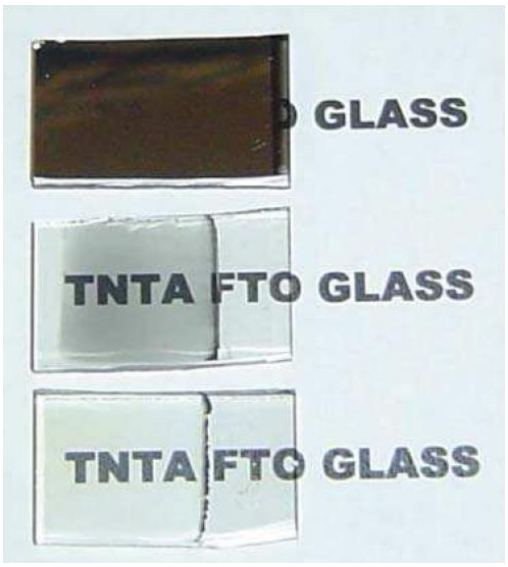

Figure 1-3: Key stages in the fabrication of a transparent nanotube array by sputtering method, Ti films on FTO (top); NT film after anodization (middle); NT film after heat treatment (bottom). [37]

The planar membranes are perfectly flat while wet but significantly curl after removal from the liquid and dried in air. This makes them unsuitable for filtering applications. Since the surface tension forces of the solution acting on the membrane were mainly responsible for this behaviour, rinsing with low surface tension liquids facilitates their drying flat. Alternatively, freeze drying can be used in which the membrane flatness

is preserved, see Fig. 1-2. The figure shows a 200 μm thick membrane after critical point drying. The surface of the membrane after drying in this way occasionally shows a nanofiber surface; it can be removed by subjecting the membrane to ultrasonic agitation. However, such a membrane is too thick and therefore not suitable for dye-sensitized solar cells application.

Another method that has been developed for fabrication of TiO_2 nanotube arrays from sputtered Ti thin film on FTO in Fig. 1-3. Deposition of a high quality Ti is crucial for growing nanotube arrays from sputtered Ti film. Usually, anodization of a single-layer film would break the electrical contact with the submerged portion of the Ti as the metal layer at the electrolyte/air interface reacts faster. Therefore, an additional protective underlayer is essential to avoid this problem.

In this thesis, an independently developed method is given to fabricate front-illuminated nanotube-based DSCs. The advantage of our approach is that the reliable method is highly reproducible, providing an intact membrane without destroying the tubular structure and an extreme flexibility on tuneable length.

1.2.2 All-solid-state dye-sensitized heterojunction cells

Solid-state dye-sensitized solar cells (SSDSC) are promising due to their large potential to convert solar energy to electrical energy at low cost and their capability to solve the degradation, sealing and leakage problems that exist in liquid electrolyte dye-sensitized solar cells. [38] A typical SSDSC consists of several different material layers: a compact TiO_2 layer, a dye adsorbed mesoporous nano-crystalline on optically transparent electrodes, solid organic or inorganic p-type layer (hole-

transporting medium: HTM) and a gold or graphite counter electrode. Fig. 1-4 shows the schematic representation of a SSDSC and the chemical structures of the standard dye and HTM.

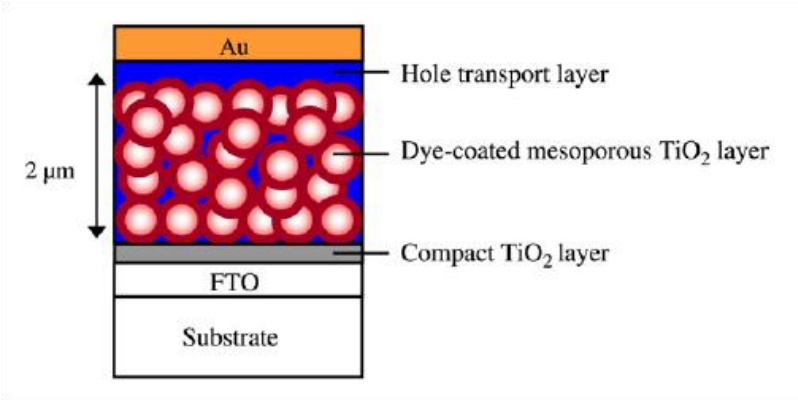

Figure 1-4: A schematic representation of a solid-state dye-sensitized solar cell showing the different components and layers. [39]

The first few demonstrations on SSDSC were based on inorganic p-type semiconductors such as CuI and CuSCN [40,41]. A typical CuSCN-based SSDSC reaches reasonably good power conversion efficiencies of about 2%. Recently, Bandara and Weerasinghe reported a first study on SSDSC using p-type NiO (V_{oc}= 480 mV, J_{sc}= 0.15 mA/cm^2, FF= 47.6%, η= 0.03%.) [42] However, the power conversion efficiencies of SSDSCs employing these inorganic hole-conductors are lower than liquid electrolyte DSSC at 1 Sun (100 mW/cm^2). This is due to the following reasons: (i) poor wetting or electrical contact between dye and HTM, (ii) high recombination between TiO_2 and HTM, (iii) low hole mobility of HTM, and (iv) incomplete penetration of HTM into the pores of nanocrystalline-TiO_2 layer. Among these disadvantages, poor pore-filling of hole-conductor into TiO_2 layer is considered as the most significant issue to solve. For instance, CuI-based SSDSCs are not very

stable. One of the reasons for the degradation is that stoichiometric excessive iodine absorbed at the CuI surface strongly decreased the photocurrent. [43] The other reason is the loosening of the contact between the dye-coated TiO_2 and CuI crystallites. Regarding to pore-filling and stability, it is found that the stability of the CuI-based DSC can be greatly improved by incorporation of 10^{-3} M of 1-methyl-3-ethyl imidazolium thiocyanate (EMISCN) in the coating solution. [44] EMISCN acts as a CuI crystal growth inhibitor and it remains at the interface between CuI and TiO_2. *Tennakone et al.* [45] also found that the simple substance triethylammonium thiocyanate (THT) was more effective than EMISCN in suppressing crystal growth.

An alternative hole-conductor CuSCN has more stable performance. *Kumara et al.* [46] found that CuSCN can be deposited from a solution in n-propylsulphide (PS). In 2002, *O'Regan et al.* [47] reported a more reproducible method of fabricating CuSCN-based SSDSC with a much better pore-filling by using a more diluted CuSCN PS solution. The TiO_2 nanoparticular cells with an optimum thickness of 5 μm showed an efficiency of ~2% under standard testing conditions (STC, 100 mW/cm^2 at 1.5 AM). In order to further improve the pore-filling and light conversion efficiency of the cell, a study of front-illuminated nanotube-based all-solid-state dye-sensitized heterojunction cell is motivated, so as to utilize the advantage of nanotube. A well-defined electron pathway and V-shape tunnel allows easy-filling for hole-transporting medium. After optimization of conductance and pore-filling, this type of SSDSC should show promising future as the device exhibits good charge collection efficiency, and long term stability without leakage issue. (A proper sealed cell shows a stable performance over two months, details are given in chapter 5)

References

1 P. Würfel, Physics of solar cells：from principles to new concepts. @ 2005 WILEY-VCH Verlag GmbH & Co. KGaA, Weinheim ISBN 3-527-40428-7.

2 A. Eppler, Thesis "Charge Transport in Nanocrystalline Titanium Dioxide and its Use in Solar Cells". Experimental Solid State Physics Group, Blackett Laboratory, Imperial College London, University of London YEAR.

3 T. Markvart, Solar Electricity. John Wiley and Sons, 2nd edition, 2000.

4 J. R. Jennings, PhD thesis, Departments of Chemistry and Physics, University of Bath YEAR.

5 R. C. Nelson, J. Phys. Chem. 1965, 69, 714.

6 J. Bourdon, J. Phys. Chem. 1965, 69, 705.

7 S. Namba, Y. Hishiki, J. Phys. Chem. 1965, 69, 774.

8 H. Gerischer, H.Tributsch, Ber. Bunsenges. Phys. Chem. 1968, 72, 437.

9 H. Gerischer, H.Tributsch, Ber. Bunsenges. Phys. Chem. 1969, 73, 251.

10 H. Gerischer, Electroanal. Chem. Interfac. Electrochem. 1975, 58, 263.

11 B. O'Regan, M. Grätzel, Nature 1991, 335, 737.

12 Z. P. Zhang, PhD thesis "Enhancing the Open-Circuit Voltage of Dye-Sensitized Solar Cells: Co-adsorbents and Alternative Redox Couples" EPFL, 2008.

13 M. Grätzel, J. Photochem. and Photobio. C: Photochem. Rev. 2003, 4, 145.

14 P. Hoyer, Langmuir 1996, 12, 1411.

15 B. B. Lakshmi, P.K. Dorhout, C.R. Martin, Chem. Mater. 1997, 9, 857.

16 H. Imai, Y. Takei, K. Shimizu, M. Matsuda, H. Hirashima, J. Mater. Chem. 1999, 9, 2971.

17 J. H. Jung, H. Kobayashi, K. V. Bommel, S. Shinkai, T. Shimizu, Chem. Mater. 2002, 14, 1445.

18 S. Kobayashi, N. Hamasaki, M. Suzuki, M. Kimura, H. Shirai, K. Hanabusa, J. Am. Chem. Soc. 2002, 124, 6550.

19 Z. Tian, J. A. Voigt, J. Liu, B. McKenzie, H. Xu, J. Am. Chem. Soc. 2003, 125, 12384.

20 T. Kasuga, M. Hiramatsu, A. Hoson, T. Sekino, K. Niihara, Langmuir 1998, 14, 3160.

21 Q. Chen, W. Zhou, G. Du, L. Peng, Adv. Mater. 2002, 14, 1208.

22 B. Yao, Y. Chan, X. Zhang, W. Zhang, Z. Yang, N. Wang, Appl. Phys. Lett. 2003, 82, 281.

23 C. Ruan, M. Paulose, O. K. Varghese, C. A. Grimes, Sol. Energy Mater. Sol. Cells 2006, 90, 1283.

24 J. M. Macak, H. Tsuchiya, P. Schmuki, Angew. Chem. Int. Ed. 2005, 44, 2100.

25 E. Balaur, J. M. Macak, H. Tsuchiya, P. Schmuki, J. Mater. Chem. 2005, 15, 4488.

26 J. M. Macak, P. Schmuki, Electrochim. Acta 2006, 52, 1258.

27 V. Zwilling, M. Aucouturier, E. Darque-Ceretti, Electrochim. Acta 1999, 45, 921.

28 V. Zwilling, E. Darque-Ceretti, A. Boutry-Forveille, D. David, M. Y. Perrin, M. Aucouturier, Surf. Interface Anal. 1999, 27, 629.

29 D. Gong, C. A. Grimes, O. K. Varghese, W. Hu, R. S. Singh, Z. Chen, E. C. Dickey, J. Mater. Res. 2001, 16, 3331.

30 G. K. Mor, O. K. Varghese, M. Paulose, N. Mukherjee, C. A. Grimes, J. Mater. Res. 2003, 18, 2588.

31 Q. Cai, M. Paulose, O. K. Varghese, C. A. Grimes, J. Mater. Res. 2005, 20, 230.

32 J. M. Macak, H. Tsuchiya, L. Taveira, S. Aldabergerova, P. Schmuki, Angew. Chem. Int. Ed. 2005, 44, 7463.

33 M. Paulose, K. Shankar, S. Yoriya, H. E. Prakasam, O. K. Varghese, G. K. Mor, T. J. Latempa, A. Fitzgerald, C. A. Grimes, J. Phys. Chem. B 2006, 110, 16179.

34 C. A. Grimes, G. K. Mor, TiO_2 nanotube arrays: synthesis, properties and applications. Springer, Dordrecht, Heidelberg, London, New York, DOI 10.1 1007/9781-4419-0068-5.

35 M. Paulose, H. E. Prakasam, O. K. Varghese, L. Peng, K. C. Popat, G. K. Mor, T. A. Desai, C. A. Grimes, J. Phys. Chem. C 2007, 111, 14992.

36 J. Wang, Z. Lin, Chem. Mater. 2008, 20, 1257.

37 G. K. Mor, K. Shankar, M. Paulose, O. K. Varghese, C. A. Grimes, Nano Lett. 2006, 6, 215.

38 B. O'Regan, M. Grätzel, Nature 2001, 414, 338.

39 C. S. Karthikean, M. Telakkat, Inorganica Chimica Acta 2008, 361, 635.

40 K. Tennakone, G. Kumara, A. Kumarasinghe, K. Wijayantha, P. M. Sirimanne, Semicond. Sci. Technol. 1995, 10, 1689.

41 B. O' Regan, D. Schwartz, J. Appl. Phys. 1996, 80, 4749.

42 J. Bandara, H. Weerasinghe, Sol. Energ. Mat. Sol. Cells 2005, 85, 385.

43 V. Perera, K. Tennakone, Sol. Energy Mater. Sol. Cells 2003, 79, 249.

44 G. Kumara, A. Konno, K. Shiratsuchi, J. Tsukahara, K. Tennakone, Chem. Mater. 2002, 14, 954.

45 G. Kumara, S. Kaneko, M. Okuya, K. Tennakone, Langmuir 2002, 18, 10493.

46 G. Kumara, A. Konno, G. Senadeera, P. Jayaweera, D. De Silva, K. Tennakone, Sol. Energy Mater. Sol. Cells 2001, 69, 195.

47 B. O'Regan, F. Lenzmann, R. Muis, J. Wienke, Chem. Mater. 2002, 14, 5023.

Chapter 2 *Theory*

2.1 Nanotube growth

2.1.1 Candidate Metals

Transition metal oxides possess a wide range of functional properties based on their optical, chemical and electrical behaviours. A class of nanotubular materials based on transition metal oxides is studied due to a broad set of outstanding properties. Their applications are found in our daily life such as in biomedicine, as photochromic, chemical sensors and in photovoltaics. [1] Many of these oxides are of more practical value when their particle size is reduced to micro or nano range and hence their surface area increased. The morphologies produced include nanopowders, nanowires and nanotubes. Among the nanostructured transition metal oxides TiO_2 is one of the most intensively studied materials. Besides template-based, hydrothermal and sol-gel methods, the synthesis of self-ordering nanostructured TiO_2 by anodization received particular attention. The structures turned out to be tubular shape with tube length, wall thickness and inter-pore distance independently adjustable by anodization working conditions. The concept of growing nanotube arrays by this approach was successively applied to other valve metals such as Hf, [2] Nb, [3] Ta, [4] W, [5] Zr [6] and their alloys TiNb, [7] TiAl, [8] TiZr [9] or Ti_6Al_7Nb and Ti_6Al_4V. [10] The progressive increasing research interest on this field is shown in Fig. 2-1.

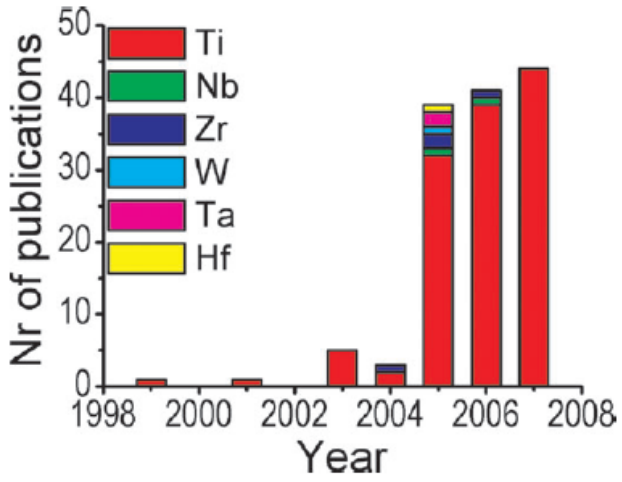

Figure 2-1: The number of articles published on valve metal oxide nanopore/nanotube layers formed by electrochemical anodization on different valve metals. [11]

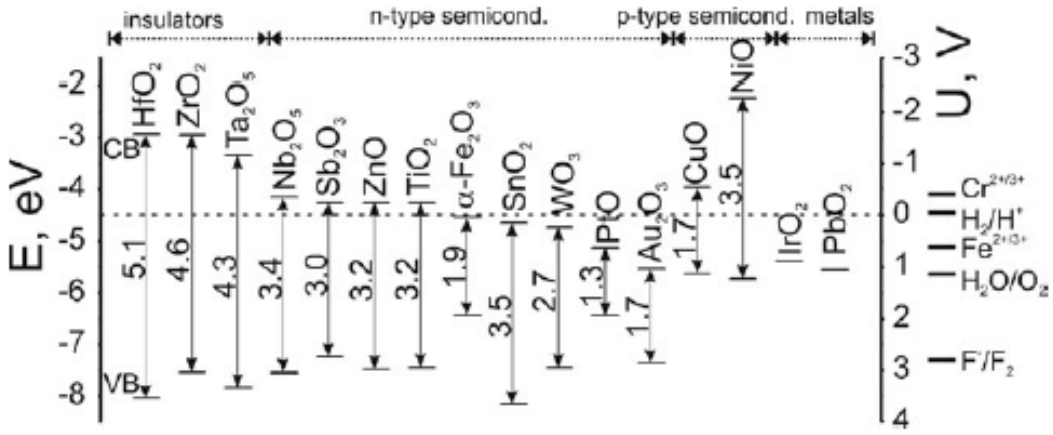

Figure 2-2: Electronic structure of different metal oxides and the relative position of their band edges vs. some key redox potentials. [11]

Generally the valve metal oxides can behave as insulators, conductors or semiconductors as outlined in Fig. 2-2. Most of them are intrinsic semiconductors with n-type behaviour. However, besides the band gap the relative band edge position or the electron kinetics are also important to judge the suitability of a material for a specific application. For instance, the photolysis of water requires the conduction band edge to be higher than the species to be reduced and the valence band edge to be

lower than the species to be oxidized. Another feature of transition metal oxides linked to the ionic properties of the materials is the ion intercalation, for example, H^+, Li^+. There would be a significant change in the electronic and optical properties of the material after intercalation.

A brief overview of types of application based on the electronic and ionic properties of these transition metal oxides is given in Table 2-1. In most of these applications the functional properties of the oxides are significantly improved by high surface area or short diffusion paths, thereby there is a promising potential to study the nanostructure (nanotube in my case) of these oxides.

Table 2-1: Some valve metal oxides and their application field [11]

Nanoporous oxides	Applications
TiO_2	DSCs, electrochromic windows, lithium batteries, photocatalyst
WO_3	Electrochromic windows, gas sensors
ZrO_2	Catalyst, solid electrolyte
Nb_2O_5	Electrochromic windows, gas sensors
Ta_2O_5	Biocompatibility, Capacitors
Al_2O_3	Templates, filters, magnetic devices, photonic devices

As many of above mentioned applications are related to the unique band structure and band bending at the interface between semiconductor and liquid electrolyte, some types of interface band diagrams are sketched in Fig. 2-3. As there is an excessive amount of electrons in an n-type semiconductor, electrons tend to

diffuse towards the semiconductor/electrolyte interface and to be transferred to electrolyte. This charge redistribution will cause an internal barrier that impedes further electron transfer leading to an equilibrium distribution. (See left diagram in Fig. 2-3) As seen from the band bending, the electron density inside the depletion zone is considerably reduced as the conduction band is effectively moved upwards with respect to the Fermi-level. At the same time, cations inside the electrolyte tend to accumulate at the surface of the semiconductor. An inner Helmholtz layer is formed to compensate the surface charge. Ions in the outer Helmholtz and an additional diffuse Gouy-Chapman layer ensure global charge neutrality. In the end, charge accumulated in the Helmholtz zone is equivalent to the one in the space charge zone inside the electrode. However, if the redox potential of the ions is above the Fermi-level in the solid, an accumulation layer would be formed instead. This will lead to some other applications, for example photoluminescence.

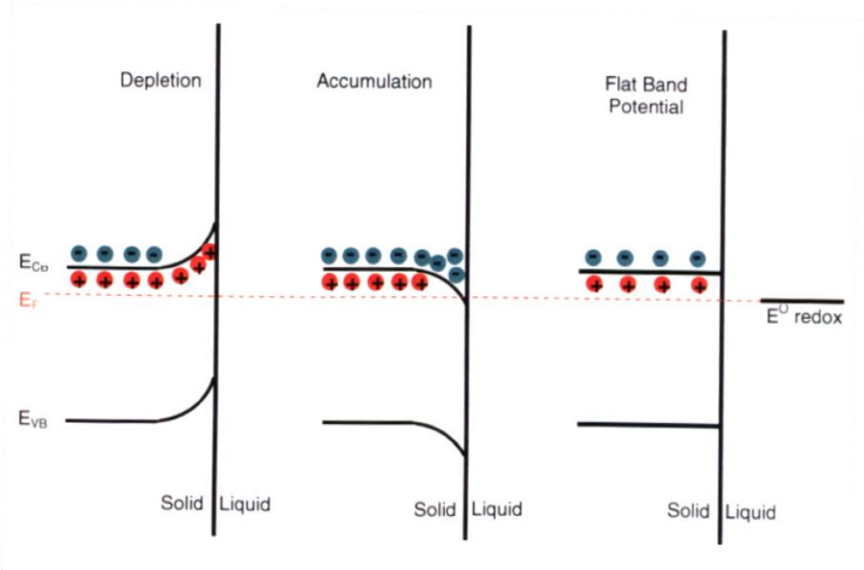

Figure 2-3: Depletion layer, accumulation layer and flat band for the interface of an n-type semiconductor to a liquid electrolyte. [12,13]

In the application of dye-sensitized solar cells, we take TiO_2 as an example. Under ambient oxygen partial pressure nominally pure TiO_2 is naturally n-doped: a small fraction 2δ of the Ti^{4+} will be reduced to Ti^{3+} and the charges are balanced by a slight oxygen deficiency in $TiO_{2-\delta}$. In the case of TiO_2 nanotubes created by anodization, the Ti'_{Ti} and $V_O^{\cdot\cdot}$ defects will be enriched near the surface of the nanotube. In this case, the capacitance of TiO_2 will be the summation of contribution from space charge C_{sc} and surface states C_{ss} since the capacitance of a Helmholtz layer is usually much larger than these two values.

Effectively, the capacitance of a TiO_2/electrolyte interface can be described as a linear summation of space charge capacitance and surface state capacitance. The cyclic voltammetry of a TiO_2 nanotube immersed in a KCl solution of 3 M reveals the capacitance contribution from both intrinsic and surface state properties.

On the right hand side in Fig. 2-3, a flat-band condition is shown. The value of the flat band potential as well as the corresponding dopant concentration can be determined by a Mott-Schottky plot. The Mott-Schottky equation [14]

$$C_{sc}^{-2} = \frac{2}{eN_d\varepsilon\varepsilon_0 A^2}\left(V_{app} - V_{fb} - \frac{k_B T}{e}\right) \tag{2.1}$$

is derived from Poisson's equation, which describes the variation of the potential created by a charged species with distance. Here C_{sc} is the capacitor from space charge zone, N_d represents dopant concentration, V_{app} is the applied potential, so we are able to find out position of flat band V_{fb} by extrapolating the curve of C_{sc}^{-2} vs. V_{app} and N_d by calculating the slope of the curve. $W_{sc} = (2V_{sc}\varepsilon\varepsilon_0/qN_d)^{1/2}$ and $C_{sc} = \varepsilon\varepsilon_0 A/W_{sc}$. The Mott-Schottky plot enables us to determine the flat band position, the nature of the semiconductor (n or p type) and the doping concentration.

2.1.2 Anodizing working conditions

Historically, the valve metal for which the growth of nanotubular oxide structures has been studied most extensively is Aluminium (Al) due to its industrial significance. It is generally accepted that anodization of Al in slightly acidic electrolytes leads to the formation of a porous oxide layer, [15] while under more neutral to alkaline conditions a compact layer is formed. Several models have been proposed in order to explain the growth mechanism and self-organization process. [16–19] Key factors that determined the occurrence of nanoporous/tubular structure are the electrolyte (pH), temperature, potential. [20] In contrast to aluminium, a low pH is not sufficient to create porous oxide layers on Ti, because of the very low solubility of Ti^{4+} in electrolytes under a low pH condition in the absence of complexing agents. Thus, besides a sufficiently acidic environment the electrolyte needs to contain a complexing agent that reacts with the metal ions and thereby promotes local oxide dissolution. This is achieved in the case of Ti anodization by adding F^-. A stable water-soluble $[TiF_6]^{2-}$ complex aids the local dissolution of the Ti-oxide layer formation at the tube bottom. Moreover, due to the small ionic radius, fluorides are able to enter the TiO_2 to participate in reaction at the metal-oxide interface. [21] By controlling electrolyte composition and anodization potential, nanotube wall thickness can be controlled in the range from 5 to 30 nm, the inner tube diameters from 20 to 350 nm, and tube length from 0.2 to 1000 μm. The aspect ratio (which is the tube length to outer diameter ratio) can thus be controlled from 10 to around 2000. In the next few paragraphs, three generations of anodization electrolyte will be

introduced together with their influences on the nanotube array morphology evolution.

The metal oxide produced by the first generation of the electrolyte (usually HF based aqueous solution) shares very similar structure with alumina nanoporous structure. Different types of acids were attempted such as HNO_3, [22] H_2SO_4, [23] $H_2Cr_2O_7$, [24] CH_3COOH [25] and H_3PO_4 [26] mixed with HF or NH_4F. The outer surface of this type of tube tends to be rough, and tube length is usually short as dissolution rate is fast in a low pH aqueous environment. The disadvantage of using this type of electrolyte is that the tubular structure is mechanically fragile; this limits the length of the tube and smoothness of the tube surface. Nevertheless, it is still a good demonstration that using fluoride in acidic environment is capable of fabricating self-organizing tube structure as first trials.

An important step forward from the first generation of the electrolyte is increasing pH value using NH_4F contained buffered electrolytes. Unlike alumina system, Ti forms complex ions with the aid of F^- even in a neutral environment. In other words, the chemical dissolution process is only suppressed but not eliminated when anodized in an electrolyte with a higher pH value. The great advantage is that the average tube length increases from 1 to 6 μm, and thereby greatly enhances the effective surface area. A representative study shows the variation of pH, potential and time affect tube length and pore diameter in Fig. 2-4. In short, larger potential, longer anodization time and higher pH will elongate the tube length independently within the anodization working conditions where there is a nanotube formation. (For instance, anodization time longer than an optimized period would shorten the tube length)

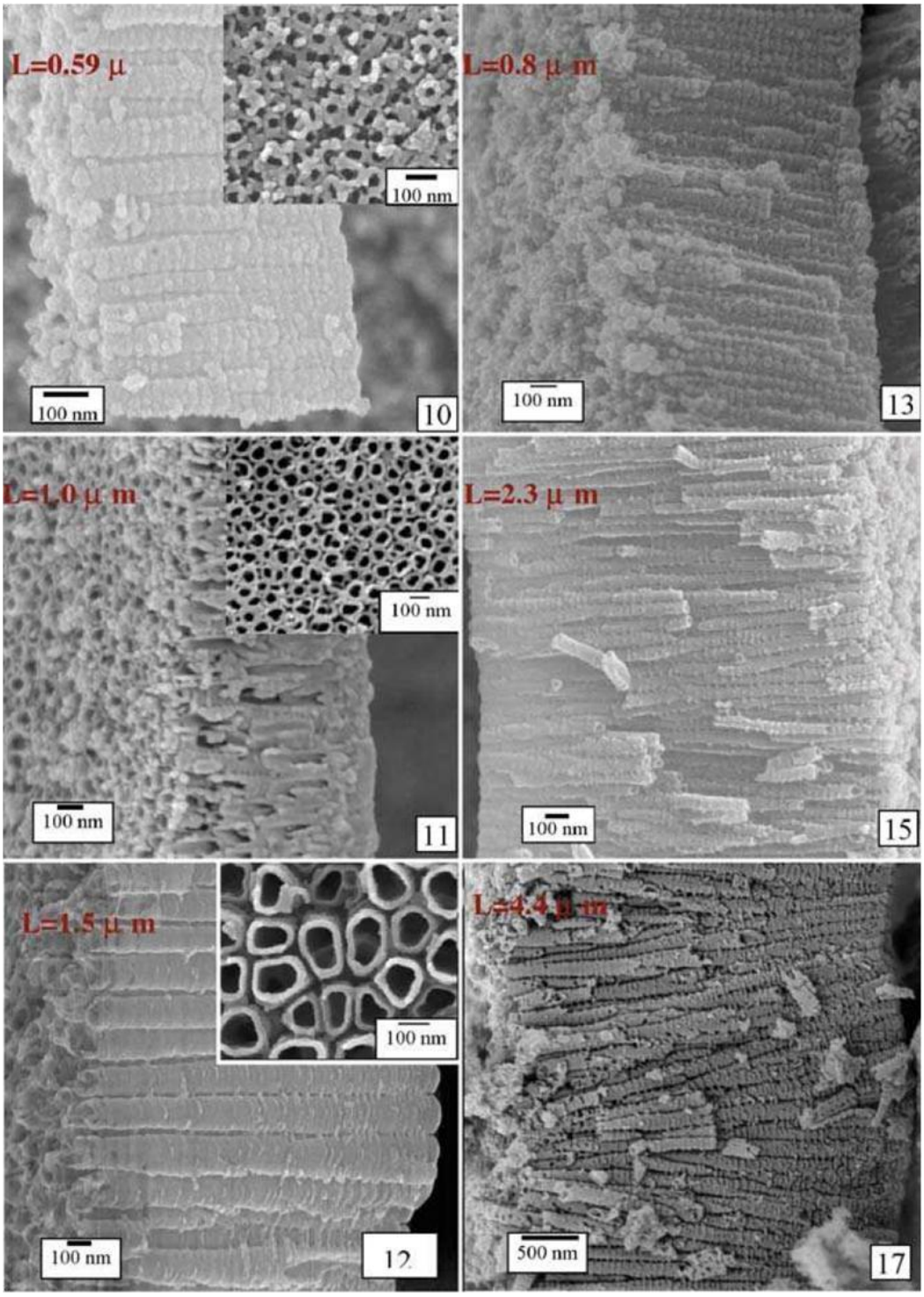

Figure 2-4: Lateral view of the nanotubes formed in different pH solutions (pH>1). The anodization conditions for each sample are 0.2M citrate 0.1 M F^-, 1 M SO_4^{2-} with different pH potential and time. Samples 10, 11 and 12 show variation of pore size and length with different anodization potentials (10, 15 and 25V respectively) for 20h in a pH 2.8 electrolyte; samples 13 and 15 show variation of anodization time on tube length with anodization potential of 10V in a 3.8 pH electrolyte; sample 17 compare with sample 12 show variation of pH value from 2.8 to 4.5 on tube length with anodization potential of 25V for 20h [27].

The final breakthrough of using polar organic electrolyte while reducing water content successfully leads to fabrications of very long nanotubular structure. The electrolyte using organic solvent such as ethylene glycol and dimethyl sulfoxide is considered as third generation. The reduced water content restricts the availability of oxygen as well as the chemical dissolution of the oxide. In other words, the growth of metal oxide becomes steadier and etching of oxide by fluoride becomes slower. As in aqueous electrolyte system, only 23% of the Ti is converted into the observed TiO_2 nanotubes in the end, the remaining TiO_2 will be dissolved as $[TiF_6]^{2-}$ or will to a minute extent (≈ 0.3%) be present as TiO_2 in collapsed nanotubes. Therefore, steady growth of metal oxide corresponds to a more stable architecture instead of a shorter tube length. (As solubility of Ti is suppressed when water content is reduced)

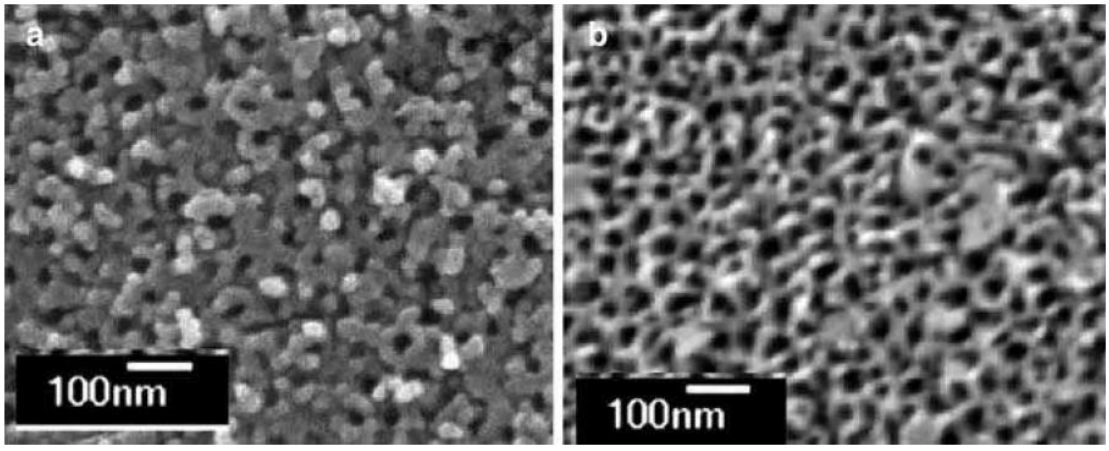

Figure 2-5: FESEM images of 10 V nanotube arrays anodized at: (a) 5 ℃ showing an average wall thickness of 34 nm, and (b) 50 ℃ showing an average wall thickness of 9 nm. The pore size is ~22 nm for all samples [29]

Generally, lower anodization potentials result in shorter nanotubes with smaller diameter using polar organic electrolytes. The increasing in nanotube length with anodization potential is attributed to the increasing driving force of ion transport

within barrier layer at the tube bottom. Furthermore, the temperature is another critical factor in the growth of nanotube arrays. [28] Top view pictures between samples anodized at the same conditions except temperature are given in Fig. 2-5. It shows that the chemical dissolution process is much more pronounced at a higher working temperature which leads to a thinner wall thickness and a shorter tube length. In the next section, possible mechanism of self-organized nanotubular formation will be discussed.

2.1.3 Possible mechanism of nanotube growth

From all the relevant studies, we can derive how those working conditions affect the morphology of the nanotube in certain ways. Basing on experimental evidence, it is solid to conclude that there are several processes essentially take place during the anodization under sufficiently high potential. Metal is oxidized to M^+ at the metal-electrolyte interface and the M^+ ions migrate outwards; O^{2-} driven by electric field incorporated in the film and migrate towards the metal-oxide interface. If the system is at a constant potential, the electric field within the oxide is progressively reduced by the increasing oxide thickness; the process is hence continuously slowing down and self-limiting. The final balanced process leads to a compact oxide layer with a finite thickness which is proportional to the applied field strength. After the formation of a compact layer, the distribution of the electrical field in the oxide is strongly related with the surface morphological fluctuations. As a result, field-enhanced dissolution in the anodic oxide takes place and the pores start to form. A predominant condition to reach this step it the metal complex formation. A more detailed

schematic description of tube growth is given in Fig. 2-6. With anodization onset a thin layer of oxide forms in Fig. 2-6a, small pits originate in the oxide layer due to the localized dissolution in Fig. 2-6b. There is an increase in the electric field intensity at the barrier layer at the bottom of the pits which resulting in further pore growth in Fig. 2-6c. Successively, the pore growth process reaches a steady-state and uniformly distributed pores are obtained in Fig. 2-6d. If a pore is higher in aspect ratio than the other, this corresponds to a narrow pore opening and thinner TiO_2 at the metal/solution interface. Fluoride etching rate on oxide is faster in a higher aspect ratio structure helps to open up the pore size; faster migration of OH^- in a thinner oxide interface grows a thicker TiO_2 layer. From these perspectives, pores tend to close the gap themselves to maintain a uniformly distributed pore size. The nanotube length increases until the electrochemical etch rate is balanced with the chemical dissolution rate. After this point is reached the tube length is independent of the anodization duration in Fig. 2-6e.

The above mentioned processes are expressed in equations 2.2 to 2.6.

$$Ti + H_2O = TiO_2 + 2H^+ + 4e^- \quad (2.2)$$

$$2H^+ + 2e^- = H_2 \quad (2.3)$$

$$Ti + 2H_2O = TiO_2 + 2H_2 \quad (2.4)$$

$$TiO_2 + 6F^- + 4H^+ = TiF_6^{2-} + 2H_2O \quad (2.5)$$

$$Ti(OH)_4 + 6F^- = TiF_6^{2-} + 4OH^- \quad (2.6)$$

Taking 0.6 wt% NH_4F in volume ratio 98/2 EG/H_2O electrolyte as an example, the electrolyte is 0.18 molar in F^- and thus contains 9 mmol in a solution of 50 ml. It is usually observed that approximately 7 μm of porous TiO_2 nanotube arrays with outer/inner diameters of 80/120nm are fabricated on Ti foil by anodizing for 1 h when 20 μm of Ti is consumed. Since a circle-shaped anodization window is used for every sample, we are able to estimate the amount of F^- required dissolving TiO_2 given that no precipitate is observed in the used electrolyte. Under the conditions described above, 47 μmol of TiO_2 will be dissolved after 1 h of anodization with the assistance of 0.285 mmol of F^- ions out of 9 mmol of F^- in the stock solution. This corresponds to a consumption of 3.2% of the F^- ions for the first anodization and an even lower consumption for consecutive anodization. Thus there is clearly sufficient F^- in the solution to sustain several anodization processes. The reutilization of the electrolyte would lead to a nominal consumption of 0.2% of the water per anodization cycle. It should, however, be kept in mind that - at least in Singapore - the water concentration of the slightly hygroscopic electrolyte will tend to increase when the electrolyte is exposed to the humid atmosphere over extended periods, which may overcompensate the water consumption.

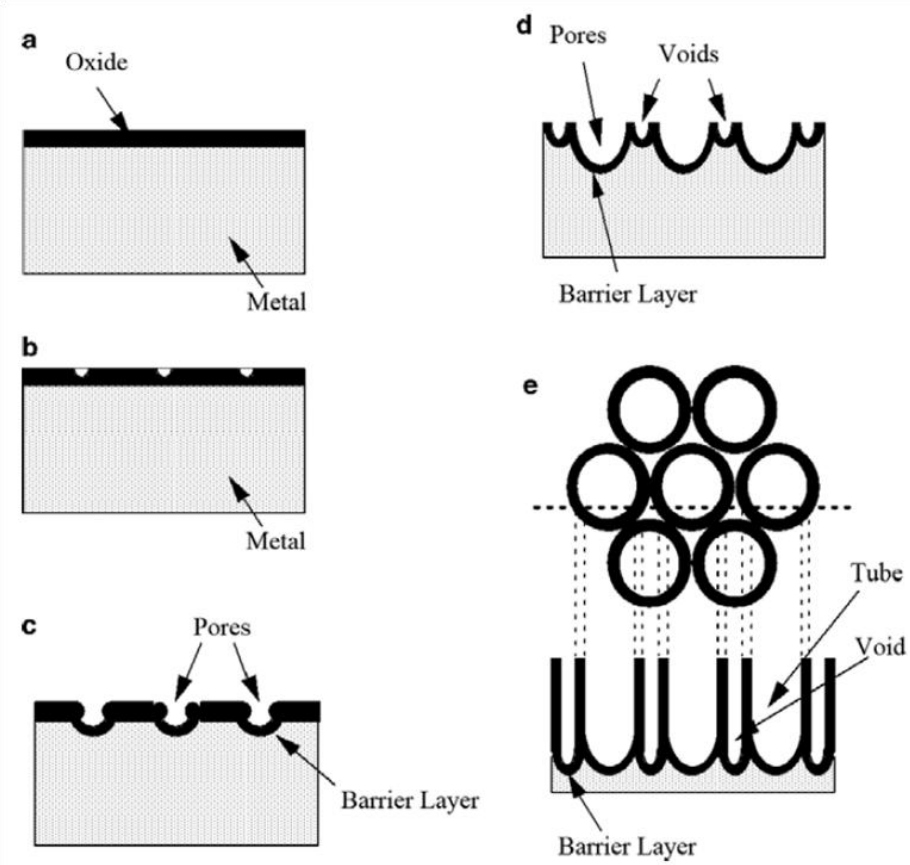

Figure 2-6: Schematic diagram of nanotube evolution at constant anodization potential: (a) Oxide layer formation, (b) pit formation on the oxide layer, (c) growth of the pit into scallop shaped pores, (d) the metallic region between the pores undergoes oxidation and field assisted dissolution, (e) fully developed nanotubes with a corresponding top view. [29]

Some other possible mechanisms are proposed. For one case, due to the volume expansion, a mechanical stress originating from the expansion during oxide formation occurs at the metal-oxide interface. Since the metal oxidation at the pore bottom takes place uniformly and simultaneously, the material can only expand in a vertical fashion.[30] Therefore, following 3 factors are crucial: (1) volume expansion generates stress at the interface; (2) field distribution at the inner tube bottom; (3) local acidity creates pH drop at the pore tip can enhance chemical dissolution when hydrolysis takes place. The competition between oxide formation and chemical

dissolution leads to V-shaped wall profiles as the earlier formed part of the walls are exposed longer to the electrolyte. Typically low electrolyte acidity and low fluoride concentration are desired. The significance of discussing nanotube growth mechanism is to understand how to deliberately control the tube size, length and wall thickness. Yasuda *et al.* [31] study Ti and TiZr showed that the nanotube diameters are linearly proportional to the anodizing ratio of the metal oxide.

$$f_{growth} = t_{film} / \Delta U \quad (2.7)$$

A typical value of f_{growth} for Ti/TiO_2 is 2.5 nm/V. [31] Here is a dilemma as the tube is desirable to possess high aspect ratio and larger tube density per area as photoelectrode for photovoltaic application; simply increasing the potential would result in a longer tube as well as a larger tube diameter. Besides, a thinner wall (less than 4 nm) thickness is more helpful in charge transport along tube length direction.

2.2 Charge transport dynamics in nanostructured TiO_2

2.2.1 Ambipolar diffusion model

Ambipolar diffusion [32] is applicable to the interaction between cations from electrolyte and electrons in metal oxide in DSCs. This model is helpful in understanding electron movement inside TiO_2 nanostructures. The transport of an injected electron is essentially diffusional due to screening by the strong ionic electrolyte at a light intensity up to one sun. The motion of electrons creates a charge imbalance, and the resulting electric field drags the cations along with them. At the

same time, negatively charged ions are repelled from the electron. The net effect is that diffusion of electrons is retarded, and the diffusion of ions is increased. A simplified expression for the ambipolar diffusion coefficient of charge transport has been proposed: [33]

$$D_{amb} = \frac{n + p}{\frac{n}{D_p} + \frac{p}{D_n}} \quad (2.8)$$

Here, D_p, D_n are diffusion coefficient of cations and electron respectively. Notation of n and p represents concentration of electron and cations respectively. The ambipolar diffusion coefficient is close to the diffusion coefficient of electron in the metal oxide when the concentration of cations in electrolyte is much more than that of the electron. Moreover, electrons can be detected in the external circuit corresponding with the arrival of electron at the collecting electrode. In particular, ambipolar diffusion is incongruous with multiple-trapping kinetics. However, there are people arguing that the ions in the electrolyte establish a quasi-static potential energy well inside the anatase that retards the electron from advancing its original position no matter how fast it moves. A high frequency ac field cannot shield the field caused by slow relaxation of the electrolyte because it cannot generate a charge density over length scales larger than a few atoms.

2.2.2 Multiple trapping model

Trapping theory is proposed to explain the light intensity dependence of diffusion coefficient with a power law. Here, n is photo injected electron density.

$$D \propto n^{\left(\frac{1-\alpha}{\alpha}\right)} \quad (2.9)$$

Generally, the electron diffusion coefficient in nanostructured anatase is much higher than for single crystalline anatase, due to the higher number of surface states that contribute to the concentration of free electrons. Carriers are emitted from a distribution of trap states thermally. To account for such behaviour with the energetic disorder model, the energy distribution of trap states g(E) would have an exponential form: [34,35]

$$g(E)=g_0 \exp\left[\frac{\alpha(E-E_c)}{k_B T}\right], \quad (2.10)$$

Here, E is the trap energy and E_c is the conduction band edge energy. The parameter α which describes the steepness of the trap state distribution is related to the average trap depth m_c by $\alpha=k_BT/m_c$. [36]

At steady state, the equilibrium of empty and trap-filled states establishes a quasi-Fermi level. The occupancy of a trap level is described by Fermi-Dirac statistics:

$$f(E)= [1 + \exp(\frac{E-\bar{\mu}_n}{kT})]^{-1} \quad (2.11)$$

where $\bar{\mu}_n$ is electrochemical potential of electron quasi-Fermi level). The power law dependence of electron diffusion on the photo carrier density can be obtained by integrating the product of g(E) and f(E) with the assumption that the detrapping time is much longer than the intertrap diffusion time.

There is an additional thermodynamic driving force caused by the charging of anatase nanoparticles resulting in a band edge shift. [37] The consequence of this causes buildup of an electrical field across the metal oxide layer because of the

electron concentration dependence on position. This also serves as an extra driving force for electron transport.

2.3 Charge transfer at semiconductor/electrolyte interface

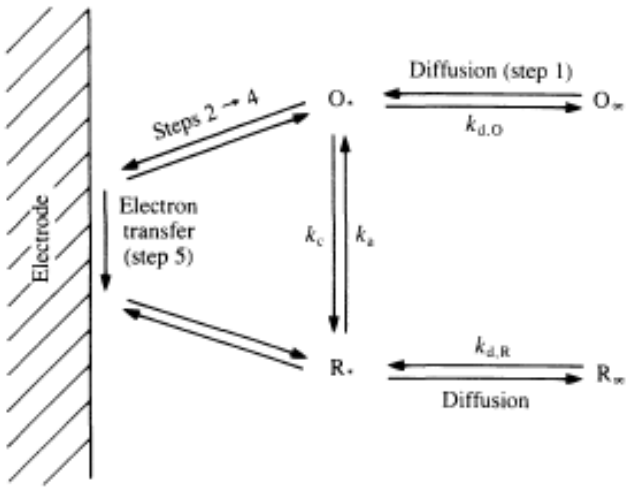

Figure 2-7: Scheme of electron transfer at an electrode. [13]

When a metal electrode is placed into a solution containing ions (there are donors or acceptors), electrons will flow from or to the electrode until equilibrium state is reached. We consider the case $I_3^- + 2e^- = 3I^-$, where there are following steps shown in Fig. 2-7. Diffusion of the species takes place from bulk of the electrolyte to where reaction occurs (k_d) in step 1. The rearrangement of the ionic atmosphere takes around 10^{-8} s. There will be reorientation of the solvent dipoles (10^{-11} s) followed by alternations in the distance between the central ion and the ligands (10^{-14} s). These include the steps 2 to 4 in Fig. 2-7. After electron transfers, relaxation processes happen in an inverse way. In a solution containing equal quantities of species O and

R, rate constant $k_{ox}=k_{red}$ when $E=E_0$. In this case, the standard rate of electron transfer k^0 is defined as

$$k^0 = A_{red} \exp\left(\frac{-\Delta G_{red}}{RT}\right) = A_{ox}\exp\left(\frac{-\Delta G_{ox}}{RT}\right) \quad (2.12)$$

For an expression relating to the charge transfer current i_{ct}, which is also known as Butler-Volmer relationships,

$$i_{ct} = nFAk^0\left[C_{red} \exp\left(\frac{(1-\alpha)nF(E-E^0)}{RT}\right) - C_{ox} \exp\left(\frac{-\alpha nF(E-E^0}{RT}\right)\right] \quad (2.13)$$

Here, α is a measure of the slope of the energy profiles in the transition state zone, value of α varies from 0 to 1.

In a dye-sensitized solar cell, the charge transfer at the interface between Pt and redox electrolyte is governed by Butler-Volmer equation, the exchange current is extremely fast as there is a low energy barrier for the processes take place at Pt electrode. In a semiconductor, the Fermi-level at equilibrium is usually located between conduction band and valence band where there are only a few donor or acceptor states in the bandgap. The exchange current density in this case is much smaller compared to metal/electrolyte interface. Take an n-type semiconductor as example in Fig. 2-8. Filled states at the conduction band edge can donate electrons to species solution leading to a small exchange current. The electron transfer from R to the conduction band i_n^+ depends on the density of empty states in the conduction band, which is appoximated by N_{cb}; The electron transfer from the conduction band to O i_n^- (cathodic current) depends on the number of conduction band electrons which approximated by n_{cb}.

$$n_{cb} = N_{cb}\exp\left(\frac{-(E_{cb}-E_F)}{kT}\right) \quad (2.14)$$

Therefore, i_n^+ is almost independent on applied bias while i_n^- is strongly dependent on applied bias (as seen in Equation 2.15/2.16, here $\eta=V-V_{eq}$ which is over potential). So in a similar way for the valence band current, the anodic current (flow of holes from the valence band to R) varies exponentially with over potential (This is valid in the state of band edge pinning so that all the potential drop is applied cross the space charge). A Tafel plot shows the logartithmic rate of an electrochemical reaction vs. the overpotential, defined as the difference between the potential required to drive the reaction minus the equilibrium potential to overcome the energy barrier of a reversible reaction. Between the limiting current plateau of a voltammogram and the linear region close to E_{eq} (current at equilibrium) there is a region of potential for irreversible reactions where current depends exponentially on the potential (so that the Tafel plot shows a linear region). This is called Tafel region. In the absence of trap states ($\alpha = 1$), the Tafel plot is supposed to have a slope of 59 mV per decade.

$$i_n^-(\eta) = i_{n,0}\exp\left(\frac{-eV}{kT}\right) \qquad (2.15)$$

$$i_p^+(\eta) = i_{p,0}\exp\left(\frac{eV}{kT}\right) \qquad (2.16)$$

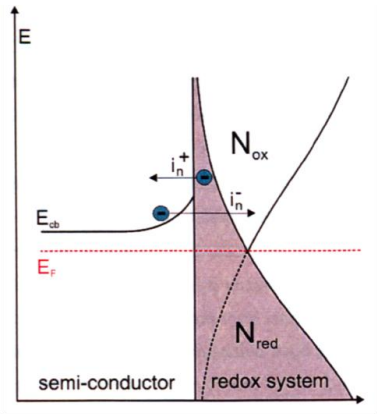

Figure 2-8: Electron transfer via the conduction band in a semi-conductor.[12,13]

2.4 Recombination kinetics in dye-sensitized solar cell

Generally, the characteristic time for recombination in DSC under normal illumination conditions ranges from milliseconds to minutes [38], and transport is generally faster than recombination. The net recombination reaction can be expressed as:

$$I_3^- + 2e^- \rightarrow 3I^- \qquad (2.17)$$

It is necessary to study the mechanism of charge transport so as to control the cell performance. In the following section, topics including location of recombination reactions within the cell, the trap state distribution and band edge movement will be discussed.

2.4.1 Discussion of recombination at interfaces in DSCs

The interface, where recombination predominates, will depend on the redox electrolyte and the surface properties of both the transparent conductive oxide (TCO) substrate and TiO_2. The locus of recombination in dye-sensitized TiO_2 solar cells with the standard I_3^-/I^- couple is related to where charge builds up in the cell. Intensity modulated photovoltage spectroscopy (IMVS) [37] study indicates that photoinjected electrons build up in the nanoparticle TiO_2 film and the photo-potential of the cell originates from the change of the quasi-Fermi level of the TiO_2 film with respect to the variation in buildup of charge. Electrical impedance spectroscopy (EIS) measurements of the cell show [39] that an exponential bias dependent behaviour of

chemical capacitance is developed at the TiO_2 nanoparticle/electrolyte interface. The capacitance reaches a value of several mF/cm^2 at open circuit, charges of this large amount indicate that the process is most likely attributed to the charging of surface states of the anatase film. Furthermore, the reduction of the oxidized component of the I_3^-/I^- couple occurs relatively slowly on both the FTO and TiO_2 surface, and the overpotential for reducing the oxidized component of the I_3^-/I^- couple is less at the surface of porous nanoparticle films of TiO_2 than at the TCO surface. There is a substantial loss of both the photocurrent and voltage when recombination occurs primarily at the TCO surface. In contrast to improvement of PV property when passivating the substrate in a fast redox system, passivating the TCO surface has no effect on the PV response of cells with the I_3^-/I^- couple [40], implying that recombination in working cells does not take place principally at the TCO.

2.4.2 Recombination mechanism

It is commonly accepted that the recombination mechanism is governed by a transport limited model. It is assumed that the rate limiting step involves an electron captured by a surface-adsorbed molecular iodine species produced in the chemical equilibrium of I_3^-. The diffusion limited recombination rate is then written as [41]:

$$R \propto D_n n \propto n^{1/\alpha} \tag{2.18}$$

As D_n depends on n, the recombination rate depends non-linearly on n. In particular, it can be shown by combining the characteristic time for photoelectron

recombination τ_r ($\tau_r = n/R$) and previous formula 2.18. The recombination time is proportional to the diffusion time. ($\tau_r \propto \tau_c$)

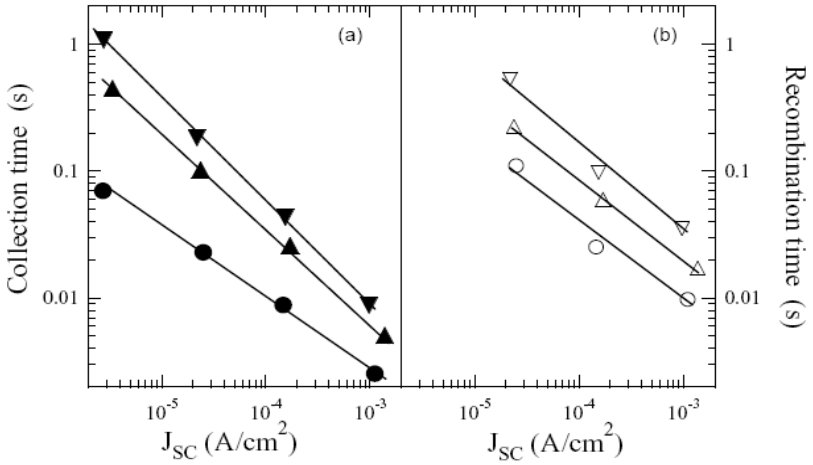

Figure 2-9: Dependence of: (a) diffusion and (b) recombination times on short-circuit photocurrent density for cells containing an undoped TiO_2 nanoparticle film (circles) and Li-doped TiO_2 nanoparticle films (triangles). The lines are power-law fits to the data. Adapted from [41]

Faster diffusion resulted from increasing the photoelectron density is owing to the progressive filling of deep traps in Fig. 2-9. With faster diffusion, there is a greater probability per unit time that electron will have a lower chance to encounter recombination sites.

2.4.3 Photovoltage

In the context of solar cells, open circuit voltage is commonly defined as the difference between the quasi-Fermi level of the electron in anatase in the light ($\bar{\mu}_n^0$) and the Fermi level in the dark ($\bar{\mu}_n$) in the solar cell community. [42] The photoinjected electron density n_{cb} in the conduction band of anatase depends on the

dark electron concentration ($n_{cb,0}$) and the difference between the quasi-Fermi level in the light and the one in the dark:

$$n_{cb} = n_{cb,0} \exp[q(\bar{\mu}_n - \bar{\mu}_n^0)/kT)] \quad (2.19)$$

A similar expression can be written of the total photoinjected electron density when electrons reside predominantly in an exponential distribution of traps:

$$n = n_{t,0} \exp[q(\bar{\mu}_n - \bar{\mu}_n^0)/m_c)] \quad (2.20)$$

where m_c is the characteristic energy of the exponential trap state distribution and $n_{t,0}$ is the trapped electron density in the dark. The expression exhibits that the average trap depth can be determined from measurements of the electron charge in the film versus the open circuit voltage. [37]

At open circuit electrons can recombine via surface states and the conduction band in the TiO_2. Assuming that the quasi-static approximation applies, communication between trap states and the conduction band is rapid and inhomogeneities in the charge distribution should not exist. As a result open-circuit voltage decay measures what is almost a succession of steady state photovoltages. If it is assumed that the conduction band electron density is contained within an exponential distribution of N_{CB} states then τ_n is given by [43] $\tau_n = -\frac{k_B T}{q}\left(\frac{dV_{oc}}{dt}\right)^{-1}$.

2.4.4 Band edge movement

As indicated in previous section, the open circuit voltage is usually fixed. An exception to this behaviour takes place when there is band-edge movement. The shift in band edge can be caused by chemically treating the surface or exposing the cell to

sufficiently high light intensity. [37] A very well-known effect of band-edge movement is adding 4-tert-butylpridine or ammonia onto anatase surface. This causes a significant shift of band edge to negative direction while recombination process becomes much slower owing to a decrease of the trapped electron density in the dark. Lower photovoltages have resulted from adding adsorptive cations like Li^+ which charge the surface positively.

2.5 Electrochemical impedance study

2.5.1 Background

Since the end of World War II we have witnessed the development of solid state batteries, a revolution in high-temperature electrochemical sensors, and the introduction of fuel cells to avoid the Carnot inefficiency inherent in non-catalytic energy conversion. As a consequence, the characterization of systems with solid-solid or solid-liquid interfaces has become a major concern of electrochemists and materials scientists. Impedance spectroscopy is a powerful method to characterize the electrical properties of materials and their interfaces with conducting electrodes. It can also be used to investigate the dynamics of bound or mobile charge in the bulk or interfacial regions of solid or liquid material such as semiconductor, insulators and so on. [44]

A monochromatic signal $v(t) = V_m\sin(\omega t)$ with frequency $f = \omega/2\pi$ is applied to a sample and the resulting current is $i(t) = I_m\sin(\omega t+\theta)$, where θ is the phase lag between potential and current signal in Fig. 2-10. Depending on what electronic

elements studied, θ can be zero or other number. In general, the solution of a system of differential equations is required. But the use of Fourier transformation can somehow simplify the case and make solution visible in frequency domain.

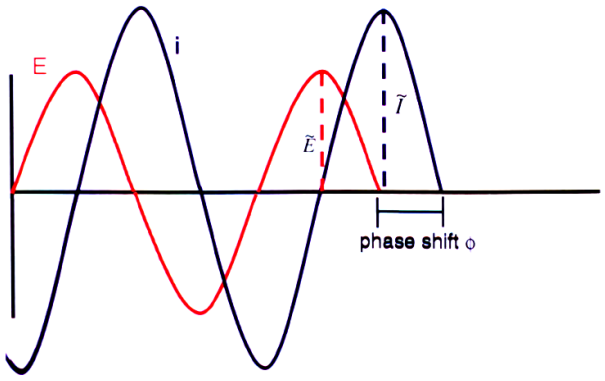

Figure 2-10: A sinusoidal varying potential and the current response 90 °out of phase. [12]

The concept of electrical impedance was first introduced by Oliver Heaviside [45] in the 1880s and developed in terms of vector diagrams and complex representation by Kennely and Stenmetz. Briefly, an impedance Z(w) =Z' + *j*Z" is a vector quantity and can be ploted in the plane with rectangular coordinates. Re(Z) = Z'=|Z| cos(θ) and Im(Z) = Z" =|Z| sin(θ). Where θ = $\tan^{-1}$(Z"/Z'), and $|Z|^2$= $(Z')^2$ + $(Z")^2$. For a pure resistor, Z=R; for a capacitor, Z= 1/ *j*ωC; for an inductor, Z= *j*ωL. The operation rules of series or parallel connection are the same as defined for resistors. Fig. 2-11 shows two typical RC circuits and their impedance plane plots.

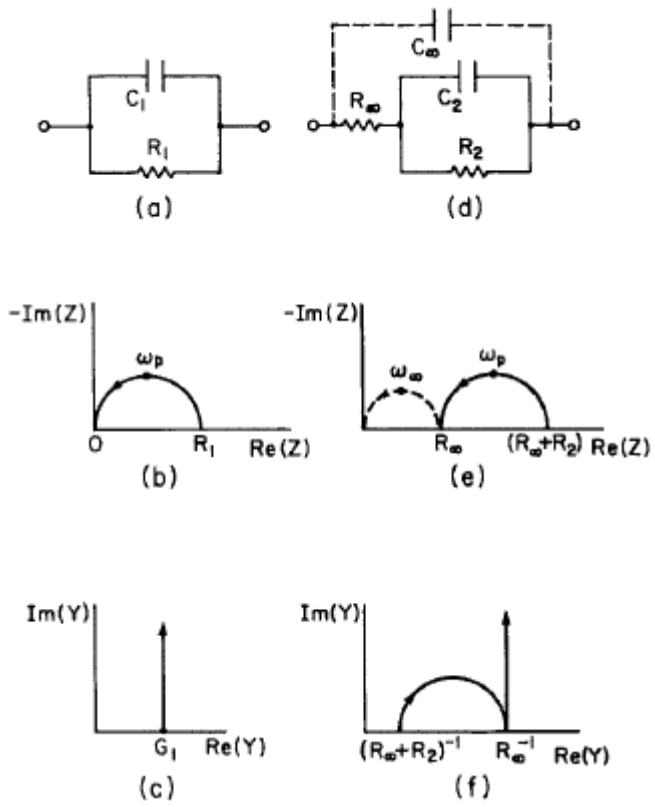

Figure 2-11: a and d show two common RC circuits. Parts b and e show their impedance plane plots and c and f their admittance plane plots. Arrows indicate the direction of increasing frequency. [44]

2.5.2 Equivalent circuit in dye-sensitized solar cells

Electrons are injected into the conduction band of mesoporous TiO_2 from the excited state of dye molecules, it may undergo recombination with trap states from internal of the semiconductor or surface states, or it may recombine with I_3^- or dye molecules. The kinetics for electron injection from dye molecules and dye regeneration process has been proved to be extremely fast. The factors that determine the charge collection efficiency of injected electrons are competition between recombination (electron in

TiO_2 with I_3^-) and charge transport of electron in TiO_2. A redox electrolyte (typically I^-/I_3^-) or hole transporting medium (CuSCN) is used for dye regeneration.

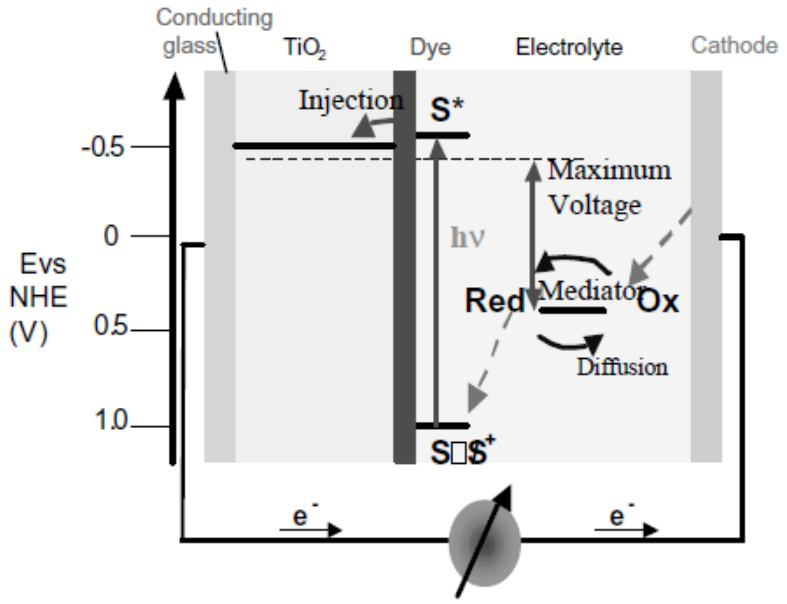

Figure 2-12: Principle of operation and energy level scheme of the dye-sensitized nanocrystalline solar cell. Photo-excitation of the sensitizer (S) is followed by electron injection into the conduction band of the mesoporous oxide semiconductor. The dye molecule is regenerated by the redox system, which itself is regenerated at the counter electrode by electrons passed through the load. Potentials are referred to the normal hydrogen electrode (NHE). The open-circuit voltage of the solar cell corresponds to the difference between the redox potential of the mediator and the Fermi level of the nanocrystallline film indicated with a dashed line. [46]

A typical operation scheme of the dye-sensitized solar cell is given in Fig. 2-12. Another version with equivalent circuit is shown in Fig. 2-13a. The series resistance R_s is an overall contribution from the resistance of TCO glasses and contact resistance. At the Pt electrode and electrolyte interface, the double layer capacitance and charge transfer resistance together constitute a RC circuit ($R_{CE}//C_{CE}$). At the interface between uncovered FTO and electrolyte, the interface capacitance and the electron recombination resistance contribute to another RC element ($R_{FTO/EL}//C_{FTO/EL}$) in equivalent circuit. Beside the transmission line model, the final element is the

diffusion element due to redox species in the electrolyte. The semi-infinite diffusion of the electrolyte towards counter electrode contributes to a Warburg diffusion plot in impedance plane when the cell is under illumination at low frequency range.

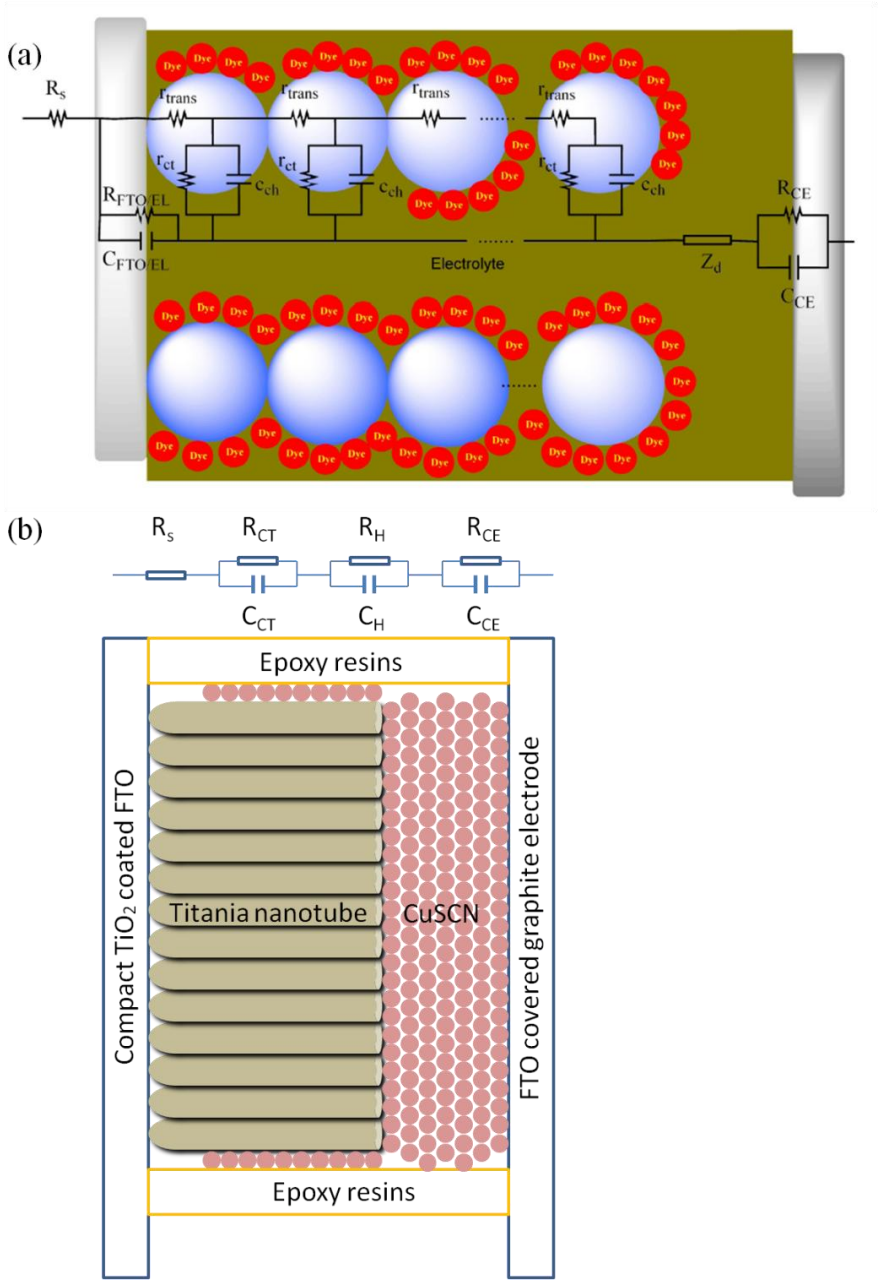

Figure 2-13: Equivalent circuit for the dye-sensitized solar cells include transmission line model. [47] (a); and for SSDSC (b) [48].

The most important parameters that can be extracted from fitting the impedance spectroscopy of a dye-sensitized solar cell in dark are charge transport resistance of electron in TiO_2, chemical capacitance of TiO_2 and charge transfer resistance of electron from TiO_2 to redox electrolyte (also named as recombination resistance). In the transmission line model, there are two channels in parallel, representing electron transport through TiO_2 and redox species transport in the electrolyte in the pores, respectively. The charge transfer process connects these two channels. If the length of the mesoporous TiO_2 is L, the charge transport resistance $R_t=r_{trans}L$, recombination resistance $R_{ct}=r_{ct}/L$, and chemical capacitance $C_\mu=c_{ch}L$.

If the semiconductor is not in the state of Fermi-level pinning condition, a shift in quasi Fermi-level is accompanied by the applied potential. A precondition is assumed that the applied potential causes a corresponding shift of Fermi-level inside semiconductor, and the Fermi-level is flat at various biases because $I_{dark}R_t$ is negligible.

The chemical capacitance is a measure of the change in electron density on a small variation of the chemical potential with the form [49],

$$C_\mu = e^2 \frac{\partial}{\partial E_F} \int_{E_2}^{E_1} F(E - E_{Fn}) g(E) dE \approx e^2 g(E_F) \tag{2.21}$$

By measuring the chemical capacitance, it is possible to pinpoint the distribution of density of states in the band gap. [50] N_L is the total density of the localized states and α is a parameter with (or without) temperature units that determines the depth of distribution below the lower edge of the conduction band E_c.

Combine 2.21 and 2.10, we find out that

$$C_\mu = C_0 \exp\left(\frac{\alpha e}{k_B T} V\right) \tag{2.22}$$

The value of α for nanoparticle is 0.36-0.4 measured by Wang *at el.* [51]. For the nanotube-based cell, the value is comparably lower ~ 0.2 measured in my experiment, which indicates that there is shallow distribution of density of states under lower edge of the conduction band for nanotubular structure. Experimental evidence shows that the behaviour of charge transport resistance with respect to temperature and bias potential is very similar to that of chemical capacitance. This dependence indicates the presence of a transport level which is close to the edge of the conduction band. The transport resistance governed by the Boltzmann distribution is inversely proportional to the density of carriers at the transport level. Therefore,

$$R_t = R_{t0}\exp\left[-\frac{e}{k_B T}\left(V + \frac{E_{F,redox} - E_c}{e}\right)\right] \qquad (2.23)$$

In the multiple-trapping model, the total electron density is composed of electron densities in a conduction band and in localized states. Transport through extended states is slowed by trapping-detrapping events to localized states, while direct hopping between localized states is neglected.

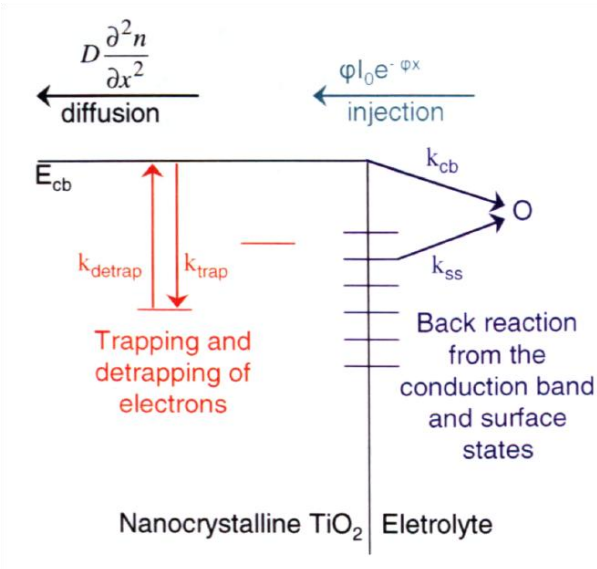

Figure 2-14: Diagram showing the processes that can occur in a dye sensitized solar cell at short circuit: injection, diffusion and recombination via the TiO_2.

At the same time, transporting electrons are slowed down by trapping and detrapping process and back reaction from conduction band or surface states in Fig. 2-14. Ambipolar model indicates that the electron movement is essential diffusion movement, there will be following equation when Fick's laws are applied to describe the electrons in conduction band of TiO_2. Consider a porous semiconductor network and the conducting substrate is x=0. Electrons diffuse and recombine in the film 0<x<L, and the transport is blocked at the outer edge of the film where x = L. Here, the condition J=0, dn/dx=0 at x=L. This is the reflecting boundary condition given in Fig. 2-15a.

$$\frac{\partial n}{\partial t} = D\frac{\partial^2 n}{\partial x^2} - k(n - n_0) \tag{2.24}$$

take $\tau_n = k^{-1}$, k is back reaction rate.

In the steady state, the excess electron concentration is determined by the equation:

$$\frac{\partial^2 n}{\partial x^2} - \frac{n - n_0}{L_n^2} = 0 \tag{2.25}$$

$$L_n = (D\tau_n)^{1/2} \tag{2.26}$$

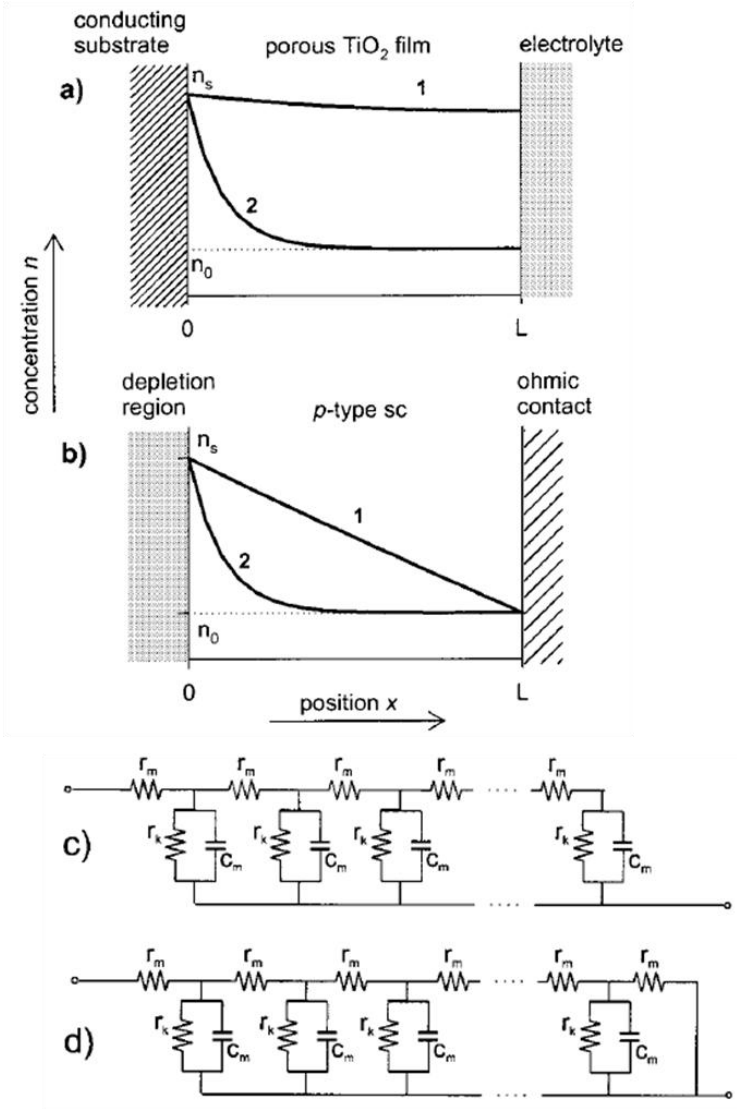

Figure 2-15: Excess concentration in the stationary condition for (a) electrons injected at the substrate to a porous semiconductor film permeated with a redox electrolyte (the electrons are blocked at the outer edge of the film) and (b) electron minority carriers in the p region of the semiconductor p-n junction (the electrons are extracted at the ohmic contact). In both cases, curve 1 is for L_n=2L and curve 2 for L_n=0.1L.Transmission line representation of the diffusion impedance: (c) diffusion coupled with a homogeneous reaction with the reflecting boundary condition; (d) diffusion coupled with a homogeneous reaction with the absorbing boundary condition. [49] [52]

When a small amplitude oscillating quantities is superimposed to a given stationary state, the formulae above convert into the form of ac modulated quantities. After

Laplace transformation, the impedance for the reflecting boundary condition in Fig. 2-15a is: [53,54]

$$Z = (\frac{R_w R_k}{1+i\omega/\omega_k})^{1/2} \coth\left[(\omega_k + \omega_d)^{1/2}(1 + i\omega/\omega_k)^{1/2}\right] \quad (2.27)$$

R_w is charge transport resistance and R_k is recombination resistance. More generally, the behaviours with respect to the variation of the frequency are determined by the relative value of these two parameters in the system as expressed in the following relationships:

$$\frac{R_k}{R_w} = \frac{\omega_d}{\omega_k} = (\frac{L_n}{L})^2 \quad (2.28)$$

$\omega_d$is the characteristic frequency of diffusion in a finite layer, $\omega_k$is the characteristic frequency of recombination process. When $R_k >> R_w$,

$$Z = \frac{1}{3}R_w + \frac{R_k}{1+i\omega/\omega_k} \quad (2.29)$$

When $R_k << R_w$, also named as Gerischer impedance

$$Z = (\frac{R_w R_k}{1+i\omega/\omega_k})^{1/2} \quad (2.30)$$

Generally for a dye-sensitized solar cell, the impedance of fresh-assembled liquid electrolyte cells in Nyquist plot is described by equation 2.29. It is reported that the one of aged sample [51] or solid-state cell is governed by equation 2.30 due to faster recombination process. The equivalent circuit of SSDSC is given in Fig. 2-13b, its corresponding impedance is displayed in Fig. 2-16b.

The absorbing boundary condition shown in Fig. 2-15b, is akin to the neutral p region of a semiconductor p-n junction diode. The number of electrons injected at x=0 is determined by the potential drop across the space-charge region at the junction, however, all of the electrons that reach the substrate are extracted at the ohmic contact

so that the electron concentration there remains constant: $n=n_0$ when x=L. When recombination resistance in this system is large, the conductive path at x=L becomes dominant, so the effect of recombination becomes insignificant, $R_{dc}=R_w$. For the other case, recombination resistance is smaller than charge transport resistance, it becomes the Gerischer impedance again, $R_{dc}=(R_wR_k)^{1/2}$.

The typical Nyquist plots for the above mentioned two boundary conditions are shown in Fig. 2-16. The curve is strongly dependent on relative magnitude of recombination resistance and charge transport resistance.

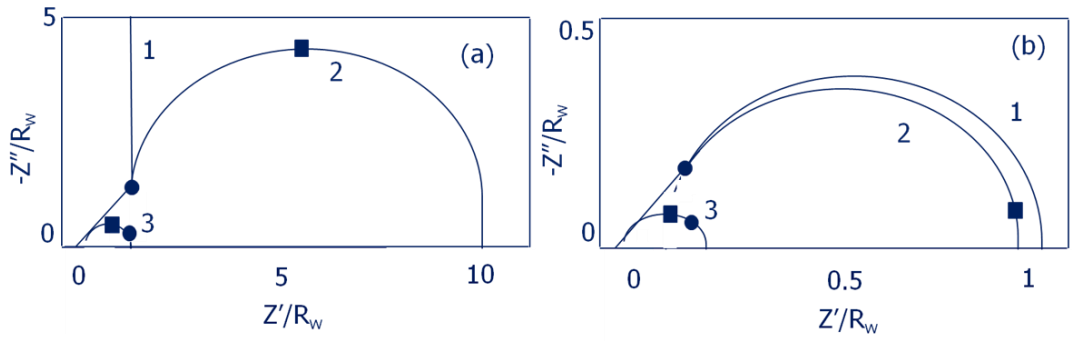

Figure 2-16: Complex plots of the impedance model for diffusion coupled with a homogeneous reaction with the reflecting boundary condition (a), and absorbing boundary condition (b). Curve 1 is for no reaction, R_k is close to infinity. In curve 2, $R_k>>10R_W$. In curve 3, $R_k<<0.1R_W$. The marked points correspond to frequencies (Hz) f =ω_d(circle) and f=$\omega_k/2\pi$(square). [49]

References

1 J. Fierro, Metal Oxides: Chemistry and Applications, CRC Press, Boca Raton, USA, 2006.

2 H. Tsuchiya and P. Schmuki, Electrochem. Commun. 2005, 7, 49.

3 I. Sieber, H. Hildebrand, A. Friedrich and P. Schmuki, Electrochem. Commun. 2005, 7, 9.

4 I. Sieber, B. Kannan and P. Schmuki, Electrochem. Solid-State Lett. 2005, 8, J10.

5 H. Tsuchiya, J. M. Macak, I. Sieber, L. Taveira, A. Ghicov, K. Sirotna and P. Schmuki, Electrochem.Commun. 2005, 7, 295.

6 H. Tsuchiya, J. M. Macak, L. Taveira and P. Schmuki, Chem. Phys. Lett. 2005, 410, 188.

7 A. Ghicov, S. Aldabergenova, H. Tsuchiya and P. Schmuki, Angew. Chem., Int. Ed. 2006, 45, 6993.

8 S. Berger, H. Tsuchiya and P. Schmuki, Chem. Mater. 2008, 20, 3245.

9 K. Yasuda and P. Schmuki, Electrochem. Commun. 2007, 9, 615.

10 J. M. Macak, H. Tsuchiya, L. Taveira, A. Ghicov and P. Schmuki, J. Biomed. Mater. Res., Part A 2005, 75A, 928.

11 A. Ghicov, P. Schmuki, Chem. Comm. 2009, 2791.

12 P. J. Cameron, Studies of Dye Sensitized Solar Cells, PhD thesis, University of Bath, Nov 2004.

13 C. M. A. Brett, M. O. Brett, Electrochemistry: Principles, Methods, and Applications, Oxford University Press, first published 1993, reprinted 1994.

14 F. Fabregat- Santiago, G. Garcia-Belmonte, J. Bisquert, P. Bogdanoff and A. Zaban, J. Electrochem. Soc. 2003, 150, 6.

15 F. Keller, M. S. Hunter and D. L. Robinson, J. Electrochem. Soc. 1953, 100, 411.

16 G. E. Thompson, R. C. Furneaux, G. C. Wood, J. A. Richardson and J. S. Goode, Nature 1978, 272, 433.

17 G. E. Thompson, Thin Solid Films 1997, 297, 192.

18 O. Jessensky, F. Muller and U. Gosele, J. Electrochem. Soc. 1998, 145, 3735.

19 H. Masuda, H. Yamada, M. Satoh, H. Asoh, M. Nakao and T. Tamamura, Appl. Phys. Lett. 1997, 71, 2770.

20 H. Asoh and S. Ono, Fabrication of Ordered Anodic Nanoporous Alumina Layers and their Application to Nanotechnology, ed. D. G. Staikov, Wiley-VCH, Weinheim, Germany, 2007.

21 S. P. Albu, A. Ghicov, S. Aldabergenova, P. Drechsel, D. LeClere, G. E. Thompson, J. M. Macak and P. Schmuki, Adv. Mater. 2008, 20, 4135.

22 C. Ruan, M. Paulose, O. K. Varghese, C. A. Grimes, Sol. Energy Mater. Sol. Cells 2006, 90, 1283.

23 R. P. Vitiello, J. M. Macak, A. Ghicov, H. Tsuchiya, LFP. Dick, P. Schmuki, Electrochem. Commun. 2006, 8, 544.

24 V. Zwilling, M. Aucouturier, E. Darque-Ceretti, Electrochim. Acta. 1999, 45, 921.

25 H. Tsuchiya, J. M. Macak, L. Taveira, E. Balaur, A. Ghicov, K. Sirotna, P. Schmuki, Electrochem. Commun. 2005, 7, 576.

26 S. Bauer, S. Kleber, P. Schmuki, Electrochem. Commun. 2006, 8, 1321.

27 Q. Cai, M. Paulose, O. K. Varghese, C. A. Grimes, J. Mater. Res. 2005, 20, 230.

28 G. K. Mor, K. Shankar, M. Paulose, O. K. Varghese, C. A. Grimes, Nano Lett. 2005, 5, 191.

29 G. K. Mor, O. K. Varghese, M. Paulose, N. Mukherjee, C. A. Grimes, J. Mater. Res. 2003, 18, 2588.

30 O. Jessensky, F. Muller and U. Gosele, Appl. Phys. Lett. 1998, 72, 1173–1175.

31 K. Yasuda, J. M. Macak, S. Berger, A. Ghicov and P. Schmuki, J. Electrochem. Soc. 2007, 154, C472–C478.

32 D. Nistér, K. Keis, S. E. Lindquist, A. Hagfeldt, Sol. Energy Mater. Sol. Cells 2002, 73, 411.

33 W. van Roosbroeck, Phys. Rev. 1953, 91, 282.

34 H. Scher, M. Lax, Phys. Rev. B 1973, 7, 4491.

35 J. Nelson, Phys. Rev. B 1999, 59 ,15374.

36 A. J. Frank. Coordination Chem. Rev. 2004, 248, 1165.

37 G. Schlichthörl, S. Y. Huang, J. Sprague, A. J. Frank, J. Phys. Chem. B 1997, 101, 8141.

38 N. W. Duffy, L. M. Peter, R. M. G. Rajapakse, K. G. U. Wijayantha, J. Phys. Chem. B 2000, 104, 8916.

39 F. Cao, G. Oskam, P. C. Searson, J. M. Stipkala, T. A. Heimer, F. Farzad, G. J. Meyer, J. Phys. Chem. 1995, 99, 11974.

40 B. A. Gregg, F. Pichot, S. Ferrere, C. L. Fields, J. Phys. Chem. B 2001, 105,1422.

41 N. Kopidakis, K. D. Benkstein, J. van de Lagemaat, A. J. Frank, J. Phys. Chem. B 2003,107, 11307.

42 S. Y. Huang, G. Schlichthörl, A. J. Nozik, M. Grätzel, and A. J. Frank, J. Phys. Chem. B 1997, 101, 2576.

43 A. Zaban, M. Greenshtein, J. Bisquert, ChemPhysChem. 2003, 4, 859.

44 E. Barsoukov, J. R. Macdonald. Impedance Spectroscopy: Theory, Experiment, and Applications, second edition, WILEY-INTERSCIENCE, A John Wiley & Sons, Inc., Publication 2005.

45 O. Heaviside, Electrical papers, 1894, 2, 504-518.

46 M. Grätzel, J. Photochem. and Photobio.C: Photochem. Rev. 2003, 4, 145.

47 Z. P. Zhang, PhD thesis "Enhancing the Open-Circuit Voltage of Dye-Sensitized Solar Cells: Coadsorbents and Alternative Redox Couples" EPFL, 2008.

48 J. Kr:üger, PhD thesis "Interface engineering in solid-state dye-sensitized solar cells", EPFL, 2003

49 J. Bisquert, Theory of impedance of electron diffusion and recombination in a thin layer, J. Phys. Chem. B 2002, 106, 325.

50 L. M. Peter, N. W. Duffy, R. L.Wang, K. Wijayantha, J. Electroanal. Chem. 2002, 127, 524.

51 Q. Wang, S. Ito, M. Grätzel, F. Fabregat-Santiago, I. Mora-Sero, J. Bisquert, T. Bessho, and H. Imai, J. Phys. Chem. B 2006, 110, 50.

52 R. de Levie, Advances in Electrochemistry and Electrochemical Engineering,

P. Delahay and C. T. Tobias, Eds. Vol. 6, p. 329, Interscience, New York 1967.

53 H. Z. Gerischer, Phys. Chem. NF 1951, 198, 298.

54 O. Contamin, E. Levart, G. Magner, R. Parsons, M. Savy, J. Electroanal. Chem. 1984, 179, 41.

Chapter 3 *Experiments*

3.1 Preparation of patterned TCO glass

Solar cells convert photon energy into electric energy, therefore good light harvesting is compulsory to minimize loss of incoming light. In my experiments, both photo and counter electrode are prepared on transparent conductive glass (TCO), particularly fluorine-doped tin oxide (FTO). FTO glass (Dyesol, TEC 15, thickness 3.2 mm, sheet resistance 15 Ω/sq.) which is firstly cleaned in a detergent solution (Decon. 90) in an ultrasonic bath for 10 min. It is then rinsed with deionized water and ethanol before it is further washed with acetone, ethanol and water, respectively, in an ultrasonic bath for another 10 min each. The cleaned FTO glass is then handled with tweezers and dried by nitrogen stream. The cleaned FTO is stored in cleaned Petri-dishes with conductive side face up and sealed by Parafilm before use.

The size of FTO sheets depends on the type of cells to be fabricated. Commonly, the size of FTO used as working or counter electrodes for a liquid-electrolyte system, is 2 cm × 2 cm. In contrast, larger size FTO is used in solid-state dye-sensitized solar cells. Usually, several cells are screen-printed on a patterned FTO. The counter electrode is typically prepared by gold sputtering or evaporation. For example, a piece of 3 cm × 5 cm FTO is first protected by covering it with a 2 cm × 5 cm Scotch tape layer, while the remaining 1 cm × 5 cm of FTO will subsequently

be exposed to HCl) The regions of the FTO, where the tin oxide should be etched away are then covered by zinc powder before the FTO is immersed in an excess of 12 M HCl for half an hour. As this leads to a significant H_2 evolution and bubble formation, the experiment is conducted in a deep beaker in a fumehood. The nascent H_2 reduces SnO_2 into Sn, which is then dissolved in HCl. The HCl treated regions of the FTO glass slide become insulating, while the tape-covered part remains conductive. After a patterned FTO is obtained, an addition of a compact TiO_2 blocking layer is usually achieved on conductive FTO either by spray pyrolysis as shown in Fig. 3-1 or by spin-coating a precursor TIP solution and subsequent annealing. Again, a rim of conductive FTO should be protected by Scotch tape (for spin-coating method) or a mask made of glass (for spray pyrolysis method) to prevent it from depositing compact TiO_2 on so as facilitate characterization after cell assembly. However, the sample prepared by spray pyrolysis is not uniform and protective to HTM. Therefore spin-coating is used as an alternative solution.

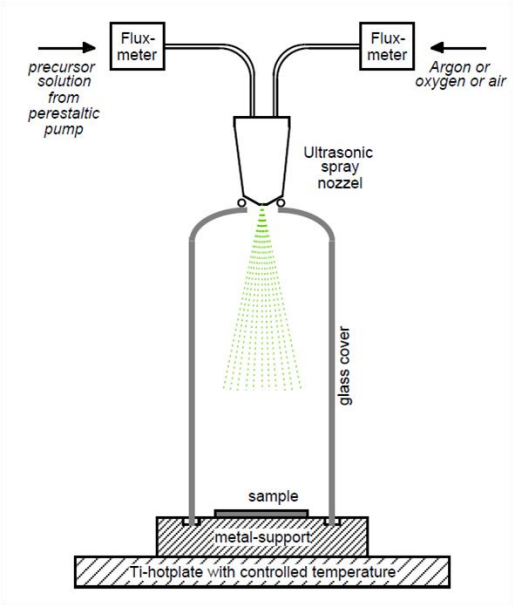

Figure 3-1: Typical spray pyrolysis setup with an ultrasonic nozzle. [1]

In a liquid electrolyte system, the blocking layer is helpful in impedance analysis by reducing FTO/electrolyte shunt effects and capacitance contributions from FTO/liquid electrolyte interface that tend to distort the Warburg diffusion in an intermediate frequency range typically spanning from 1000 Hz to 50 Hz (due to electron transport in mesoporous TiO_2). In the case of solid-state heterojunction cells, the role of a blocking layer becomes more prominent as it prevents short-circuiting of the device by a direct contact between FTO and hole-transporting medium.

3.2 Preparation of working electrode

In this thesis, two types of working electrode are used. Both electrodes consist of the anatase phase of TiO_2. TiO_2 nanoparticle-based DSCs are usually used as reference cells in my study to compare with the performances of the new, e.g. nanotube-based, cells. In order to prepare the working electrode for a nanoparticle-based DSC, pre-cleaned FTO is used as the starting material. The sample is dried and immersed into a covered beaker containing 40 mM of $TiCl_4$ solution maintained at 70 ℃ for 30 min before it is rinsed with deionized water and ethanol.

3.2.1 Growth of nanoparticle

So far the procedure is identical for both front-illuminated nanoparticle-based and nanotube-based dye-sensitized solar cells. Before detailed information of how to grow nanotube arrays is presented, a brief summary of the way to deposit

nanoparticles on FTO is given now. The glass is then secured on two sides by tape to enable screen printing on the glass using TiO_2 pastes in Fig. 3-2.

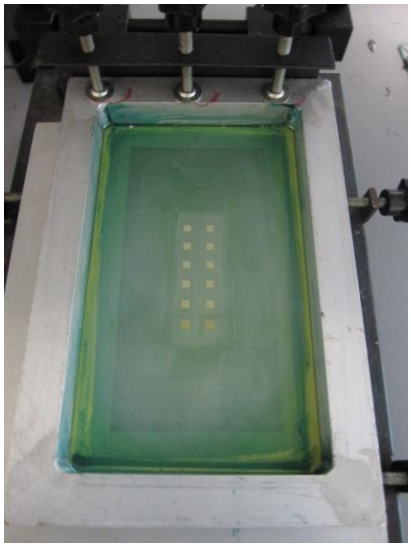

Figure 3-2: Screen printing mesh with sample holder beneath the mesh.

Two kinds of paste containing nanocrystalline TiO_2 are used in this preparation. The first paste, paste A (Dyesol, TiO_2 Paste DSL 18NR-T, transparent titania nanoparticular paste, particle size 20 nm) is applied on the conducting side of the glass and is allowed to relax for 3 - 4 min in a clean box before it is heated up to 125 ℃ for 6 min to evaporate the residual solvent. The printing procedure with paste A is repeated for another one (three) times to obtain a total thickness of the TiO_2 layer of about 5/(10) µm for the application of solid (liquid) DSC. Paste B (Dyesol, TiO_2 Paste DSL 18NR-AO, opaque titania nanoparticular paste, particle size 20-400 nm) is applied in the same manner, After the solvent is evaporated again at 125 ℃ for 6 min, the sample is subjected to a heat treatment under airflow at 325 ℃ for 5 min, at 375 ℃ for 5 min, at 450 ℃ for 15 min and at 500 ℃ for 15 min. The sample is then cooled down to room temperature before further treatment with $TiCl_4$ solution for another 30

min at 70 ℃. Thereafter it is rinsed with water and ethanol, and sintered at 500 ℃ for 30 min.

3.2.2 Growth of nanotube

In this thesis, both back and front side illuminated nanotube-based (NT) DSCs are attempted. The fabrication steps of the back-illuminated nanotube-based dye-sensitized solar cells are different from the ones in the front-illuminated devices. For the back-illuminated devices, the anodization is preferably conducted in a special setup made of PTFE, where only a defined window is available to expose Ti foil to NH_4F-containing electrolyte. In detail, the working electrode of the NT-DSC is prepared from a Ti foil (Aldrich, 99.7%, thickness 0.25 mm) which is cleaned by ultrasonification for 10 min in 0.5% Decon 90, acetone, ethanol, and deionized water in sequence and dried in nitrogen. The Ti foils are anodized under constant potential in a two electrode configuration with a Pt foil counter electrode at room temperature using a source meter (Keithley 236) as the power supply. A typical anodization electrolyte consists of a mixture of ethylene glycol and deionized water (in 49:1 volume ratio) containing 0.5 wt% NH_4F. Unless indicated otherwise an anodization potential of 50 V and an anodization time frame of 1-6 h is studied for anodes with a mask-controlled area of 0.384 cm^2. After anodization, the sample is rinsed in deionized water, ultrasonicated in alumina slurry containing DI water for 30 seconds and dried by nitrogen gas. The sample is then annealed at 200 ℃ for 15 min and 480 ℃ for 40 min in air in an oven to transform amorphous titania into anatase as seen

in Fig. 3-3. An intermediate step at 200 ℃ is to reduce the crack of nanotube arrays due to a rapid thermal treatment.

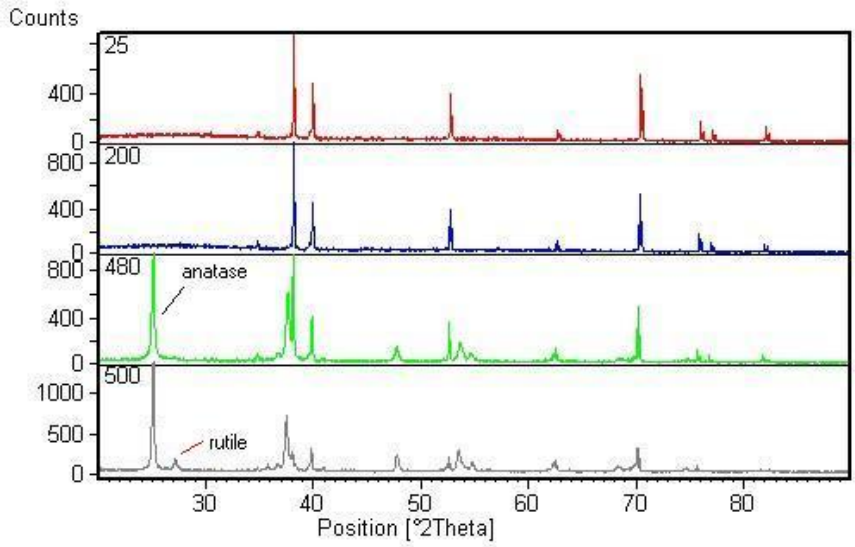

Figure 3-3: Effect of the annealing steps on the phase evolution in NT titania electrodes. No pronounced peak is observed for in-situ HTXRD until 200 ℃. However, a rutile peak is detected as temperature reaches 500 ℃.

In the course of the annealing at 480 ℃, the amorphous titania nanotubes are transformed into anatase (a= 3.786(1) Å; c = 9.510(2) Å). No trace of rutile is detected in the grazing incidence data (as seen in Fig. 3-3). The rutile phase can be observed when the thermal treatment extends to 500 ℃ indicating a start of phase transition. This rutile is probably located at the barrier layer between the NT titania and the titanium foil as the rutile peak is more pronounced measured in power XRD. Since the morphology of rutile TiO_2 is usually more porous and less connected after the phase transition, an optimum peak temperature of 480 ℃ is used in my study to grow large crystalline anatase TiO_2. Rietveld refinement is used to understand the crystal structure of the nanotube arrays treated by the optimized thermal profile in Fig 3-4.

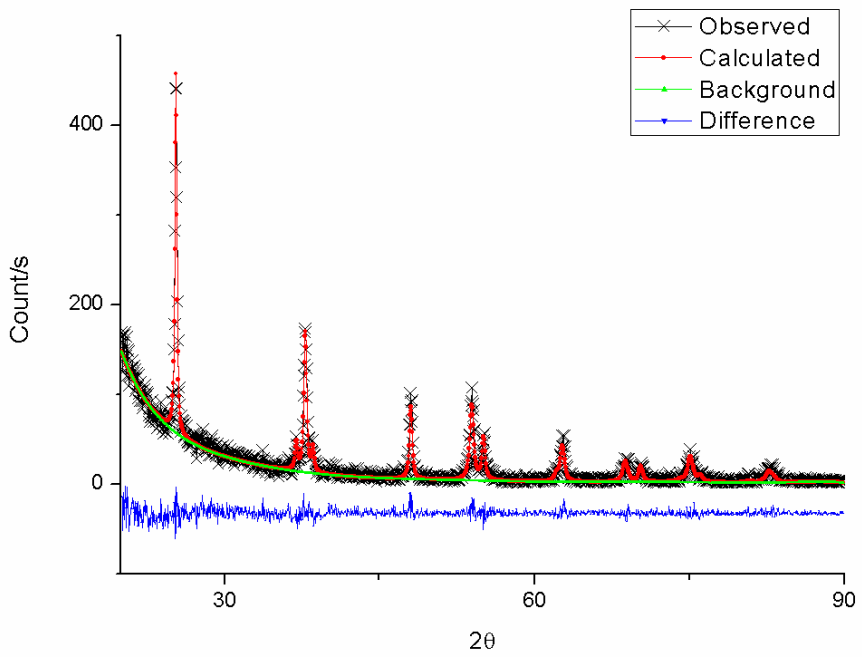

Figure 3-4: Grazing angle X-ray diffraction pattern of an annealed NT titania electrode at room temperature with an incidence angle of 3 °and its corresponding Rietveld refinement results.

The crystallite orientation in the nanotubes exhibits a moderate preferred orientation ([001] along the nanotube growth direction, March Dollase parameter = 0.790(8)). From the variation of the Bragg peak broadening, the anisotropic average crystallite size and strain have been refined. Along the [001] direction the crystallites show practically no size broadening, suggesting that the crystallite size along the growth direction is macroscopic (>> 100 nm, broadening parameters || 001 LX+ptec ≈ 0). The size broadening observed for the perpendicular directions formally indicates an average size of ca. 60 nm (LX = 14 centideg. after correction for instrumental resolution), which slightly exceeds the NT wall thickness (~50nm). This suggests that at a given height the entire circumference of the nanotube belongs to 1-2 crystallites. The elongated crystallites should be beneficial for electron transport along with the NT wall direction, resulting in a higher charge collection efficiency. The strain

component of the peak broadening parallel and perpendicular to the [001] direction is 1.3% (LY+ stec = 76 centideg) and 0.4% (LY = 22 centideg), respectively. Most of the stress caused by the fast crystal formation is relaxed in the direction perpendicular to the NT wall.

3.2.3 Front-illuminated nanotube-based DSC

There are two methods attempted to fabricate front-illuminated nanotube-based DSCs: direction method and transfer method. Direct method is to sputter a thin layer Ti on FTO first, the FTO with Ti film is then subject to anodization to grow nanotube arrays on it; Transfer method is an exploration of back-illuminated nanotube devise. The anodized Ti foil is anodized again after annealing to grow a sub-layer of new amorphous TiO_2 beneath the first layer. The first layer of TiO_2 nanotube arrays is then transferred and fixed onto FTO.

The direct method requires a sputtering system. Titanium is deposited by Radio Frequency Magnetic sputtering onto a FTO substrate (4 cm × 4 cm) that has been cleaned by Decon, acetone, ethanol and DI water 5 min each. The inner chamber wall of the sputtering system has to be cleaned by KimWipe with ethanol before use. The sputtering system is very sensitive to moisture contamination and vacuum level. Therefore, samples and chambers are not allowed to touch with bare hand. The cleaned and dried FTO is clamped onto a sample holder and placed in sample loading chamber. The sample is then transferred from the sample chamber to the sputtering chamber in vacuum. Before sputtering, the sputtering chamber is usually baked and evacuated overnight. A typical vacuum level required is 10^{-5} Pa before sputtering.

After the vacuum level is reached, pressure is adjusted to 0.8~1 Pa with Ar gas flow rate of 20 cm^3/min. Working pressure of 0.8 Pa facilitates the plasma generation while not slowing down the sputtering rate. The sputtering process is conducted at 400℃; the RF power is ca. 200 W. A Ti thin film of 1μm thick on FTO can be obtained by 3 h sputtering. The sample is cooled down after sputtering system is completed with the vacuum pump still on to prevent oxidation. As-cooled Ti is anodized at 50 V for 30 min with an initial ramp rate of 1 V/s. The electrolyte used in the anodization consists of NH_4F in ethylene glycol/water solution (same composition as described in previous section). To prevent peeling-off, the anodization has to be stopped immediately when the Ti foil in the active area is just converted into nanotube structure. This can be monitored visually as the point in time when the sample becomes transparent, which is followed by a sudden increase of the current (indicating the beginning detachment).

For transfer method, similar to that described in section 3.2.2. Titanium foil ($30 \times 15 \times 0.25$ mm, 99.7%) and fluorine-doped tin oxide (FTO 15 Ω/square, Dyesol) are cleaned in the sequence of 0.5% Decon 90, acetone, ethanol and deionized water 10 min each in an ultrasonic bath. In contrast to the case of nanotubes for back-illuminated DSCs, here the anodization is carried out in a PTFE beaker with most of the Ti foil immersed in the electrolyte. 0.6wt% NH_4F in ethylene glycol (EG, 99.8% anhydrous, Aldrich) with 2% vol. H_2O is used for anodization. The cleaned and dried Ti foil is immersed in the electrolyte with a platinum foil (0.125 mm, Aldrich) counter-electrode at a distance of 3 cm. Typically, a first anodization is conducted under 50 V for 0.5 - 6 h with an initial ramp rate of 0.05 V/s (see Fig. 3-5 (a, b)).

Ultrasonication for 30 s in a slurry of alumina powder [2] in DI water removes the debris on top of the nanotube layer. The as-anodized foils are then dried at 200 ℃ for 20 min, followed by annealing at 480 ℃ for 40 min in Fig. 3-5c. The annealed foils are anodized again under 70 V with a steeper initial potential ramp rate of 1 V/s. Under these conditions the membrane detaches from the Ti foil within one hour (see Fig. 3-5 (e, f)). To prevent that the membrane detaches completely and floats in the electrolyte, the immersion depth of the Ti foil is slightly reduced during the second anodization: thereby a well-defined rim of the nanotube membrane remains attached to Ti and facilitates subsequent handling of the membrane. The Ti metal foil with the essentially detached nanotube membrane is then transferred to an isopropyl alcohol (IPA) containing Petri dish.

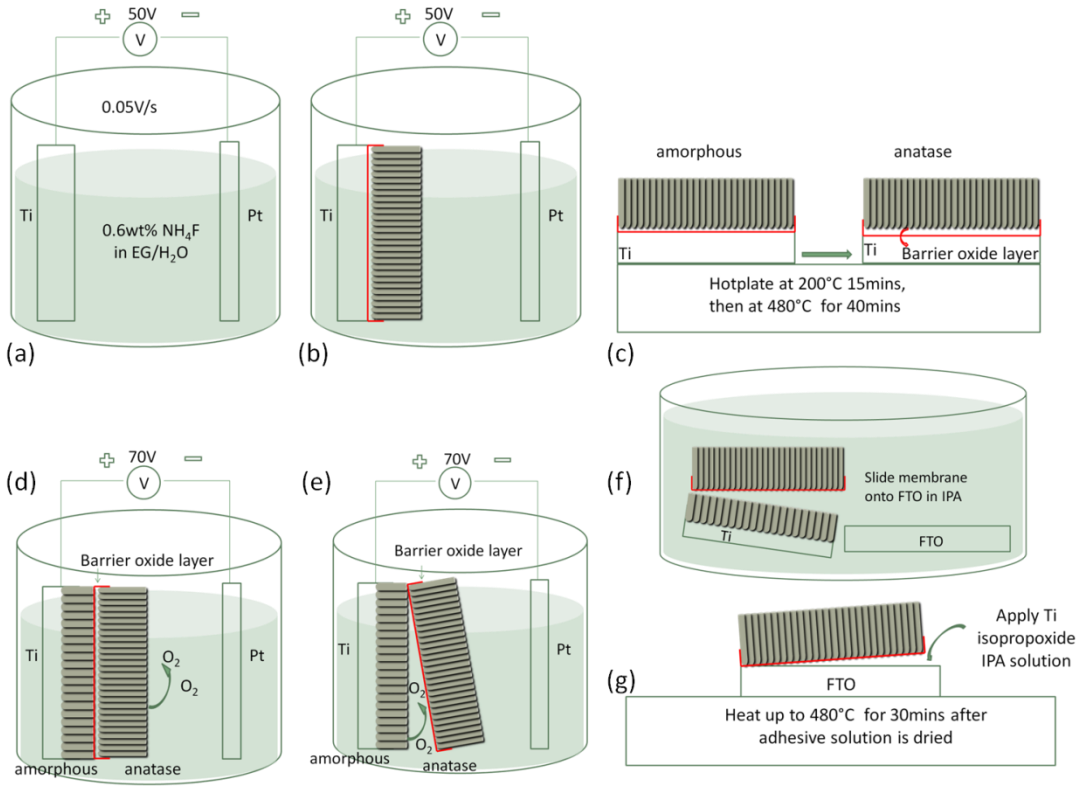

Figure 3-5: Flow-chart of membrane transfer by two-step anodization (sequence a-g);

Similar to that mentioned in section 3.1, 20 µl of a Titanium isopropoxide (97%, Aldrich) solution in IPA with Triton X-100 (Aldrich) and acetic acid in volume ratio 1:20:4:2 are spin-coated at 3000 rpm on a 1.5 cm × 1.5 cm portion of a 2 cm × 2 cm FTO glass for 1 min (The rims are covered to facilitate the cell characterization). The coated FTO is annealed at 450 ℃ for 30 min to form a 50 nm buffer layer of anatase that facilitates the later adhesion of the nanotube membrane and inhibits recombination between FTO and electrolyte. Details of the membrane transfer are presented in the results section together with cell assembly procedures. The annealed spin-coated FTO is then immersed in the IPA containing Petri dish that contained the nanotube membrane. By just tilting the metal foil, the titania nanotube membrane gently slides down onto the FTO in IPA in Fig. 3-5f. The membrane transfer is conducted in IPA rather than in air to minimize the surface tension and damage to the membrane. This procedure also avoids damages by any mechanical action on the membrane (e.g. by tweezers). The membrane-FTO stack is then removed from IPA and two drops of the above-mentioned isopropoxide IPA solution are applied to the side of the membrane. Infiltration of the titanium isopropoxide IPA solution between anatase buffer layer and nanotube membrane fixes the membrane on the FTO. The attached nanotube layer is subsequently heated to 200 ℃ for 15 min, and finally annealed at 480 ℃ for 30 min (cf. Fig. 3-5g).

3.3 Preparation of hole transporting medium

The redox system is another significant component in DSC as it helps to regenerate the dye molecules from donated state to original state. Fast dye regeneration and slow

electron recombination are two typical requirements for the system. In a liquid-electrolyte system, a commonly employed electrolyte composition is 0.6 M 1-methyl-3-propyl-imidazolium iodide (PMII), 0.03 M I_2, 0.1 M guanidinium thiocyanate (GuSCN), 0.5 M 4-tert-butylpyridine (tBP) in acetonitrile and valeronitrile (85:15). PMII and I_2 are core elements in redox system as they define the concentration of I_3^- /Γ, GuSCN and tBP can improve open-circuit voltage by either aligning dye molecules in well-defined orientation to screen TiO_2 from cations or modifying the surface of TiO_2 so as to effectively shift conduction band upward in the electron energy scale.

In all-solid-state cells the dye regeneration is achieved by transporting the hole away from the dye to the counter electrode via a p-type conductor (hole transport medium, HTM). To prepare the HTM α-CuSCN, β-CuSCN, $Cu(SCN)_2$ and $Ni(SCN)_2$ are dissolved in dipropyl sulphide (PS) [3] to produce saturated stock solutions two days before use. While in the dissolved state the structural difference between the α- and β-phase should not play any role, their synthesis methods and hence the impurities will differ. In that context we suspect that residues of LiSCN (undetected in XRD) from the synthesis of α-CuSCN may play a significant role in enhancing its conductivity. α-CuSCN/$Cu(SCN)_2$ are precipitated [4] from aqueous solutions of 0.25 M LiSCN and 0.4 M $Cu(ClO_4)_2$ with or without the addition of a triethylammonium acetate buffer solution. Volume ratio between triethylammonium acetate buffer solution and water remains 1:4. $Ni(SCN)_2$ is precipitated from 0.1 M NH_4SCN and 0.04 M $NiCl_2$ aqueous acetic acid solution. The solvent is made of a mixture of glacial acetic acid and DI water in a fixed vol. ratio of 10:1. After mixing, the

precipitates are filtrated, rinsed (here use solvent to rinse due to high solubility of $Ni(SCN)_2$ in DI water) and dried in a vacuum oven at 80 ℃ over night. Triethylammonium thiocyanate (THT) [5,6] is prepared by mixing NH_4SCN (1 g) with excess triethylamine (3.66 ml) at 100 ℃ with vigorous stirring. After completion of the reaction the bottom layer is sucked out by a dropper. (The density of THT is larger than that of the remaining triethylamine) The optimized recipe for solution casting of the HTM is to add 0.2 mM THT into a mixture of α-CuSCN, $Ni(SCN)_2$ and β-CuSCN saturated solutions in PS (vol. ratio 1:1:10). Additional 10% vol. PS is added to allow for good reproducibility.

The dye-coated photoelectrode is placed on a 45 ℃ pre-heated hotplate. The active area of the 5 μm thick photo-electrode is 0.25 cm^2. A drop (2.5 μl) of as-prepared solution is evenly spread on the titania layer. At least 10s are allowed in-between each casting to allow for the solution drop to penetrate into TiO_2, the solvent to evaporate and the HTM to nucleate. This process is repeated 50 times at 45 ℃; then the temperature is raised by 5 ℃ every five drops from the 50^{th} to the 70^{th} drop. This turned out to be crucial as the first 50 castings at a lower temperature allow for better pore-filling, while increasing the temperature at the later stage ensured a more complete coverage. The surface temperature of the hotplate is monitored by an infrared temperature sensor. The optimized number of drops and volume per drop obviously varies with the active area and layer thickness. The samples are finally dried in vacuum oven over night before measurement.

3.4 Cell assembly

For liquid system, the samples after heat treatment in previous sections are then cooled down to room temperature before further treatment with $TiCl_4$ solution for another 30 min at 70 ℃. After it is rinsed with water and ethanol, it is sintered at 500 ℃ for 30 min. After cooling to room temperature, the sample is immersed completely into a solution of N3 dye solution (Dyesol, N3 dye) and kept in the dark overnight. Thereafter it is rinsed with acetonitrile and dried with nitrogen gas before it is ready for assembly.

Platinum coated transparent glass is used as a counter electrode. A hole is drilled into a FTO glass plate (TEC 15 Pilkington North America, Inc.) by a glass cutting bit for the electrolyte injection. The substrates are cleaned as described for the Ti foils. The cleaned FTO substrates are sintered at 400 ℃ for 15 min to remove residual organic contaminants. A drop of H_2PtCl_6 solution (2 mg Pt in 1 ml ethanol) is spread on the FTO glass and heat treated at 400 ℃ for 15 min. The titania electrodes and Pt electrodes are assembled and sealed by Surlyn-30 thermoplastic sealant (Dyesol). A drop of electrolyte composed of 0.6 M 1-methyl-3-propyl-imidazolum iodide (PMII), 0.03 M I_2, 0.1 M guanidinium thiocyanate (GuSCN), 0.5 M 4-tert-butylpyridine (tBP) in acetonitrile and valeronitrile (85:15) is placed on the hole in the counter electrode and is sucked into the cell via vacuum filling. Finally the hole is sealed using the sealant and a cover glass. A brief schematic description is given in Fig. 3-6.

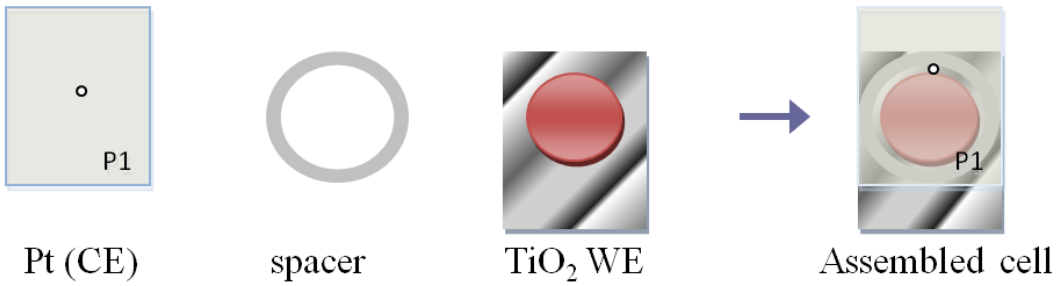

Figure 3-6: Assembly process of DSC with titania nanotubes [7].

An analogous assembly process also applies for NP-based dye-sensitized solar cells. In contrast to the liquid electrolyte system, the non-active area is, however, protected by a layer of scotch-tape after complete solvent evaporation. (See previous section 3.3) Since the drying process of the deposited inorganic hole-transporting medium takes one day, the cell assembly of a solid-state cell continues from the moment where HTM is fully nucleated and dry.

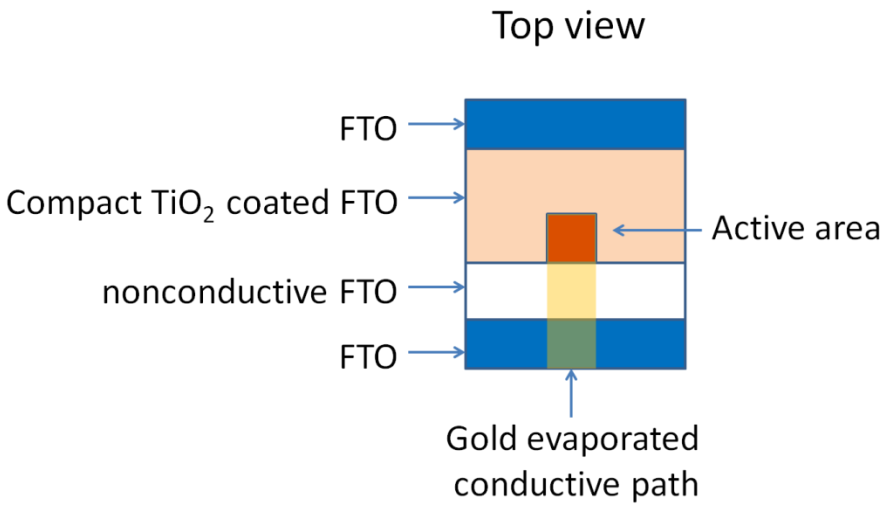

Figure 3-7: A schematic diagram of the location of different component in SSDSC on a patterned FTO, the top FTO is acting as a contact point for photoelectrode, the bottom FTO is counter electrode.

Now, I have explored two other ways to coat the counter electrode, by graphite or by gold: the samples are protected by a mask in a gold evaporator. Gold is evaporated and only coated on a mask-defined path, which connects the HTM to a conductive rim of the glass. A nonconductive strip separates the photo-electrode and counter electrode on the same FTO glass sheet by Zn/HCl patterning described in section 3.1. It proved to be advantageous to apply gold counter electrodes on samples with patterned FTO. In this case, there is only one piece of FTO glass sheet required for a sample as shown in Fig. 3-7. However, this method does not work well in my experiment due to a limited access to evaporator and reproducibility concern. Alternatively, a cheaper and more flexible method is applied. The graphite powder counter electrode is easy to handle, and no pre-patterning on photoelectrode FTO is required. A thin layer of fine graphite powder is evenly spread and covered on top of the CuSCN layer when the non-active area is covered a layer of Scotch tape. The graphite powder is then covered by another conductive glass slide and the cell is clamped by clips for a quick measurement or sealed by epoxy resin for stability tests.

3.5 Characterization

Scanning Electron Microscope

The morphology of the NT electrodes is studied by field-emission scanning electron microscopy on a Zeiss FE SUPRA40 SEM (Fig. 3-8). From top view micrographs the inter-pore distance, wall thickness, inner tube diameter and outer tube diameter can be analysed. Bottom views are employed to check whether the tube bottom is closed or

open-ended. The nanotube length can be observed from side view pictures (or alternatively, measured by a KLA Tencor surface profiler (Fig. 3-9). The results given by these two approaches are found to harmonize well. Other than for measuring the nanotube thickness, the same surface profiler is also used to measure the thickness of the compact TiO_2 layer, deposited CuSCN layer and miscellaneous other length determinations. The surface profiler measurement is fast and convenient, but destructive to the measured samples.

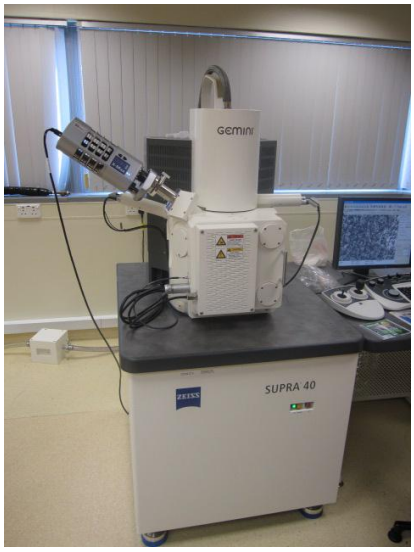

Figure 3-8: Zeiss Supra 40 Scanning electron microscopy.

Figure 3-9: KLA Tencor Alpha-step IQ surface profiler.

X-ray Diffraction

The crystal phase evolution of the NT titania electrodes induced by annealing is monitored using X-ray powder diffraction (PANalytical, X'Pert Pro MPD) equipped with a high temperature chamber (ANTON PAAR, HTK 1200). To minimize the interference of the Ti substrates, additional room temperature grazing incidence angle XRD patterns of the NT titania electrode are recorded using a Bruker D8 Advanced Thin Film XRD with a fixed incidence angle of 3 °. Both types of XRD patterns are analyzed by Rietveld refinement using GSAS software [8]. (see Fig. 3-10)

Figure 3-10: X-ray powder diffraction (PANalytical, X'Pert Pro MPD) equipped with a high temperature chamber (ANTON PAAR, HTK 1200) (left); Bruker D8 Advanced Thin Film XRD with incidence angle of 3 °(right).

I-V measurement & Incident Photo-to-Electric Conversion Efficiency

DSCs are illuminated by a 150W NREL traceable Oriel Class AAA solar simulator (Model 92250A-1000). Current density-voltage characteristics are measured using a Keithley sourcemeter 2420 to record the cell performance. (see Fig. 3-11) Incident photon-to-current conversion efficiency (IPCE) of the DSCs is

measured by a DC method. The light from a 300W Xenon Lamp (Oriel 6258) passed through a monochromator with a resolution of 10 nm (Cornerstone 260 Oriel 74125) to select a single wavelength. (Fig. 3-12)

Figure 3-11: JV curve measurement using computer controlled Keithley and solar simulator

Figure 3-12: IPCE measurement setup using computer monitored monochromator.

Light intensity is measured by a NREL traceable Si detector (Oriel 71030 NS) and the short circuit current of the DSCs is measured by an optical power meter (Oriel

70310). Short circuit current density J_{sc} can be calculated by integrating the IPCE over the AM 1.5G irradiance spectrum. In our experiments, the calculated J_{sc} is close to that measured in the JV curves, indicating that the mismatch factor of our solar simulator is close to unity.

Electrochemical Impedance Spectroscopy & Cyclic Voltammetry

Electrochemical impedance spectroscopy (EIS) and cyclic voltammetry (CV) measurements are performed using an ECO CHEMIE Autolab (PGSTAT 302N with/without FRA2) as shown in Fig. 3-13. The photoelectrodes are used as the working electrode, the Pt/graphite/gold electrodes as counter and reference electrode. The EIS measurements at different forward bias potentials in dark are conducted in the frequency range of 10^{5} -10^{-1} Hz and an ac amplitude of 10 mV (V_{peak}). The impedance data are fitted using ZView program (ScribnerAssociates, USA). [9]

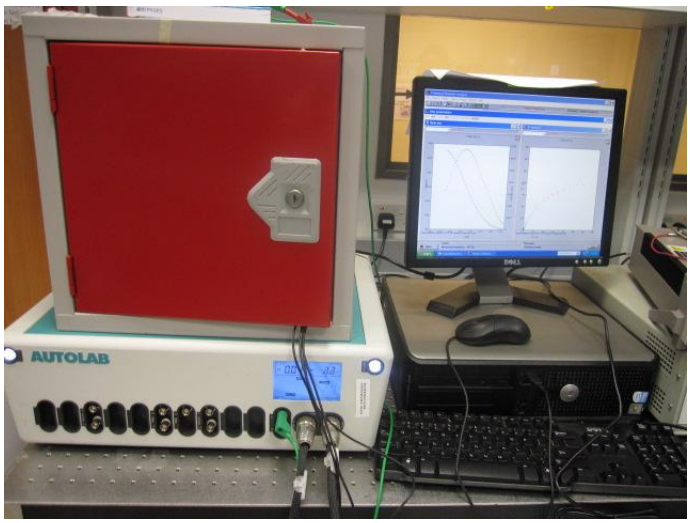

Figure 3-13: Computer monitored Autolab 302N + FRA for impedance measurement.

References

1 U. Bach, Solid-state dye-sensitized mesoporous TiO_2 solar cells, PhD thesis 2000, EPFL.

2 D. Kim, A. Ghicov, P. Schmuki, Electrochem. Commun. 2008, 10, 1835.

3 G. Kumara, A. Konno, G. Senadeera, P. Jayaweera, D. De Silva and K. Tennakone, Sol. Energy Mater. Sol. Cells 2001, 69, 195.

4 B. O' Regan, S. Scully, A. C. Mayer, E. Palomares and J. Durrant, J. Phys.Chem. B 2005, 109, 4616.

5 Q. B. Meng, K. Takahashi, X. T. Zhang, I. Sutanto, T. N. Rao, O. Sato, A. Fujishima, H. Watanabe, T. Nakamori and M. Uragami, Langmuir, 2003, 19, 3572.

6 E. Premalal, G. Kumara, R. Rajapakse, M. Shimomura, K. Murakami and A. Konno, Chem. Comm. 2010, 46, 3360.

7 A. Jakub, Performance and Grid Compatibility of Dye Sensitized Solar Cells under Varying Environmental Conditions, thesis of final year project, NUS, 2009.

8 A. C. Larson and Von Dreele R.B., "General Structure Analysis System (GSAS)", Los Alamos National Laboratory Report LAUR 1994, 86.

9 J. Bisquert, J. Phys. Chem. B 2002, 106, 325.

Chapter 4 *Nanotube-based DSC*

Nanostructured semiconductors such as TiO_2 have a great potential in photoelectrochemical devices due to large effective light-harvesting interface area and wide band gap. Anodization of Ti is a simple way to prepare well-ordered nanostructured TiO_2 in the form of vertically oriented titania nanotube arrays. Compared to unordered nanoparticles, nanotube arrays facilitate charge transport along the tube direction [1,2] while maintaining a high effective surface area. Titania nanotubes are thus suitable for a variety of applications, including sensors, [3] water photoelectrolysis, [4] photovoltaic devices, [5] photocatalytic CO_2 reduction,[6] supercapacitors, [7] etc. and their use as photoelectrode in photovoltaic devices can help to boost the efficiency. Therefore, titania nanotube growth by anodization has been studied widely in literature. [8]

In order to form a well-ordered tubular structure with controlled morphology, a balance between oxidation and field-assisted dissolution has to be maintained by adjusting electrolyte concentration, temperature, anodization duration, ramp rate and magnitude of potential [9].

In this chapter, my findings on optimising liquid electrolyte DSCs based on TiO_2 nanotubes are summarized. This includes the optimisation of anodization potential, ramp rate and duration on the tube morphology. (See section 4.1). Moreover, the anodization procedure is optimised, such as electrolyte with respect to

the electrolyte solvent, functional additives, electrolyte storage and repeated use of the same electrolyte (section 4.2).

Section 4.3 focuses on the optimisation of back-illuminated nanotube-based DSCs, whereas sections 4.4 and 4.5 discuss two approaches to fabricate titania nanotube arrays on FTO and the performance optimisation of front-illuminated DSCs based on these.

4.1 Study of the effect of anodizing potential

In this section, the effects of anodization working potential, potential ramp rate and two-stage anodization on a patterned structure will be discussed.

A typical nanotube array anodized at 50 V with an initial ramp rate of 1 V/s by using the electrolyte (0.5wt% NH_4F in ethylene glycol/water solution, 49:1 in volume) for 1 h is of 7 μm in length, 22 μm (out of 0.25 mm Ti foil) in barrier layer thickness and 65/120 nm as the inner/outer diameter. Earlier work in our group demonstrated that the nanotube length and diameters generally vary with the applied potential and duration of anodization as shown in Fig. 4-1. For the electrolyte composition described above, the maximum potential that can practically be applied is limited to 60 V, as we find that samples anodized at a potential equivalent to or larger than this potential are very likely to peel off from the Ti foil and crack.

If the field-assisted oxidation process is too fast the mismatch stress/strain generated at the interface between oxide and metal cannot be relieved in time and

cracks are initiated at the metal/oxide interface finally leading to the peeling-off and destruction of the membrane.

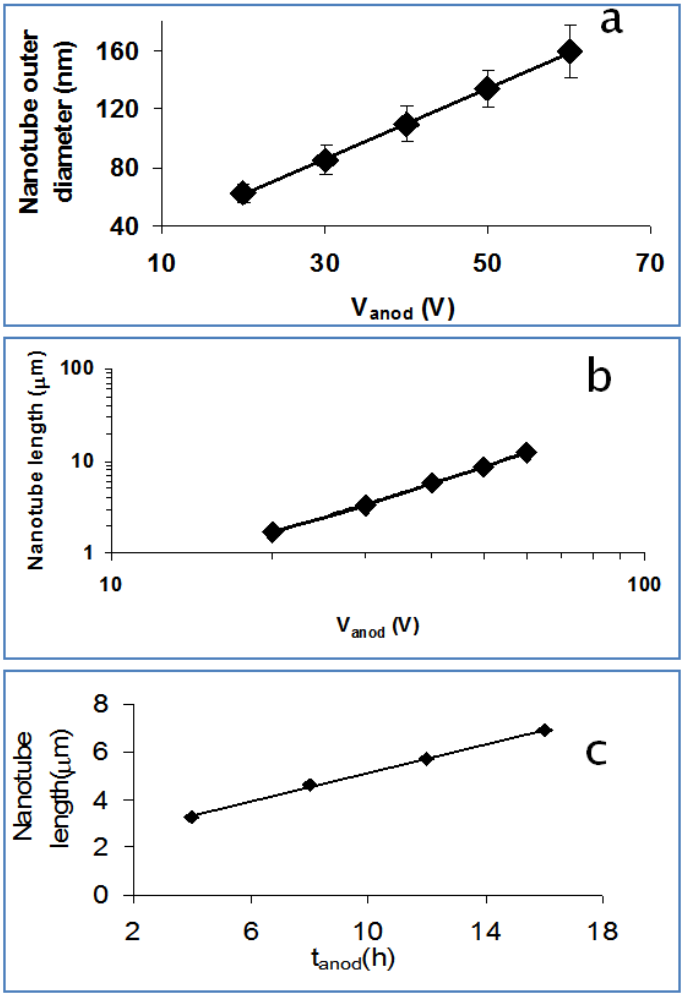

Figure 4-1: Effects of anodization potential on nanotube diameters (a) and length (b); Effect of anodization duration on tube length is given in (c). Adapted from [10]

The effect of the initial potential ramp rate on the morphology of the produced TiO_2 nanotubes is demonstrated in Fig. 4-2. SEM micrographs of samples that have been anodized for the same time in the stationary stage (50 V) after increasing the potential with different ramp rates show that the potential ramp rate affects the outer diameter of the nanotubes.

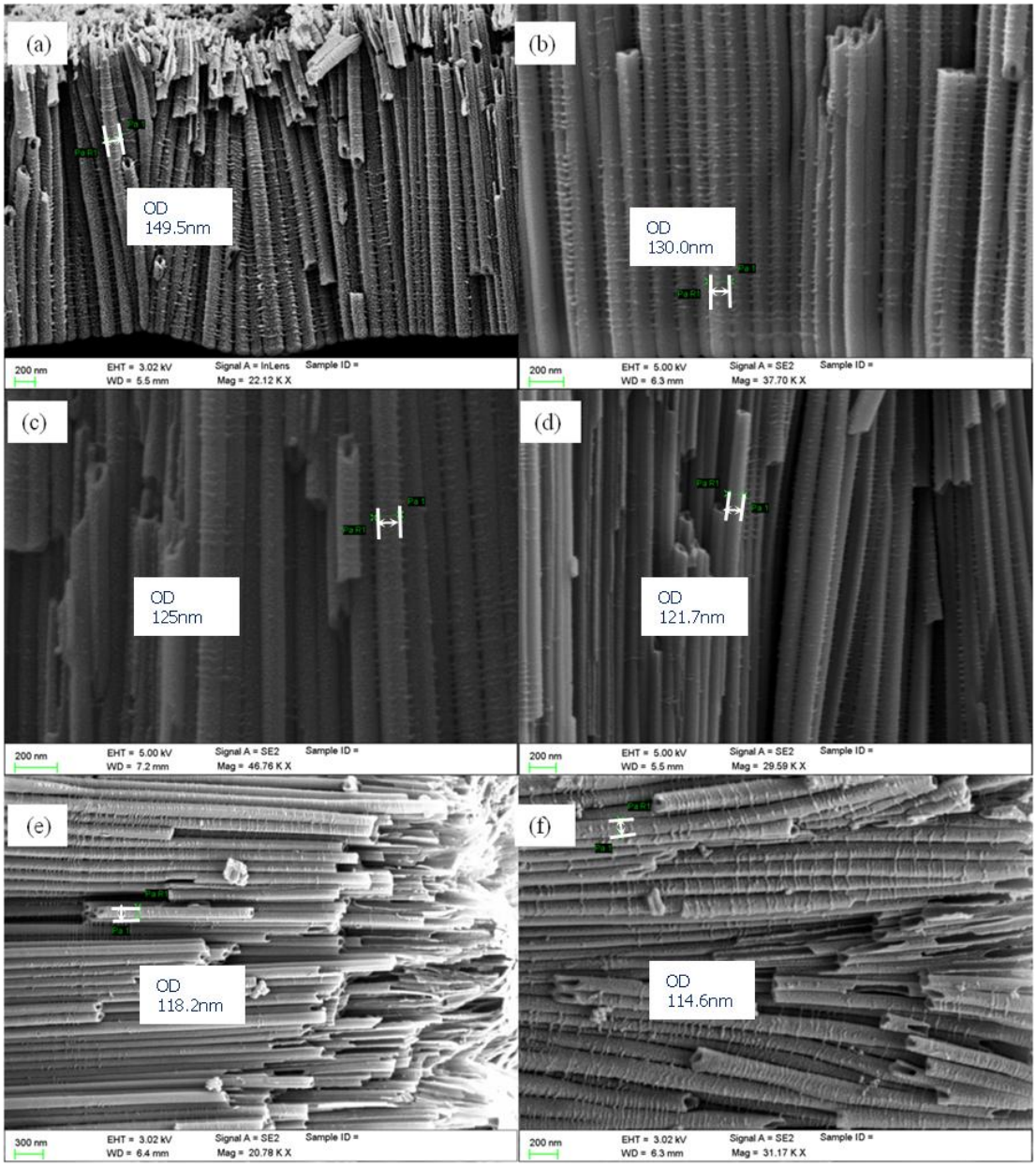

Figure 4-2: Side view pictures of titania nanotube arrays prepared by the same electrolyte with different potential ramp rate from 0.05 V/s (a), 0.1 V/s (b) 0.25 V/s (c), 0.5 V/s (d), 5 V/s (e) to 10 V/s (f), the tube outer diameter drops from 150 nm (a), 130 nm (b), 125 nm (c), 121 nm (d), 118 nm (e) to 114 nm (f)

Obviously, the ramp rate affects the thickness and morphology of the oxide during the initial stage of anodization. Usually, the initial stage is defined as the period from the start of the anodization until current density ceases to increase. From

this point of view, a higher ramp rate results in larger effective current density (higher peak current density) at initial stage (for a fixed period). It has been shown that the tube spacing is inversely proportional to the strain energy stored in the film. Accordingly, samples anodized by 50 V with the highest ramp rate (10 V/s) produce oxide films with a denser packing of slightly thinner nanotubes, due to a larger amount of stored strain energy. Thus the smallest tube diameters should be expected which is in good agreement with our experimental results in Fig. 4-2. In the other end, the slowest ramp rate of 0.05 V results in the largest outer tube diameter (From a-f, tube diameter and inter tube spacing decreases when ramp rate increases).

After all, the tubes formed using the lowest potential ramp rate are more evenly distributed on the oxide surface with larger spacing, and smooth surface and less cracks are discovered from top view pictures. This may be partially attributed to a more stable current density (Fig. 4-3) experienced during anodization as a consequence of the smaller potential ramp rate. The optimum ramp rate is determined by a trade-off between the high aspect ratio for high ramp rates and the improved organization, alignment and micro structural stability for nanotube membranes produced with lower ramp rates. Typically, the optimum ramp rate during anodization for back-illuminated nanotube-based dye-sensitized solar cell is 1 V/s; while the one for front-illuminated nanotube-based DSC is 0.05 V/s at stage one followed by 1 V/s in the second anodization. The reason of choosing a lower ramp rate at stage one in front-illuminated cell is because there is a limit of current supply when a larger Ti foil is used. (Consider that membrane is easy to detach and the method becomes more

efficient) The detailed discussion on optimization of 2-step anodization method is given in later section 4.4.

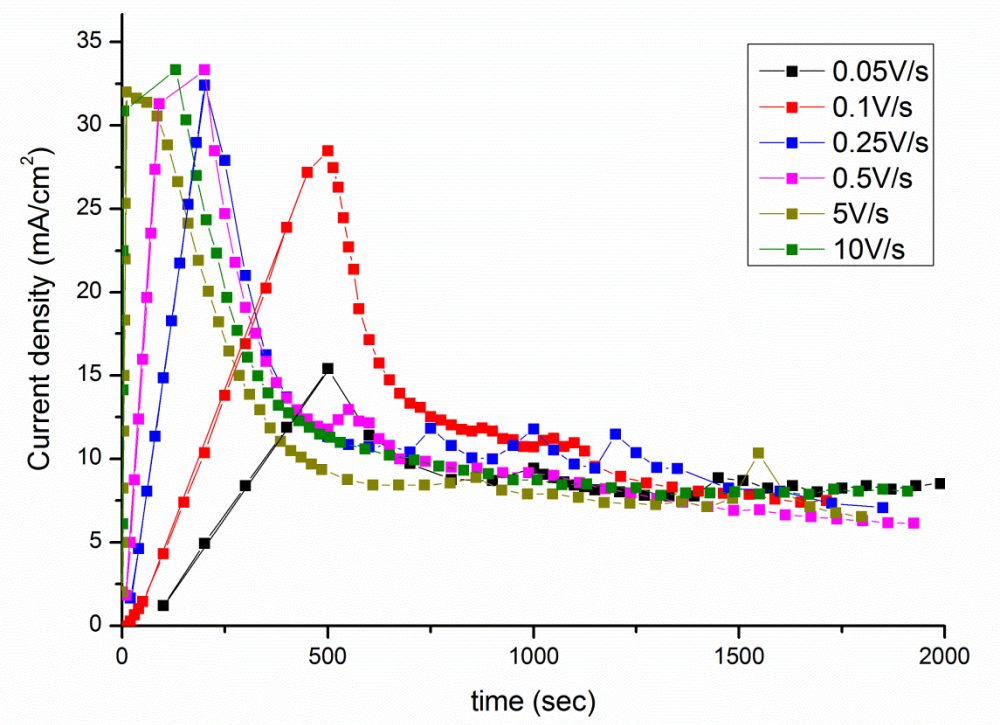

Figure 4-3: Current density-time profiles (a) of the samples anodized with an initial potential ramp of 0.05 V/s (black), 0.1 V/s (red) 0.25 V/s (blue), 0.5 V/s (magenta), 5 V/s (dark yellow) to 10 V/s (olive), the peak current tends to increase with increased potential ramp until a current plateau is reached due to the current limit of the DC power source (Keithley 236). Note that the current limit is exceeded only for the final stage of the 5/s and 10 V/s ramps.

Other than potential ramp, potential profile in the stable stage also greatly contributes to the morphology of nanotube arrays. Therefore, 50 V and 60 V are selected as working potentials to further study the detailed effects of anodization potential on tube morphology and their optimisation for application in dye-sensitized solar cells. Moreover, we also tried to manipulate the tube structure by applying step potentials during the anodization.

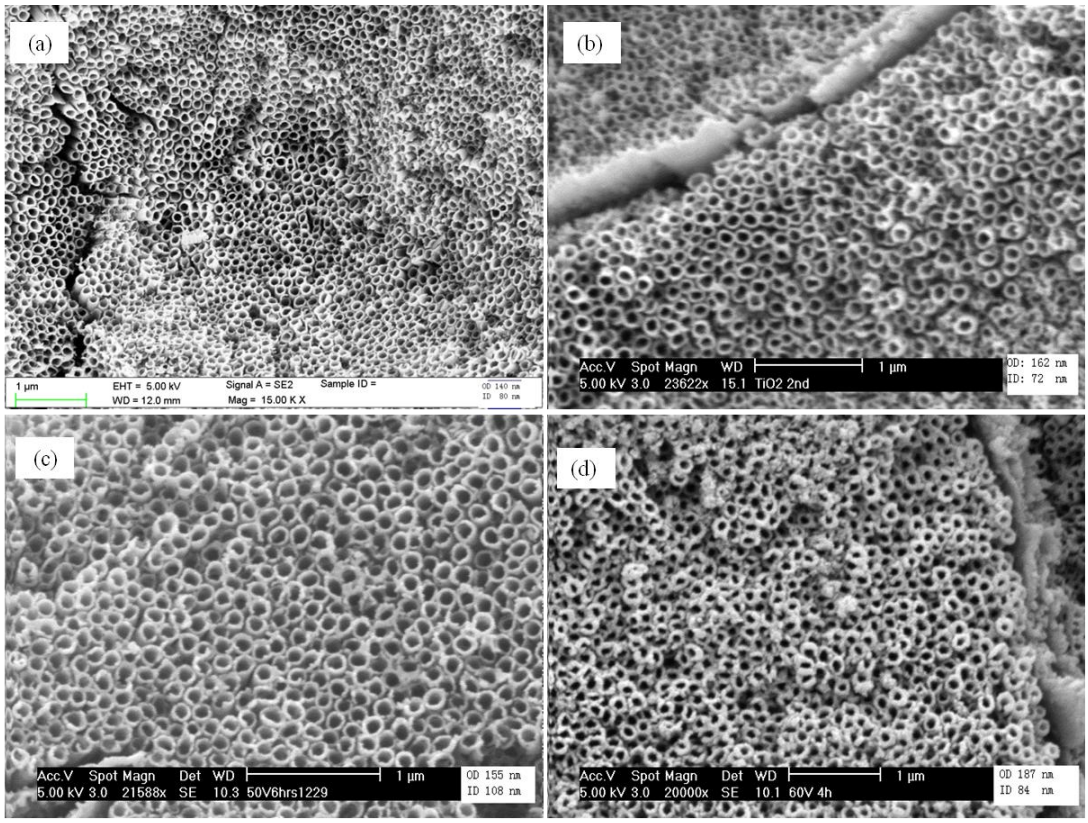

Figure 4-4: Top view of nanotubes on Ti foil after 2h anodization with the same initial ramp. The applied potential profile is (a) constant 50V; (b) 40V 40min→50V 40min→60V 40min; (c) 60V 40min→50V 40min→40V 40min and (d) constant 60 V. The inner and outer diameter of respective sample is displayed in each picture.

For example, applying a higher potential at the initial stage and then gradually decreasing the applied potential to a lower value, and vice versa. Compared to 50 V, the nanotube membrane anodized at 60 V consists of longer nanotubes with larger inner and outer diameters when other working conditions are kept constant (Fig. 4-4 a, d). In another words, the nanotube array produced at 60 V is not as closely packed as the one fabricated at 50 V. For 60 V, longer tube length would usually compensate the loss in effective tube area due to loosely packed structure. However, a longer tubular structure may suffer from collapse after anodization and short-circuit

problems in cell fabrication. (As seen in Fig. 4-5, the short circuit current of a sample anodized at 60 V is higher while ff is much lower indicating local short condition).

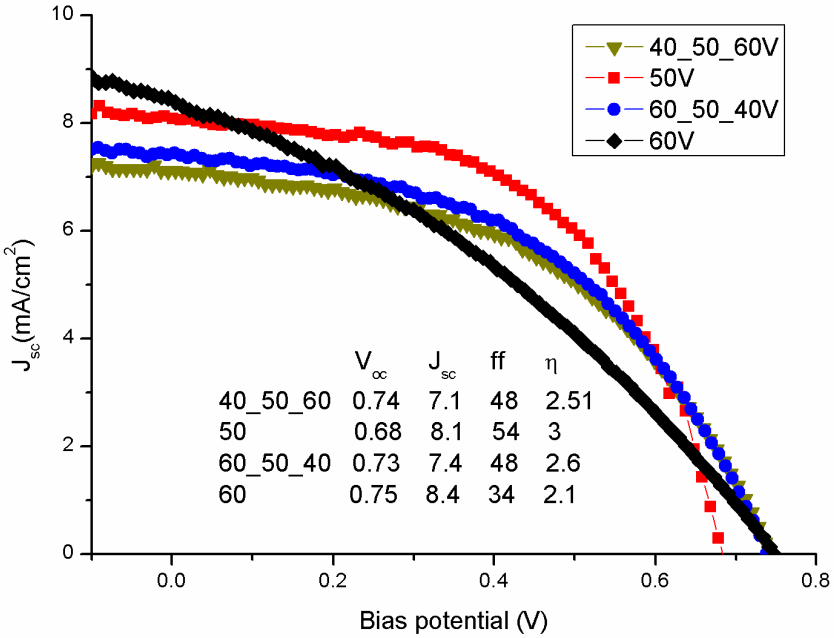

Figure 4-5: JV curves of nanotube-based dye-sensitized solar cells. The nanotubes are anodized for 2 h. One potential profile is 40→50→60V and each potential maintain for 40 min, another potential profile is a reverse case that sample is anodized at 60→50→40V in sequence and each potential maintains for 40 min. The rest two samples are anodized at 60V and 50 V respectively for 2 h.

Alternatively, increasing and decreasing potential step profiles are explored for Ti anodization. Nanotubes anodized at 60, 50 and 40 V for 40 min each in sequence exhibit a reduced wall thickness compared to the case using the reverse potential profile and thereby a larger effective area for dye adsorption in DSC application. While, the advantage of nanotubes prepared at 40, 50 and 60 V for 40 min each in sequence is the more stable tube architecture. The performances (under STC) of nanotube-based DSC prepared by above mentioned working potential profiles are given in Fig. 4-5. The comparison of tube length, diameters and photovoltaic

performance of the cells fabricated at different anodization condition are summarized in Table 4-1.

Table 4-1: The length, diameters and JV performance under illumination of the cells fabricated by different anodization profile.

Anodization Profile (V)	Length (μm)	Inner/Outer Diameter (nm)	V_{oc} (V)	J_{sc} (mA/cm^2)	FF (%)	η (%)
40→50→60	9.6	72/162	0.74	7.1	48	2.5
50	12	80/140	0.68	8.1	54	3.0
60→50→40	10	108/155	0.73	7.4	48	2.6
60	14	84/187	0.75	8.4	34	2.1

Cell efficiency of the sample prepared by 60→50→40 V anodization is slightly higher than another sample prepared by 40→50→60 V due to slightly longer tube length. As we know, V_{oc} is defined as the difference between quasi-Fermi level and redox potential. However, it also reveals the effective interface area where recombination process takes place. Accounting for tube structure stability, effective inner tube area and tube length, we find out that the best working potential is 50 V without step potential during the anodization. A relative lower V_{oc} of the sample prepared by 50 V is also attributed to a more close-packed structure. Further increase in working potential usually leads to nanotube crack and a partial collapse of the tube structure. So far, the optimized anodization potential remains at 50 V, and the optimized electrolyte composition is 0.6 wt% NH_4F in ethylene glycol/water (49:1 in volume). A more detailed study of effects of variations in the nanotube length can be found in section 4.3.

4.2 The effect of anodizing electrolyte

As discussed in chapter 2, an acidic environment is not sufficient to grow self-ordered titania nanotubular structure when anodizing a Ti foil, as the presence of fluoride in the electrolyte is necessary. In my study, NH_4F is selected as the solute because the NH_4^+ cation is effective in reducing the barrier layer and buffering the pH value of the solution. Moreover, NH_4^+ can form $(NH_4)_2TiF_6$ on top of TiO_2 to slow down both oxidation and dissolution process. The etching tends to be not as aggressive as using KF or NaF. In the end, considering all the effects mentioned and safety concern, NH_4F is selected for further study. Solvents glycerol, dimethyl sulphoxide (DMSO) and ethylene glycol (EG) are selected in this study to understand their effects on tube morphology after anodization. 2% vol. water as the source of oxygen is added to all solvents and a NH_4F concentration of is 0.5 wt% in uniformly used in this section. The samples are anodized at 50 V with potential ramp rate of 1 V/s for 1 h. The results shown in Fig. 4-6 demonstrate the effect of solvent on the formation of titania nanotube arrays when all other anodization parameters are kept constant.

Under these working conditions anodization in DMSO does not yield a nanotube membrane but a relatively compact columnar microstructure (see Fig. 4-6 (c, f)). Nanotube membranes by anodization in DMSO are reported by Ruan *et al.* [11], who used HF as the fluoride source. As a technique based on HF is improbable to find wide application due to the safety hazards involved, this has not been further explored in this work. During the anodization in NH_4F-containing DMSO, the formation of a white suspension in the electrolyte, which indicates the low solubility of NH_4F in pure DMSO leads to a phase segregation into an aqueous NH_4F phase and

a DMSO phase. The viscosity of glycerol is much higher than that of ethylene glycol; therefore the anodization current is drastically suppressed, as the high viscosity limits the transport rate of oxygen and fluoride ions to the metal/oxide interface. In consequence, the nanotubes grown in glycerol are shorter and their wall thickness is larger (see Fig. 4-6 (b, e)). Therefore, works presented in the later part of the thesis focuses on anodization in ethylene glycol as the tube growth is more efficient in a given amount of time, and a well-defined high aspect ratio tubular structure can be formed.

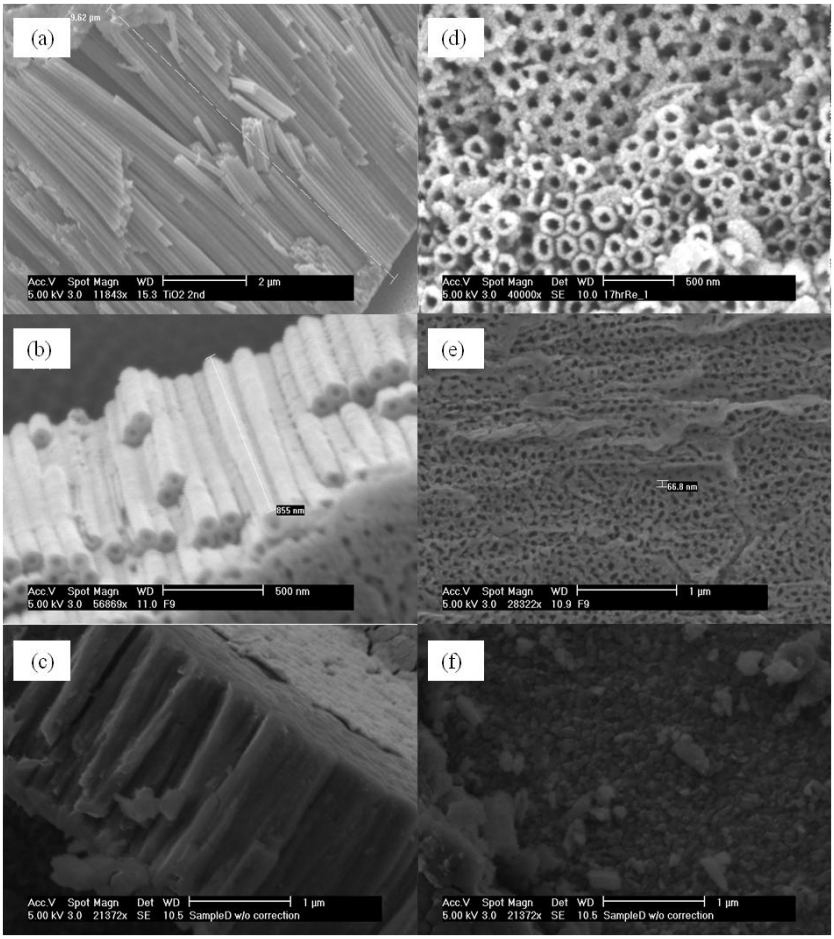

Figure 4-6: Side view (a-c) and top view (d-f) SEM pictures of titania after 1h anodization (50V, ramp rate 1V/s) using different NH_4F-containing solvents : (a,d) ethylene glycol, (b,e), glycerol and (c,f) DMSO. The longest tubes are achieved by using EG; the tubes fabricated in the glycerol electrolyte are shorter in length and their tube opening is smaller; Anodization in NH_4F-containing DMSO did not lead to a clear tubular structure formation on Ti foil.

In the course of the anodization experiments with various solvents, it is also observed that the tube morphology is influenced by the water content, the age of the solution and the number of times the same electrolyte solution had already been used for anodization experiments. As NH_4F and ethylene glycol absorb water in a humid environment, an aged electrolyte effectively contains a higher amount of water than intended. It is generally observed that nanotube membranes fabricated using (i) aged electrolyte or (ii) fresh electrolyte with an increased amount of water accelerates the nanotube growth but leads to membranes that tend to detach from the Ti foil and crack into pieces. This is due to the imbalance between field-assisted oxidation and fluoride dissolution. Excess water is helpful in decreasing solution viscosity and thereby supplying fluoride ions to the metal/oxide interface more efficiently. At the same time, the enhanced oxygen supply accelerates the oxidation process that induced stress accumulated during the fast anodization is not able to be released. As a result, the nanotube arrays are usually detached under this circumstance.

Moreover, we found that problems such as detachment of nanotube membrane can be relieved by repeatedly using the same anodization electrolyte. Intuitively, it may be assumed that previous anodization have consumed some of the dissolved water by a process of $TiO_2 + 6F^- + 2H_2O \leftrightarrow [TiF_6]^{2-} + 4OH^-$ (for the first cycle until an equilibrium concentration of $[TiF_6]^{2-}$ is reached) and $Ti + 2H_2O \rightarrow TiO_2 + H_2\uparrow$ (for each cycle). Therefore, the repeatedly used electrolyte contains less water and more $[TiF_6]^{2-}$ which respectively slow down the oxidation and dissolution processes (Note, however, that the electrolyte will also absorb moisture, if exposed to a humid atmosphere over extended periods). It is observed that the nanotube membrane is

more closely attached to Ti foil without crack formation, and SEM micrographs show that the tubes are better organized and oriented when the samples are anodized using a previously used electrolyte. As exemplified in Fig. 4-7, the JV curve of a dye-sensitized solar cell based on a nanotube membrane prepared by 2nd time use of the anodization electrolyte shows a higher J_{sc} at the expense of a slightly lower V_{oc} and hence a typically ca. 25% higher efficiency. For the samples shown in Fig. 4-7, the anodization is conducted at 50V for 3 h with a 1 V/s initial ramp rate. The nanotubes in a typical nanotube array fabricated under these conditions using the fresh electrolyte (cf. Fig. 4-7a, Fig. 4-6a) are 10 μm long, and have an inner (outer) diameter of 80 nm (140 nm), while the nanotubes grown by repeated use of the electrolyte (see Fig. 4-7) are longer (15 μm), and the tube openings are also wider (inner diameter 110 nm, outer diameter 170 nm). The nanotube arrays resulting from anodization in a repeatedly used electrolyte possess a higher aspect ratio of 8.82 than that of 7.14 produced by the fresh electrolyte. Moreover, these nanotubes are well-organized without severe accumulation of collapsed tubes (debris) from the top view of SEM pictures in Fig. 4-7c even without further treatment such as ultrasonication.

In order to verify the hypothesis proposed above, several experiments are designed and executed to study the effects of water deficiency or the variation in the TiF_6^{2-} concentration on the tube morphology, leading to a better understanding why repeatedly used electrolyte leads to a higher performance in the DSCs.

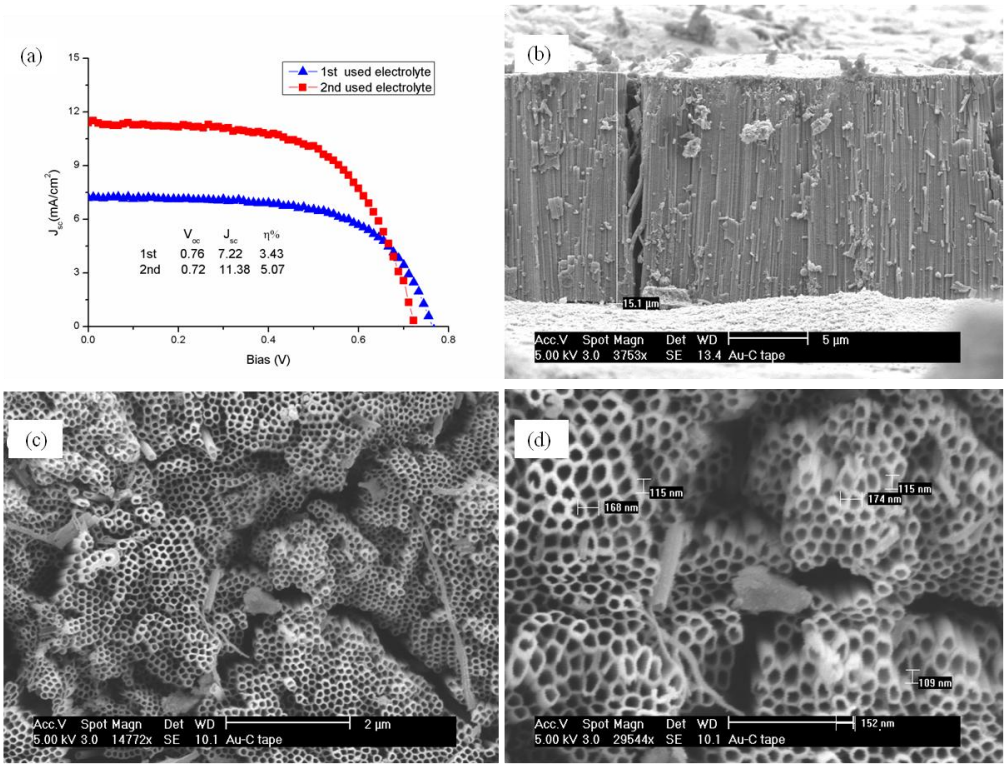

Figure 4-7: (a) Typical JV curves obtained under STC using titania nanotube as photoelectrode prepared by the same anodization profile. The repeatedly used electrolyte is more helpful in fabricating high performance nanotube used in DSC; Side view (b) and top view (c) of the nanotube anodized by 2nd used electrolyte, the tube is longer and tube opening at the top is larger, thereby effective dye adsorption area is larger. A magnified picture of (c) is given in (d).

As a simple way to emulate the effect of a second use of the electrolyte on the TiF_6^{2-} concentration, 0.4 mg of anatase is added to 50 ml of the electrolyte and allowed to react over night. This would correspond to the result of a typical first anodization experiment if we assume that roughly equal factions of the oxidised Ti is finally dissolved and captured in the Ti^{4+} form of the TiO_2 layer. As a consequence of this TiO_2 addition, the current peak in the current vs. anodization time curve is suppressed, while the anodization current in the stationary state increases. Fig. 4-8 illustrates this increase of the current at the final stage as a consequence of the addition of anatase. The blue curve in Fig. 4-8 exhibits higher current ramp and

stabilized current in comparison to the standard electrolyte. Moreover, the anatase addition greatly affects the tube length (+15%) and oxide barrier layer thickness (~30%) given in Fig. 4-9 (b,c), as the concentration of free fluoride is reduced. At the same time the addition of some TiO_2 leads to a more stable $[TiF_6]^{2-}$ concentration and hence less variations in the TiO_2 deposition rate. With this pronounced effect of increasing the tube length and suppressing the oxide film thickness, the modification of the electrolyte composition by the additional anatase optimizes the TiO_2 morphology for application in dye sensitized solar cells. As a consequence of this morphology optimization, the series resistance of the cell would decrease (due to the thinner barrier layer) and the area available for dye absorption is enlarged (by the longer nanotubes). When compared to just reducing the NH_4F concentration to shift the balance between oxidation and dissolution, the addition of the TiO_2 has the additional advantages that (i) the higher overall ion concentration reduces the electrolyte resistance and (ii) the relative changes of the concentrations of active ingredients in the electrolyte over the time of the anodization experiment are reduced.

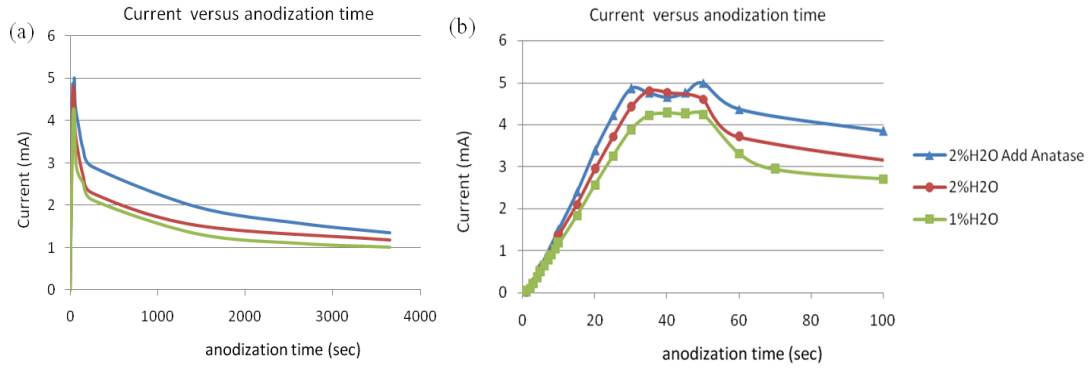

Figure 4-8: Current-time profiles (a) of samples anodized by several electrolytes. A comparison of the blue curve (electrolyte with added anatase) to the reference electrolyte (red curve) clarifies the effect of anatase addition. A comparison of the green curve (electrolyte with reduced water content) to the red reference curve demonstrates the influence of water content. Graph (b) displays a magnified version of the same curves highlighting the variations of the anodization current during the initial period of the anodization.

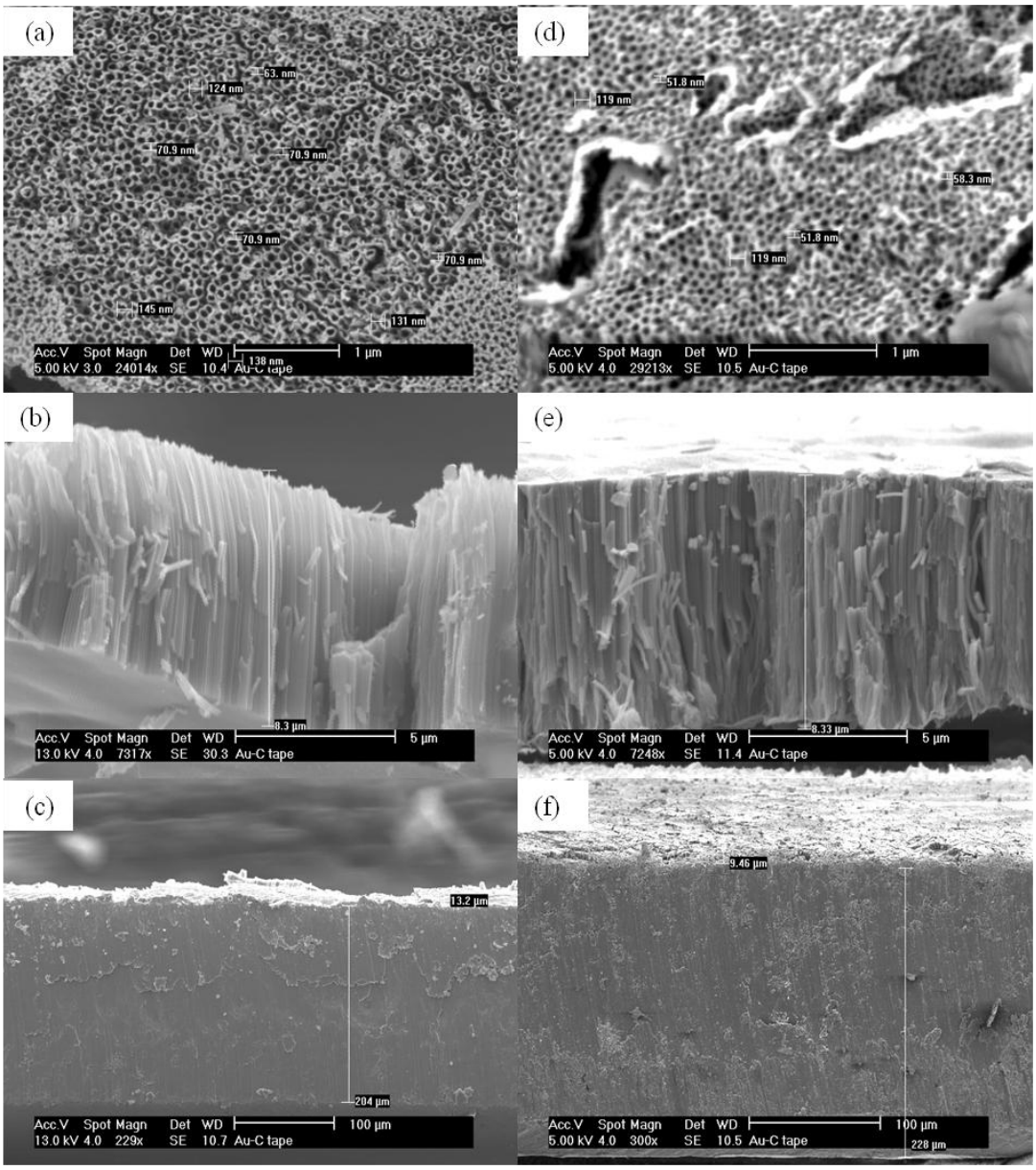

Figure 4-9: Top view (a) exhibits that the inner diameter is 68 nm and outer diameter is 130 nm. The side view section (b) shows that the tube length is around 8 µm and the barrier layer has a thickness of 13 µm (c), the sample is prepared by using electrolyte containing 0.5 wt% NH_4F in ethylene glycol/water (49:1 vol%) solution with 0.4 mg anatase additive; Top view (d) exhibits that the inner diameter is 55 nm and outer diameter is 120 nm. The side view picture (e) shows that the tube length is around 8.4 µm and oxide thickness of 9 µm (f), the sample is prepared by using electrolyte containing 0.5 wt% NH_4F in ethylene glycol/water (99:1 vol%) solution.

On the other hand, the green curve in Fig. 4-8 shows that current density is greatly suppressed when the water content of the electrolyte is tuned down although the reduced water content also increases the nanotube membrane layer thickness (see Fig.

4-9). This may be attributed to a slower diffusion of dissolved charge carriers reducing the growth of oxide film, and larger fluctuations in the fluoride concentration (due to higher viscosity and lower diffusion rates) so that the corrosion rate of oxide film will be reduced as the Fluoride concentration at the surface is more easily depleted. So the decrease of the inner diameter, and barrier layer thickness as well as the increase in tube length can be consistently attributed to the slower migration rates.

In a short summary, the combined effects of anatase addition and reduced water content on the tube morphology are in accordance with the findings when re-using the anodization electrolyte. So we can conclude that it can now be understood why re-using the anodization electrolyte (with reduced water content and higher TiF_6^{2-} concentration) is beneficial for fabricating high aspect-ratio nanotube structures suitable for high performance DSCs.

4.3 Study of the optimized tube length

The diameter of titania nanotubes is usually proportional to the magnitude of the applied potential, but not sensitive to the duration of the anodization while maintaining the same anodization working potential. In the experiments discussed in this section, a Ti foil is anodized at the same working potential using the same electrolyte, so that we gain more insight into the effect of anodization duration on the nanotube morphology, electrochemical properties and their performance in DSCs.

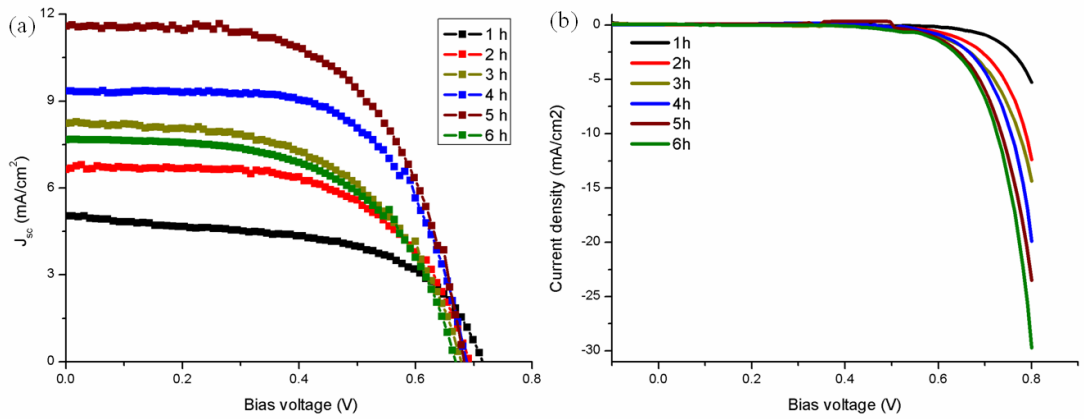

Figure 4-10: Nanotube prepared by anodization for 1-6 h as photoelectrode in DSC application. (a) Photovoltaic performances under STC; (b) dark current.

Since Grätzel and O'Regan [11] introduced mesoporous TiO_2 as photoelectrode in DSCs, the efficiency of such cells using dye sensitizer as photoelectron generator greatly improved due to a larger effective light absorption area for dye molecules. Frank et al. [12] studied the thickness effect of nanoparticle TiO_2 on J-V performance under illumination and in the dark as well impedance in dark. They conclude that the optimized thickness of a TiO_2 nanoparticle layer is around 10 μm as the gain in larger effective dye adsorption area (thereby higher photocurrent) cannot compensate the power loss due to increasing dark exchange current although the impedance study shows that the charge collection efficiency is still close to unity. In agreement with their results, the length effect of nanotube as photoelectrode on the performances of DSCs is similar to that of nanoparticular-based cells, yet with a larger optimum tube length of 20 μm (4 h sample in Fig. 4-10a). The dark current keeps increasing for the samples anodized at a longer time in Fig. 4-10b. Above 20 μm, the effective dye-loading area and the photo-to-electric conversion efficiency start to decrease at listed in Table 4-2.

Table 4-2: The relationship between the anodization duration and the tube length of back-illuminated nanotube-based dye-sensitized solar cell and their corresponding JV photovoltaic parameters under 1 sun illumination. The active area of the cells is consistently 0.384 cm^2.

Anodization Duration (h)	Length (μm)	V_{oc} (V)	J_{sc} (mA/cm^2)	FF (%)	η (%)
1	5 (±0.5)	0.71	5.01	54 (3)	1.9
2	9 (±1)	0.7	6.63	59 (1)	2.73
3	13 (±0.3)	0.69	8.23	55 (2)	3.12
4	16 (±0.4)	0.68	9.34	63 (2)	4
5	20 (±0.5)	0.68	11.5	59 (2)	4.61
6	24 (±1)	0.67	7.6	57 (1)	2.9

Equations 4.1 and 4.2 express the output power of the solar cell, *P(V),* consists of the contributions in the dark and in the light.

$$P(V) = -J_{00}Vd\left[\exp\left(\frac{meV}{k_BT}\right) - 1\right] + e\Phi T_{TCO}V[1 - \exp(-\alpha d)] \quad (4.1)$$

$$\frac{\partial P(V)}{\partial d} = -J_{00}V\left[\exp\left(\frac{meV}{k_BT}\right) - 1\right] + \alpha e\Phi T_{TCO}V\exp(-\alpha d)] = 0 \quad (4.2)$$

Here, J_{00} is the dark exchange current density per unit film thickness, Φ is the incident photon flux, T_{TCO} is the effective transmittance of the TCO substrate; α is the effective absorption coefficient of the cell and d is the thickness of nanotube arrays. The first term on the RHS of equation 4.1 represents the dark current which scales linearly with film thickness, while light absorption of the cells increases exponentially when the film is relatively thin. For instance, increasing tube length from 2 μm via 10 μm to 20 μm enhances the light absorption from 32%, via 86% to 98%, if we assume

α = 5 μm^{-1}. Further increase of the film thickness (>20 μm) is not beneficial for better light harvesting as light cannot reach this part of the cell. In contrast, the first term on the RHS of equation 4.2 contributes to the loss of energy through recombination process as which scales up with respect to the increased tube length. So there would be an optimized length d_{max} for maximized output power.

$$d_{max} = -\frac{1}{\alpha}\ln\left(\frac{J_{00}}{\alpha e \Phi T_{TCO}}\right) - \frac{1}{\alpha}\ln\left[\exp\left(\frac{meV}{kT}\right) - 1\right] \quad (4.3)$$

The optimized length is dependent on absorption coefficient (tube architecture), incident photo flux, diode ideality factor, dark exchange current density and transmittance of the TCO substrate. Comparing nanotubes to nanoparticles, a higher light absorption coefficient and hence a smaller value of d_{max} is to be expected for the latter as light scatters forward along tube length direction.

Other than the balance between light absorption and recombination, a limiting factor for the optimum tube length is also the nonlinear variation of the effective dye-adsorption area with the tube length. This may be partly due to the fact that the inner walls of the nanotubes are V-shaped (cf. Fig. 2-6 in section 2.1.3) and the total surface area varies sub-linearly with the nanotube length. Another contributing hypothesis is that the dye solution incompletely wet the inner wall surface of deep nanotubes, so that the dye-coated area no longer increases (and recombination is promoted at the uncoated TiO_2 surface). Complementary information on the active dye-coated area is extracted from the UV-Vis spectra of desorbed dye in 0.1 mM NaOH aqueous solution. If the nanotube structure is consistent over the range of lengths prepared by the different anodization durations in this study and limitations of dye penetration are not taken into account, the observed variation of the UV

absorption of desorbed dye solution with nanotube length (cf. Fig. 4-11a) would be hard to explain: When the anodization time is increased beyond 5 h, the concentration of desorbed dye (as a measure of the effective dye-adsorption area, Fig 4-11 a) as well as the IPCE of back-illuminated DSCs based on these nanotube arrays (Fig. 4-11 b) even show a pronounced decrease.

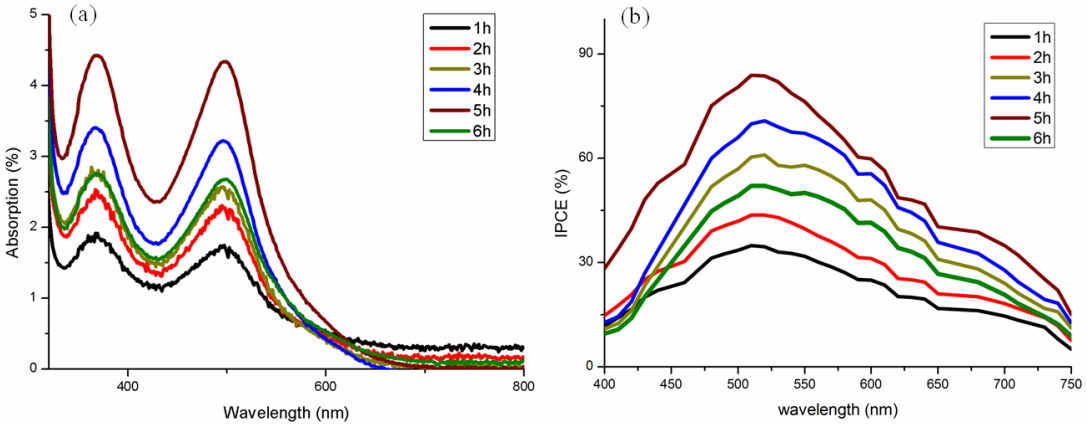

Figure 4-11: Nanotube length effect on UV-Vis spectrum of the desorbed dye solution in 0.1 mM NaOH (a); and on IPCE of back illuminated nanotube-based DSCs (b).

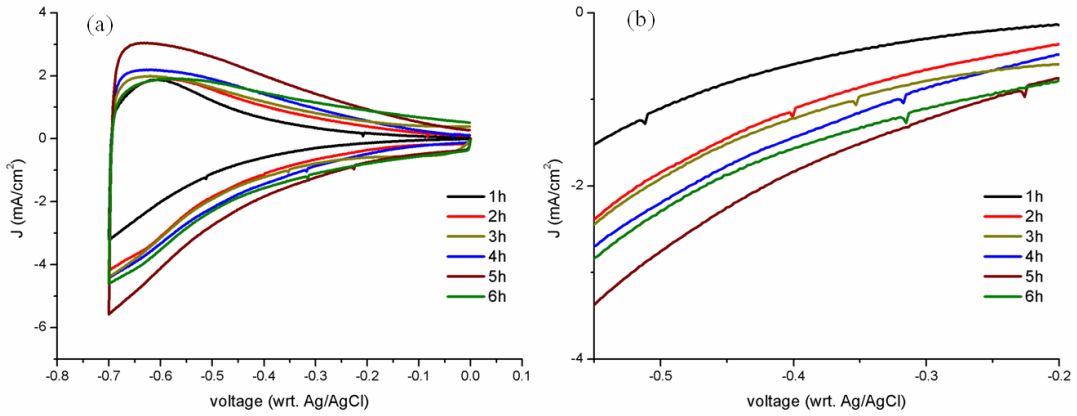

Figure 4-12: Cyclic voltammetry plot of nanotube arrays anodized at 1-6 h. A constant active area (0.5 x 0.5 cm^2) is ensured by covering the excess area of the nanotubes with a mask made of a nonconductive tape. The scan rate is 200mV/s in a 3M KCl aqueous solution. The plot reveals the density of states of nanotube arrays on Ti foil, there is a shift of local trap states on electron energy scale in (a); The magnified plot of a is in (b)

The dye-unloaded TiO_2 nanotube arrays are studied by cyclic voltammetry in a 3 M KCl aqueous solution, a pH value of 2 is adjusted by HCl. The experiment is conducted in a three electrode system with a Pt foil as counter electrode and Ag/AgCl as reference electrode. In a typical CV curve of TiO_2 electrode in 3M KCl aqueous system, a low capacitance which is attributed to FTO/electrolyte interface can be observed at very low cathodic potential. At higher cathodic potentials, there occurs a faradic loss of charge through the film that is accounted for a faradic resistance placed in parallel with the capacitor. There are intrinsic capacitor and trap state capacitor contributing to overall capacitor given that Helmholz capacitor is usually far larger than these two. $1/C= 1/(C_{int}+C_{trap})+1/C_{helm}$

Effectively，$I = dQ/dt = CdV/dt = Cs$, where $s = dV/dt$ is the scan speed. At a scan speed of 200 mV/s, capacitor current prevails therefore the shape of current reflects the magnitude of capacitor which is a sum of intrinsic capacitor (exponential increase of background cathodic current) and trap state capacitor (current spike). The magnitude of the current density in cyclic voltammetry (see Fig. 4-12 in higher cathodic region) reflects the capacitance of each sample and hence the effective surface states. A shift in local trap states from more negative to positive potential indicates that the location of trap states shifts to deeper values with respect to the conduction band of the nanotube arrays when anodization increases from 1 h to 5 h, while the trap state position on the electronic energy scale, as well as the magnitude of current density, shift backwards when anodization duration extends to 6 h. This again implies that the effective surface area is reduced when anodization is extended

to 6 h. The detailed origin of the shift in the local trap states with respect to the anodization period is not clear at this stage.

The grazing angle XRD patterns of this group of samples in Fig. 4-13 show that there is an enhancement in the intensity of a Bragg peak due to the contribution of TiO_{2-x} when anodization period extends from 1 h to 6 h. Charge imbalance of oxygen deficiency is compensated by reduction of Ti^{4+} to Ti^{3+}. In the case of TiO_2 nanotubes created by anodization, the Ti'_{Ti} and $V_O^{\cdot\cdot}$ defects will be enriched near the surface of the nanotube. Although the tubular structure is continuously formed, the growth of nanotube at the later stage of the anodization during 6 h is hampered by a lack of sufficient oxygen supply (leading to an increasing amount of TiO_{2-x} rather than TiO_2). The TiO_{2-x} peak in Fig. 4-13 is identified to be Magneli phases of Ti_8O_{15} with pronounced (00l) preferred orientation and anisotropic strain broadening (in b-c plane) by Rietveld refinement.

In line with the limited access of OH^- there will also be a reduced access of F^- ions to the metal/oxide interface at a later stage of the anodization, which will lead to a more pronounced V-shape of the inner tube wall reducing the available surface area.

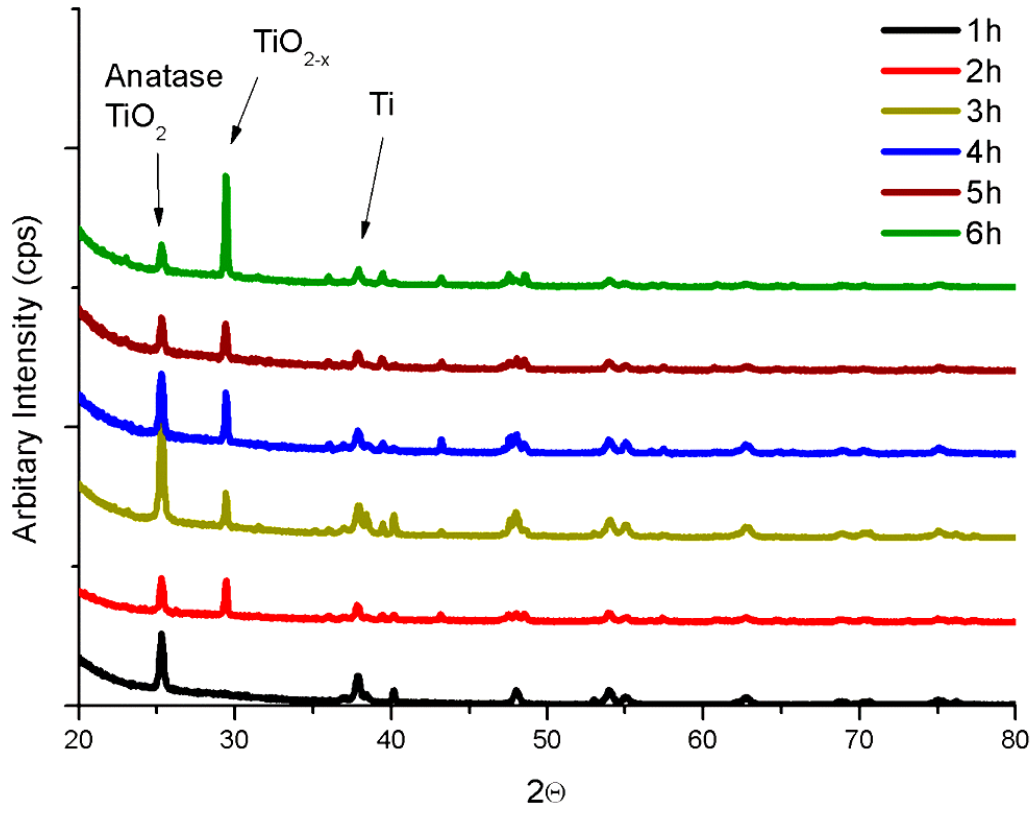

Figure 4-13: XRD patterns of the nanotube arrays on Ti anodized at 1-6 h. The peak attributed to the presence of TiO_{2-x} becomes pronounced over anatase peak as anodization duration becomes longer.

On the other hand, the formation of TiO_{2-x} is beneficial for the fast charge transport of electrons in TiO_2 nanotubes. As discussed above, the recombination rate (charge transfer rate) scales linearly with the length of the nanotube (more precisely with the effective surface area); this trend can be confirmed from the inverse trend of the recombination resistance in Fig. 4-14a (except for the 6 h sample). This result further supports the interpretation of the previous dye desorption experiment that the effective surface area of the sample anodized at 6 h becomes smaller. The charge transport resistance (Fig. 4-14b) also decreases with respect to anodization period. If the electronic properties of the nanotube per length would remain the same, the

charge transport resistance should increase with the length. The opposite trend of a reduced charge transport resistance with increased nanotube length.

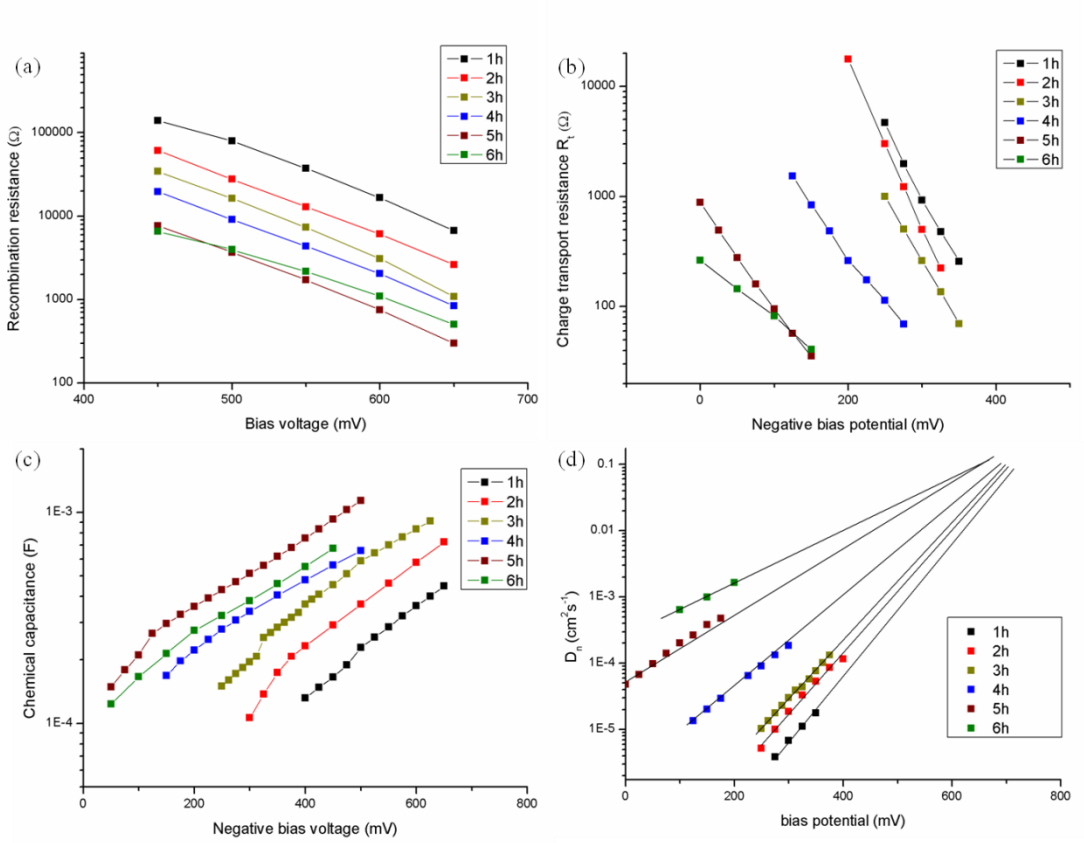

Figure 4-14: The nanotube-based DSCs are characterized by impedance spectroscopy in study. The results are fitted by Zview with respect to bias potential in dark. Recombination resistance (a), charge transport resistance (b) and chemical capacitance (c) of the TiO_2 anodized at 1-6h is dependent on the bias potential in dark. Open circuit voltage decay curves of same batch of samples are shown in (d).

In line with the XRD results the impedance data points towards a higher percentage of the oxygen vacancies in the nanotube prepared by a longer anodization time, so that the charge transport activation energy of the electrons in the titania nanotube drops. With heavy doping, the energy of the highest-energy occupied trap states comes closer to the conduction band of the titania nanotube. This phenomenon is in accordance with the multiple-trapping model of the electron transport in TiO_2. Although there is a sign of a shift of localized trap states towards the deep level

compared to conduction band, the linchpin of fast charge transport is a change of the distribution of density of states. It is generally accepted that traps cannot retard the charge transport rate, and electron movement between the traps is diffusional as well. So when the trap distribution becomes less steep, there are actually more trap states per energy level close to the conduction band which assists in electron transport.

As given in equations 2.22 and 2.23, charge transport resistance should follow an exponential relationship with the applied potential with ideality factor of 1. Chemical capacitance and recombination resistance are, however, dependent on the trap distribution, the ideality factor of which usually deviates from 1. Table 4-3 summarized the respective nonideality factor (α, β, m) obtained by several methods to study the nonideality effect of nanotube/electrolyte interface. When anodization is extended from 1 h to 6 h, the charge transport resistance becomes smaller and smaller, and the slope $dlnV / dR_{ct}$ starts to deviate from 25.8 mV/decade. This is an indication that the electrons are trapped by a distribution of trap states below the conduction band. Therefore, the dependence of electron transport rate of applied potential does not simply follow equation 2.23. In the nanotubes prepared by long-time anodization the defect concentration will be higher and hence the more trapping and detrapping processes will take place. If the trap states are sufficiently concentrated, the electron transport process may eventually take place directly through trap states like hopping processes among traps.

Table 4-3: Fitted results of chemical capacitance, charge transport resistance and charge transfer resistance dependence on applied potential. The values given in table are the ideality factors of the chemical capacitance, charge transfer resistance and dark current vs. applied potential. Ideal diode value is 25.8 mV/decade when ideality factor equals to 1.

Ideality factor	Equation	1h	2h	3h	4h	5h	6h
α: from EIS	2.22	0.09	0.09	0.07	0.08	0.09	0.08
α: from CV		0.15	0.12	0.09	0.13	0.09	0.12
β: from EIS	4.4	0.37	0.41	0.38	0.39	0.37	0.44
m: from dark IV	4.1	0.46	0.4	0.34	0.39	0.35	0.38

The results of chemical capacitance fitting in Fig.4-14c are in accordance with the trend observed in cyclic voltammetry. Values obtained by two methods are considered as comparable indicating fitting results are reliable. The factor α in equation 2.22 is calculated to be 0.09 by impedance fitting, 0.15 by cyclic voltammetry fitting for 1h sample. The slight deviation between the two methods may be due to a small contribution by the capacitance from Helmholtz layer and adsorbed ions on TiO_2 surface.

$$R_{ct} = A\exp\left[\frac{-e\beta V}{k_B T}\right] \tag{4.4}$$

The charge transfer resistance vs. applied potential curve displayed in Fig. 4-14a shows that the slope coefficient β is about 0.4. The more this value deviates from 1, the more of the electrons transfer from a shallower distribution of trap states toward the electrolyte rather than from the conduction band. The fit results obtained from impedance spectroscopy and dark current are again comparable. Generally speaking, the larger value of β is, the higher the fill factor will be. This explains the consistently smaller fill factor in nanotube-based DSCs compared to nanoparticle-

based DSCs. Moreover, the higher the recombination resistance, the higher the open-circuit voltage is. A typical value of recombination resistance at a bias potential of 600mV in nanoparticle-based cell is around 50 kΩ, while the highest value in nanotube-based cell (1 h case) is 5 kΩ. The best solution to further optimize nanotube-based DSCs would be to suppress the recombination process. (In order to increase V_{oc} and ff, as these two parameters are still lower than the corresponding typical values in well-optimized nanoparticle-based cells).

D_n is the chemical diffusion coefficient and D_0 is the diffusion coefficient at the transport level in equation 4.5.

$$D_n = \frac{N_c T_0}{N_L T} \exp\left[(E_{Fn} - E_c)\left(\frac{1}{k_B T} - \frac{1}{k_B T_0}\right)\right] D_0 \qquad (4.5)$$

The chemical diffusion coefficient is delayed by the response of the trapping and detrapping process. D_0 can be determined by extrapolating the D_n vs. applied potential curve to the conduction band. In Fig. 4-14d, we observe that the intercept places an upper constraint on the free electron diffusion coefficient $D_0 = 0.1$ cm^2s^{-1}; this is an indication of a very fast charge transport rate in nanotubular structure (compared to the highest reported value of 0.01 cm^2s^{-1} in nanoparticle system).

Open-circuit voltage decay curves provide an indication of the electron life time. The trend observed in the open-circuit voltage decay curves shown in Fig. 4-15b is in accordance with the calculated electron life time from dark impedance results in Fig. 4-15a. The highest electron life time (ca. 1 s at 650 mV) is observed for the sample anodized for 4h, which leads to a cell conversion efficiency of 6% under STC.

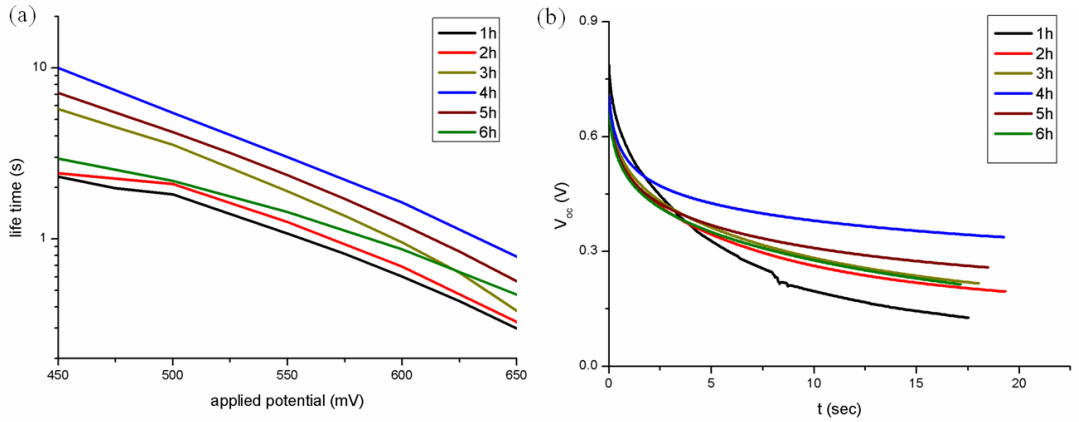

Figure 4-15: Electron life calculated from fitting results of impedance spectroscopy of the NT-based dye-sensitized solar cells in dark in (a); Open circuit voltage decay curves (another measurement of electron life time) of the same batch of cells showing very similar tendency as tube length.

In summary, the idea of elongating nanotubes so as to gain a larger effective dye-adsorption area is successful as long as the thickness of active layer remains within the effective light absorption length. The gain in light absorption can compensate the power loss due to increased dark current. Nevertheless, nanotube structures require further optimization to enhance effective surface area and facilitate access by dye solution and redox electrolyte. The electron transport process is demonstrated to be extremely fast in nanotube arrays [8] (typically we find that D_n is around 10^{-4} cm^2s^{-1} from V_{oc} till -0.4 V compared to D_n of nanoparticles which drops to 10^{-6} cm^2s^{-1} at - 0.5 V), even though the non-ideality factor of the dark current process at the nanotube/electrolyte interface deviates from unity. The nanotube cell is still showing a good performance probably due to the lower activation energy compensating the long tail distribution of trap states.

4.4 Sputtered Ti on FTO

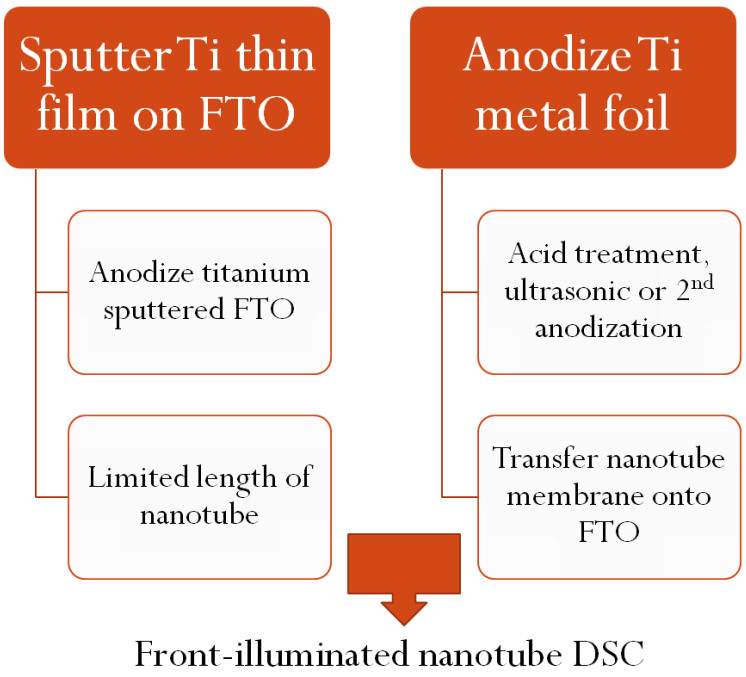

Figure 4-16: Two approaches to fabricate front-illuminated nanotube-based dye-sensitized solar cells: Anodize a Ti-sputtered FTO (left) or anodize Ti foil followed by the detachment and transfer of nanotube membrane onto FTO (right).

In my previous publication [8], we have demonstrated that nanotube titania is advantageous when compared to nanoparticular titania as photoelectrode in terms of electron transport. Still, the solar cell efficiency of nanotube-based DSCs is lower due to the restriction to a back-illumination configuration, when the nanotubes are to be used as grown on transparent Ti foils. To solve this problem, it is desirable to grow the nanotube arrays on a transparent conductive substrate instead of Ti foil. There are fundamentally two types of approaches to fabricate front-illuminated nanotube-based dye-sensitized solar cells as sketched in the Fig. 4-16 above. (i) A titanium thin film is sputtered on a TCO and an anodization process is conducted after that so as to directly grow titania nanotubes on the TCO (e.g. FTO). (ii) Alternatively a nanotube

array is grown on a Ti foil by anodization (as described in the previous sections), but then the nantubes are detached (preferentially as an intact, crack free membrane) from the Ti foil, transferred and fixed onto FTO. In this section, the first approach is explored here (For the second approach see section 4.5).

Quality and thickness of the sputtered film along with stopping the anodization process at the correct point in time are three critical issues in this experiment. The detailed experimental work of the sputtering is illustrated in section 3.2.3. As described in Fig. 4-17, the targeted atoms are knocked out by Ar plasma and fly towards the substrate. A higher RF power, a lower chamber pressure and a larger DC bias accelerate the deposition rate of target atoms on the substrate. A higher working temperature allows for fast atom diffusion on the substrate leading to a more uniform islands forming at the initial stage of the deposition. This should be helpful in depositing a high quality thin film.

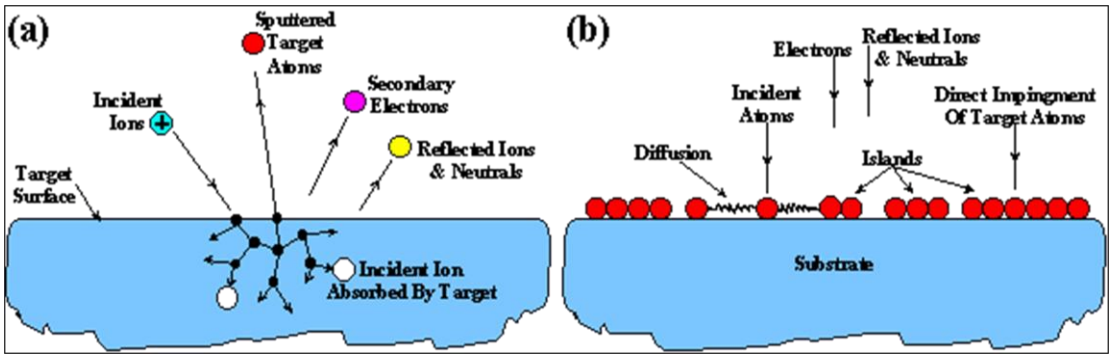

Figure 4-17: Schematic diagram of plasma bombarding on target (a); Atoms from the target hit the substrate and form small islands. The uniformity of the islands (film) depends on working temperature and deposition rate (controlled, e.g., by pressure, bias potential) in (b).

However, it turned out that the quality of the sputtered Ti thin film at high temperature is not superior to the quality of films sputtered at room temperature (see Fig. 4-18). The Ti morphology sputtered at room temperature in SEM picture in Fig.

4-18a is more uniform. Although we can still observe the topography of isolated unit like shape due to the island formation at the initial stage of the deposition, the sample after anodization shows a nanorod like structure in Fig. 4-18c.

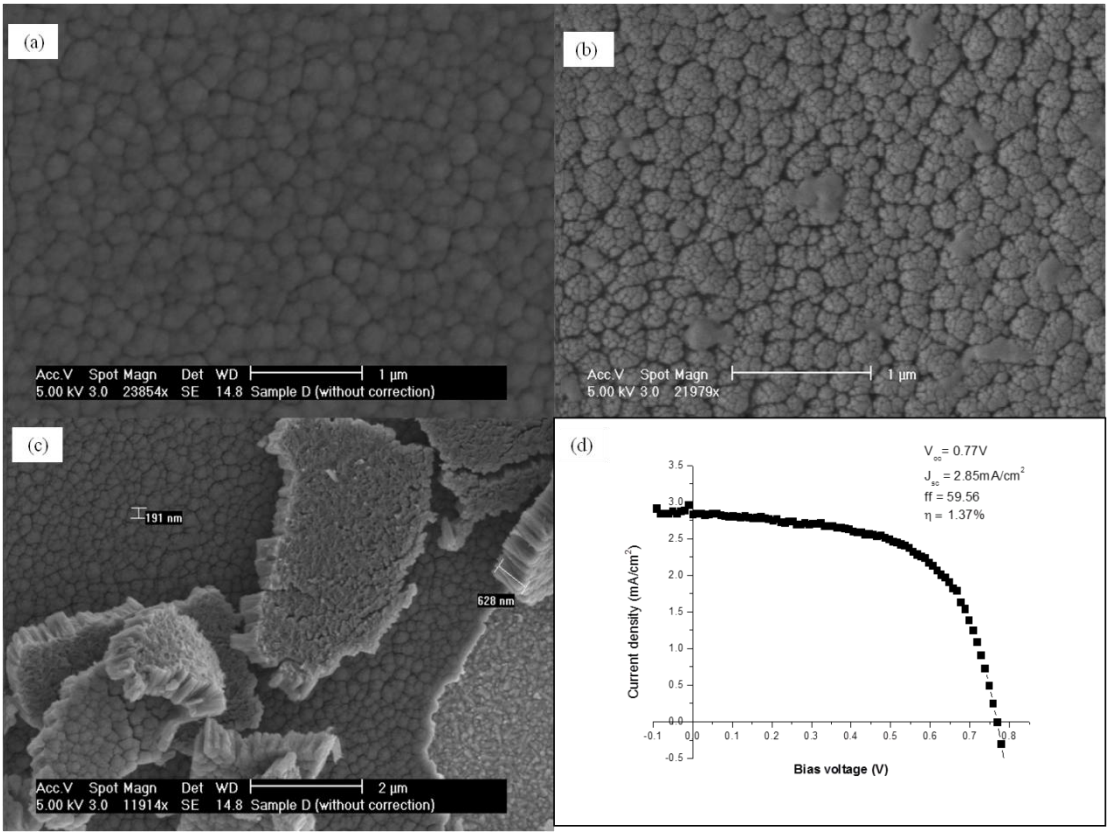

Figure 4-18: Top surface of a Ti film deposited by RF sputtering at room temperature (a) and at 400 ℃ (b); Cracked TiO_2 nanorods layer on FTO produced by anodization of a room temperature-sputtered Ti film, indicating the nanorods are 190 nm wide and 630 nm long (c); The JV curve of the sample shown in (c) under STC (d).

The film morphology grown at a higher working temperature (~400 ℃) is given in Fig. 4-18b. The top surface looks more porous than the one prepared at room temperature. Surprisingly, the high-temperature deposited film is not conductive, and the XRD pattern shows the presence of anatase. Despite attempts to eliminate a possible leakage or problems with a specific target, the production of a pure Ti film by high temperature-sputtering is not successful with the available sputter system.

Because of these limitations the pioneering work of using high-temperature sputtering to fabricate front-illuminated nanotube-base dye-sensitized solar cells is not pursued further.

Anodization of the Ti films produced by room temperature sputtering led to a TiO_2 film with a low-aspect ratio (~3) nanorod structure (see Fig. 4-18c). The annealed TiO_2 on FTO electrode is then soaked in 0.3 M dye solution (N719 in ethanol) over night (for details see chapter 3). Cells are fabricated by sandwiching the anodized TiO_2 on FTO photoelectrode and a Pt-coated FTO counter-electrode. The highest cell efficiency reached with these sputtered photoelectrodes is 1.37% as seen in Fig. 4-18d. This cell efficiency is considered low mainly due to the formation of solid nanorods instead of hollow nanotubes after anodization, which reduces the effective dye-absorption area. The nanorod layer is also only 630 nm thick, which also reduce the surface area. The finding that the length of the nanorods is shorter than the thickness of the originally deposited Ti film suggests that the less tightly packed Ti film on FTO partly peeled off during anodization.

In a brief summary, it is demonstrated that the method of using sputtered Ti on FTO works in principle. Sputtering at high temperature should lead to a more uniform, high quality film more suitable for later anodization. However, the optimization working temperature, working pressure, RF power and the distance between sample and target requires further works. One further limitation of this approach for DSC application is the achievable thickness of the film. It may be suitable for solid-state nanotube-base dye-sensitized heterojunction cell only, as the maximum deposited film thickness reported so far is 3 μm. In other words, if the Ti is

completely converted into titania nanotube during anodization, the oxide tube length cannot exceed 10 µm. Light harvesting of nanotube arrays at a length of 10 µm in DSC is not sufficient yet.

4.5 Nanotube detachment and transfer

As discussed in the previous section, using nanotube arrays as grown on Ti limits the flexibility in the design of photoelectrochemical devices: illumination is only possible from the opposite side of the cell ("back-illumination"), limiting overall performance by light absorption in the hole-conductor [13] as well as reflection at the counter-electrode. To avoid these losses, various methods have been tried to grow nanotube layers directly on a transparent conducting substrate (cf. section 4.4) [14] or to transfer nanotube layers grown on Ti onto a TCO [15,16]. The aggressive transfer methods tried so far (acid etching, ultrasonication) yielded fractured and or damaged nanotube arrays and a thick nanoparticle buffer layer (formed from the Ti isopropoxide) may cast doubt on the contribution of the nanotube layer for the overall cell performance. Effectively, subsequent studies found that a large fraction of the overall efficiency is contributed by the nanoparticle layer. [17,18] A method to fabricate large-scale, crack-free nanotube membrane layers with adjustable thickness is not yet been available, when we started our project based on our observation that a second anodization of a pre-annealed anodized Ti foil results in detachment of the nanotube membrane. Similar findings were in the meanwhile reported in the literature by Lin *et al.*[19]. However, the detailed mechanism of this process remained unclear

from Lin *et al.*'s work.

The outcome of different detachment methods of membrane used so far to fabricate front-illuminated nanotube-based DSCs in our lab is summarized in Table 4-4. Compared with our results in reproducing the two previously reported methods, we have developed a new two-step anodization method leading to the fabrication of a more efficient DSC with large-scale active area.

Table 4-4: Comparison of front-illuminated nanotube DSC fabricated by different methods in our lab (anodization duration is 4 h for each method).

Method	Reference	η(%) reported for 20μm nanotubes	Experimental observation	η(%) this work
Two-step anodization	This work	N.A.	Large scale, intact membrane obtained, highly repeatable	6.3
Acid treatment	Park et al. [15]	5.8	One out of ten attempts successful, only. HCl immersion time required to cause detachment cannot be predicted reliably. Long time immersion tends to damage the nanotube structure. Method can only be applied to sufficiently thick membranes (> 10μm)→ not suitable for SSDSC	5.6
Ultrasonic Agitation	Lei et al. [16]	8	In contrast to findings by Lei *et al.*, the membrane generally cracks to small pieces in our experiments irrespective of the ultrasonication power. In most of the experiments, even prolonged ultrasonic agitation alone does not lead to membrane detachment from Ti foil.	N.A.

Among the three approaches listed in Table 4-4, ultrasonic agitation turned out to be not reproducible in our lab. There seems to be no way to tune the ultrasonication power in a way that just detaches the membrane without cracking the nanotube

arrays. In contrast, the acid treatment method could be reproduced in the lab yielding results in close agreement with literature reports. Still, the reproducibility of this method is too low for practical application (about 1 out of 10 attempts only leads to a detachment of an intact membrane) and we find that the method works only for arrays of sufficiently long nanotubes (> 10 μm). Thinner titania nanotube membranes cannot be detached by this method, as they tend to dissolve in the acid before a detachment from the Ti foil takes place. The performance of front-illuminated dye-sensitized solar cells made by acid treatment method is illustrated in Fig. 4-19 that shows typical JV curves under illumination of the front-illuminated nanotube-based samples.

As seen from Fig. 4-19 membranes from relatively short anodization time of 2 h yield unsatisfactory performance, while the highest performance is observed for samples anodized for 6 h. A Ti sample anodized for 2 h before concentrated (1 M) HCl acid treatment seems to be the minimum requirement for this method to work. It is observed that the longer the tube, the higher the chance the membrane is detached from Ti foil after an immersion in the concentrated acid for roughly 1 h. On average, the nanotube is shorten by 4~5 μm after 1 h acid treatment among successful trials. When analyzing the performance of these cells, it should be kept in mind that how long the acid treatment needed to achieve the membrane detachment shows very wide fluctuations (with a tendency of a longer time being needed for thinner nanotube membranes). During this acid treatment the nanotube length shrinks by dissolution (Table 4-5) and thereby the surface area available for dye adsorption becomes too small particularly for the samples anodized for less than 6 h. The variation of the acid

treatment time of course also limits the repeatability of the results reported here, as the initiation of the detachment mainly depends on imperfections of the individual membrane. Sometimes, even nanotube arrays prepared by long time anodization could not detach from Ti after acid treatment. The low predictability on the required time of acid treatment makes this method also unattractive for technical applications.

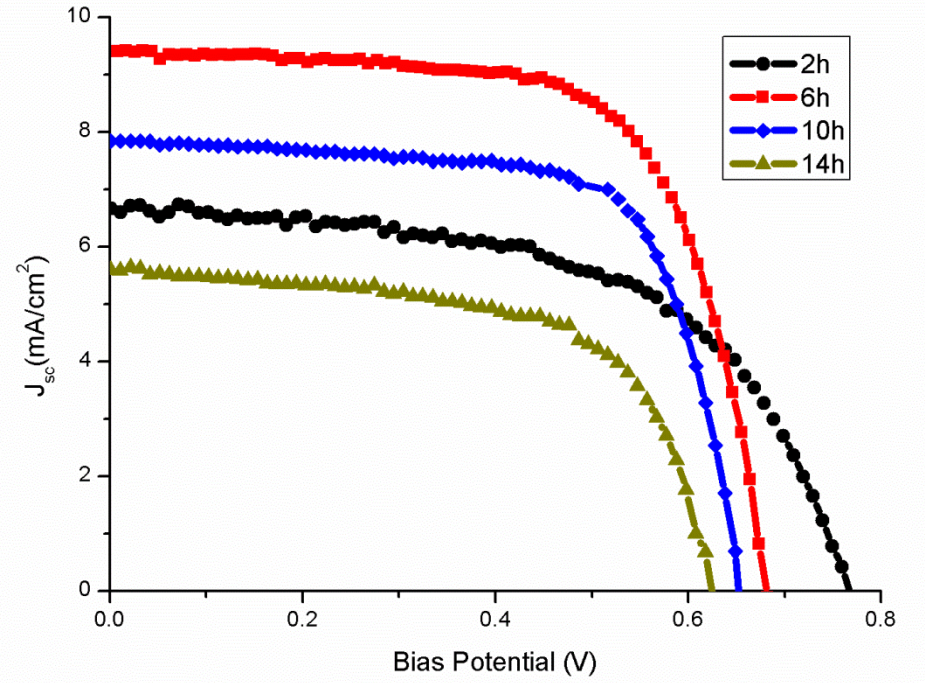

Figure 4-19: JV curves of front-illuminated nanotube-based dye-sensitized solar cells using acid treatment method to detach nanotube from Ti foil. The nanotube is anodized at 50V for 2, 6, 10 and 14h respectively.

For the sufficiently thick nanotube membranes, the variation of the J-V curve with respect to the anodization time for the nanotube preparation roughly follows the trend of backside-illuminated cells discussed in section 4.3. From 6 h onwards, the longer the anodization, the worse the photovoltaic performance. This part of the study further substantiates the observation of how anodization duration affects the cell performance. Nanotubes that are longer than the optimized length lead to decrease of

J_{sc}, ff and V_{oc}. Therefore, the best solution is to find a way to increase the optimized length so as to allow the J_{sc} to reach the theoretical maximum (~20 mA/cm^2) but not to reduce ff and V_{oc}, which is a good topic for future works.

Table 4-5: The photovoltaic performance of the cells made from acid detached nanotube membrane. The method is more repeatable when the anodization duration is sufficiently long. After roughly one hour treatment, the nanotube arrays are generally shortened in a large extent.

Anodization (hours)	Length after treatment (μm)	V_{oc}(V)	J_{sc}(mA/cm^2)	FF(%)	η(%)
2	8	0.76	6.66	57	2.89
6	18	0.68	9.40	67	4.28
10	25	0.65	7.85	71	3.62
14	30	0.62	5.60	62	2.15

A major advantage of our two-step anodization approach when compared to alternative nanotube membrane transfer techniques [15,16] is that by our method we could achieve a complete membrane transfer in more than 90% of the experiments. When using this highly repeatable method, the size of the detached membrane is only limited by the area of the Ti foil that is immersed in the anodization electrolyte (in the experiment 2 × 2 cm^2). It should be straightforward to scale up the method further to a scale of interest for commercial application. Fig. 3-5 (a-g) in section 3.2.3 illustrates the sequence of membrane detachment steps and transfer onto FTO. Titania nanotube arrays are fabricated by anodizing a cleaned Ti foil as indicated in Fig. 3-5 (a, b), the as-prepared sample is annealed to crystallize (see Fig. 3-5c). A second anodization is the key stage for membrane detachment (Fig. 3-5d).

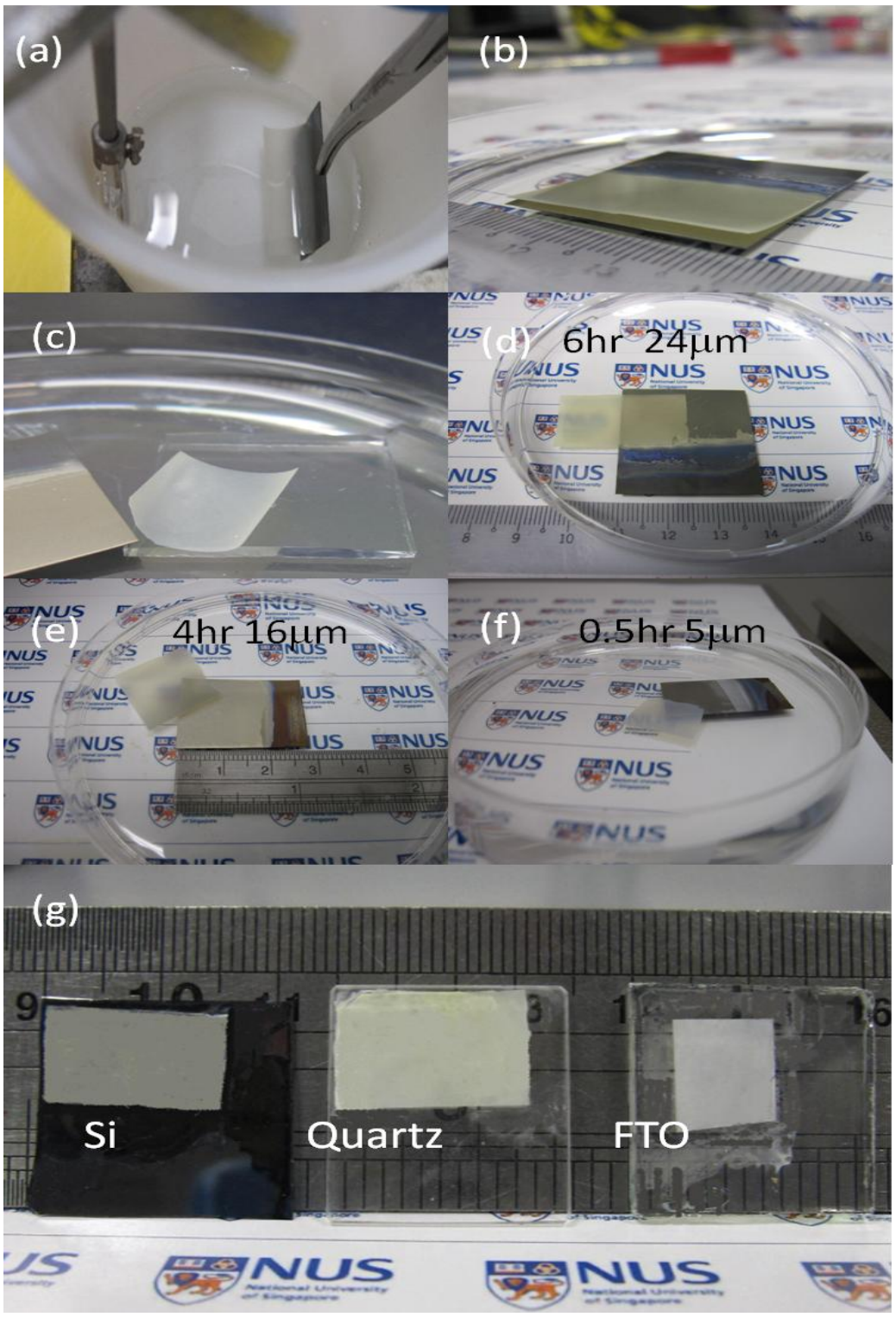

Figure 4-20: (a) Membrane detached from Ti foil; (b) transferred into a IPA-contained Petri dish; (c) free-flowing membrane on FTO (d-f) A glance of how transparency of the membrane changes with thickness; (g) membrane on various substrates after applying adhesive solution and annealing.

There are some critical steps worthy to highlight in Fig. 4-20, which shows photographs representing the equivalent steps that are schematically described in Fig. 3-5 (e-g). The depth of immersion is chosen so that at the end of the second anodization in Fig. 4-20a, the membrane peels off except for a thin rim close to the electrolyte: air interface (see Fig. 4-20b) that remains attached and facilitates transfer of the membrane into an IPA-containing Petri dish without mechanical damage. The membrane can then be cut along this rim to fully detach the membrane. The membrane-receiving substrate (FTO with spin-coated TiO_2 layer) is also immersed into the same IPA-contained Petri dish (Fig. 4-20c). By just tilting the metal foil, the titania nanotube membrane gently slides down onto the FTO. Membrane transfer is conducted in IPA rather than in air to minimize surface tension. This procedure also avoids mechanical damage of the membrane (e.g. by tweezers).

The thickness of the membrane and hence its transparency is controlled by the duration of the first anodization (from 5 μm for 0.5 h to 24 μm for 6 h, see Fig. 4-20 (d-f)). The membrane-FTO stack is then removed from IPA and two drops of the above-mentioned isopropoxide IPA solution are applied to the side of the membrane. Infiltration of the solution between anatase buffer layer and nanotube membrane fixes the membrane on FTO. The attached nanotube layer is subsequently heated to 200 ℃ for 15 min, and finally annealed at 480 ℃ for 30 min. This leads to a membrane closely attached to a variety of substrates such as Quartz, Si and FTO (Fig. 4-20g). This again demonstrates a great flexibility of the transfer method that can be extended to other applications. The transferred nanotube membrane consists entirely of

crystalline anatase as confirmed by XRD in Fig. 4-21a. On the other end, there is only amorphous phase on the remaining Ti foil after detachment in Fig. 4-21b.

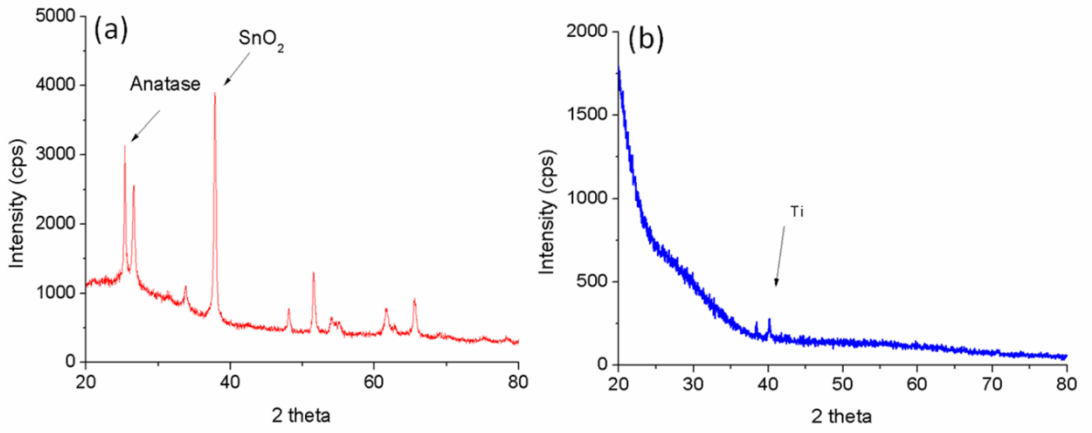

Figure 4-21: XRD patterns of titania nanotube membrane attached onto FTO (a) and of the Ti foil from which the membrane is detached after second anodization (b).

In order to get deeper insight into the detachment mechanism, we studied the current-time profile of the process and analyzed the separation products by SEM micrographs and XRD. The current-time profile of the anodization can typically be divided into three stages [20]: (i) the current initially increases as the potential ramps up; (ii) once the anodization potential is reached, the current drops due to the field-assisted formation of an oxide layer; (iii) fluctuations in the current-time curve indicate local peeling-off of the nanotube layer until a stationary state with an only slow decrease in current vs. time is reached. This trend is shown in Fig. 4-22 (a) for samples anodized at 50 V or 70 V for 1 h, where only a circular shaped region of the Ti foil is exposed to the electrolyte. The characteristics of the anodization current curve change when Ti foils are anodized in an electrolyte-containing PTFE beaker, so that also edges and corners of the Ti foil are exposed causing high current fluxes, which contribute to membrane detachment. As a consequence, the two-step anodization works more

reliably in the simple beaker setup than in an anodization kit that exposes only a defined area of the Ti foil.

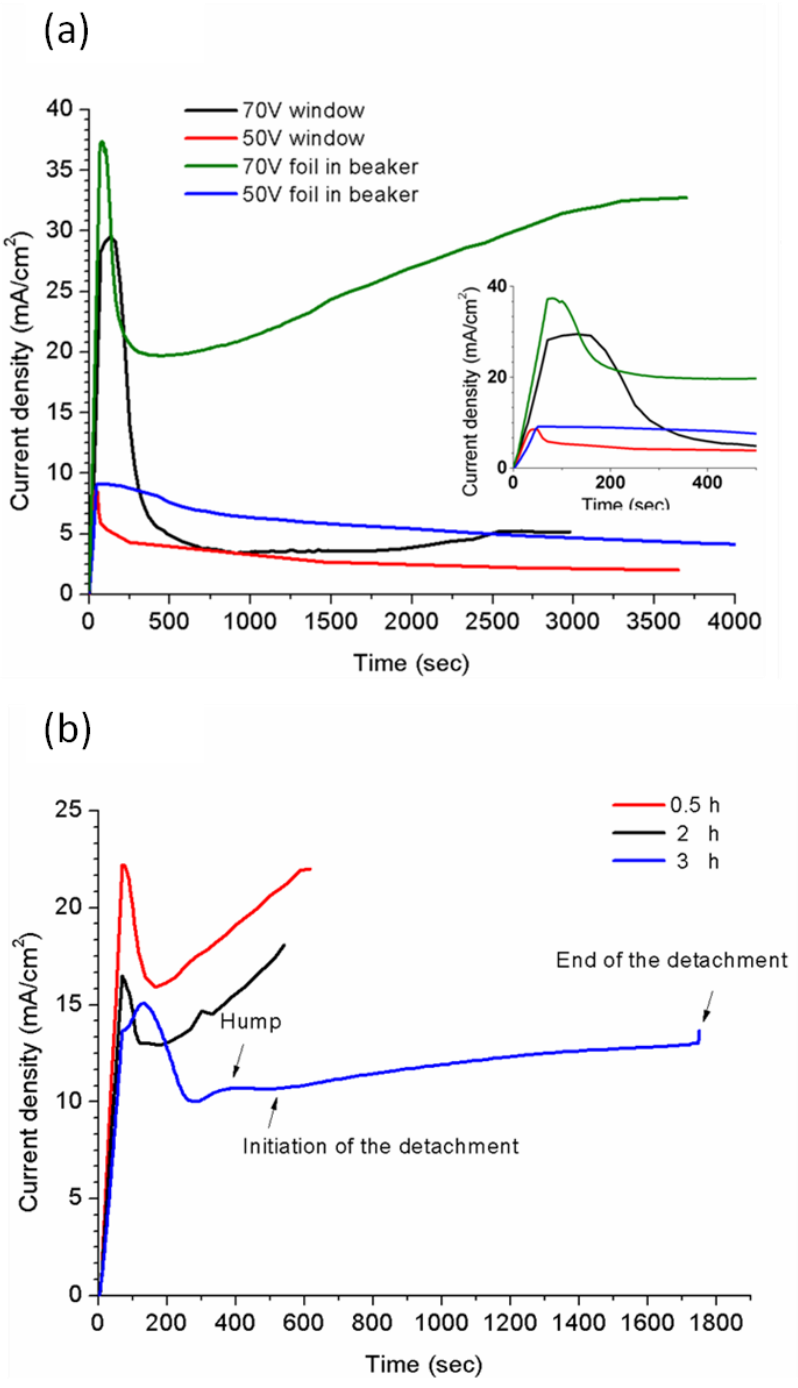

Figure 4-22: (a) Variation of current density vs. time for Ti foils immersed in a PTFE beaker or sandwiched in an anodization kit (circular window of diameter 8 mm exposed). Foils are anodized for 1h at 50 V and 70 V. Inset highlights the first 500 s. (b) Effects of nanotube length on current-time curve during second anodization.

Membrane detachment criteria are tested by varying experimental conditions. We found that annealing temperature, annealing time and anodization potential in the second anodization largely influence the detachment process. Anodization current-time curves for the second anodization are shown in Fig. 4-22b using samples anodized for 0.5 - 3 h in the first anodization. Again, the anodization current exhibits a similar time profile with an overall decrease in current for increasing membrane thickness. Once 70 V is reached, the current initially drops, and then remains nearly constant for a few minutes. In most experiments a minor hump in the current curve marks the start of a current increase and first signs of a gradual detachment can be observed immediately thereafter (cf. blue curve in Fig. 4-22b). Such a hump is commonly ascribed to the initiation of a new tubular oxide layer [20] that might cause the detachment. The current rise after the hump in Fig. 4-22b can be understood as a consequence of fresh Ti foil surface exposed to the electrolyte due to the ongoing detachment.

To analyze the effect of annealing conditions on membrane detachment, we also compared samples that have undergone identical first and second anodization processes, but differ in the annealing in-between. We found no detachment for samples that have not been annealed between the two anodizations or have been annealed only at 200 ℃ for 3 h so that the nanotube membrane remains amorphous. Our findings thereby contrast to a recent report by *Lin et al.* [19], who suggested that drying for 3 h at 200 ℃ leads to the detachment of (open-ended) nanotubes. Moreover, a sample annealed at 480 ℃ for 20 min only (leading to incomplete conversion into anatase) also failed to detach during second anodization. Both

experimental observations can be explained, as the nanotube undergo incomplete phase transition and thereby remain vulnerable to dissolution in the presence of fluoride. Therefore, no second layer of nanotube arrays is formed during second anodization. Instead, the nanotube growth during the second anodization just continues from the bottom of the nanotube arrays fabricated by the first anodization, if there is insufficient heat treatment to ensure a complete phase transition. Therefore, it appears plausible to assume that the detachment is initiated by the strain/stress generated at the interface between two nanotube layers (partially due to geometric mismatch between the two nanotube layers, partially due to weaker interactions at the phase boundary between amorphous and crystalline anatase nanotubes).

Other than the effect of annealing temperature and duration, the effect of various choices of the anodization potential during the second anodization is also examined. If using the optimized heating profile after the first anodization, a second anodization at 50 V for 1 h (i.e. the same voltage as in the first anodization) is applied, this does not leads to a detachment, implying that nanotube fabricated at the same applied potential during the second anodization cannot create a sufficient mismatch between the two tubular structures (Both upper and lower nanotube arrays are similar in tube diameter and inter-tube spacing).

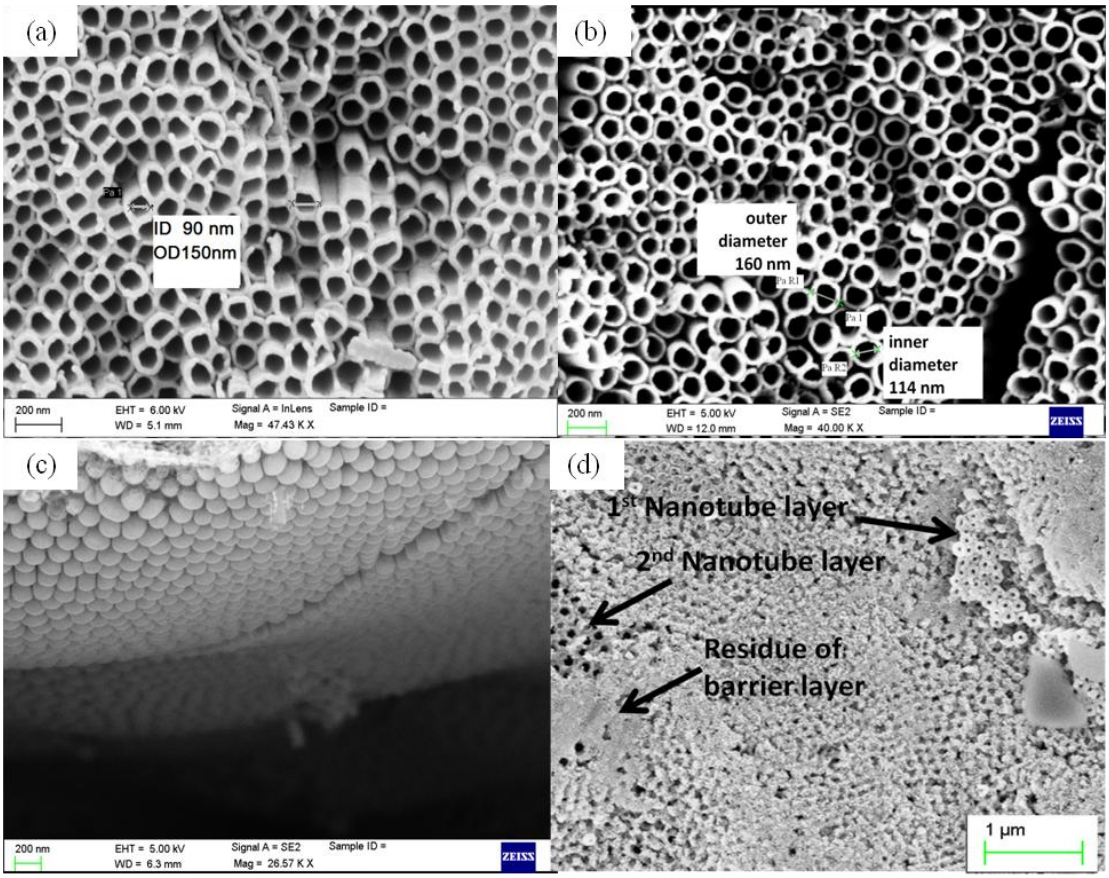

Figure 4-23: Top view of 5 µm nanotube membrane prepared by 0.5 h anodization at 50V after first anodization (a) and attached on FTO (b); (c) bottom view of detached membrane, showing a closed-ended tube bottoms; top view (c) of the remaining Ti foil after twice anodization, there are nanotube remains on Ti foil after membrane detachment.

Recently, another method reported by *Li et al.* to produce free-standing open nanotube membranes was reported, that is employing a sudden rise of the anodization voltage from 60 V to 120-150 V [21]. This method is based on the build-up of pressure by a fast production of oxygen gas within the nanotubes leading to an explosive detachment of the upper part of the nanotube membrane. The authors did not report use of these nanotube membranes in DSCs and limited efforts to reproduce their results are unsuccessful, possibly because of limitations of the available pulse power in our equipment.

SEM studies in Fig. 4-23 present the evolution on nanotube morphology in the course of our two-step anodization and transfer procedure. The morphology of the nanotube membrane slightly changed after transfer as demonstrated in Fig. 4-23 (a, b). The inner diameter increases after detachment indicating there is still a moderate amount of fluoride dissolution process taking place on anatase nanotube during the second anodization. The first anodization as usual produces closed bottom nanotubes. These are preserved in the membrane detachment (as shown in Fig. 4-23c). We further examine by SEM the Ti foil after detachment of the nanotube membrane (Fig. 4-23d). It can be seen that another nanotube layer has grown during the second anodization and this secondary nanotubes are not detached together with the first layer (created during the first anodization). Tube diameter and tube wall thickness of tubes anodized at 50 V during first anodization and at 70 V during second anodization should differ [10]. However, as indicated in Fig. 4-23d, the nanotubes formed during second anodization are of nearly the same diameter as the ones from first anodization. This may be tentatively linked to the inhibited access of F^- and OH^- and thereby of the oxidation and dissolution processes. A thin layer of compact TiO_2 separating the two nanotube layers in Fig. 4-23d might arise from the debris accumulation during formation of the 2^{nd} layer or from the annealed barrier layer. The first hypothesis appears more plausible, as a grazing incidence XRD shows that the oxide layer remaining on Ti after detachment is amorphous (Fig. 4-21).

From all the characterization results discussed above, a possible mechanism to consistently explain all our observations is proposed. The initial anodization leads to a compressive stress on the nanotube layer, which is only partially released during

crystallization. At the beginning of the second anodization, bubbles are formed at the surface of the membrane due to an oxygen formation side reaction on the oxide surface indicating a high electronic conductivity of the oxide layer on Ti in Fig. 3-5d. The attachment between the annealed compact barrier layer and the top of the newly formed nanotube under layer turns out to be the weakest link in the multilayer stack. A stress-assisted etching of this connection finally leads to detachment, which invariably starts from the rim of the electrode. This can be monitored visually, as the detached part of the membrane becomes opaque and the bubble evolution at the top surface ceases once detachment starts. The peeling-off is also assisted by an inhomogeneous stress distribution in the nanotube membrane, as seen from the bending of the detached membrane. Once a gap forms between the two layers at the rim of the electrode, the detachment process may also be assisted by the oxygen bubble evolution in-between the two layers in accordance to the mechanism proposed by Wang and Liu in [22]. Thus we can conclude that the reported two-step anodization procedure reproducibly yields large-scale, crack-free titania nanotube membranes and the annealing process is crucial for a successful detachment.

To demonstrate the applicability of the approach, we produced and characterised a set of front-illuminated dye-sensitized cells based on TiO_2 membranes with a range of thicknesses transferred on FTO (Fig. 4-24). J-V characteristics of the cells under 1 sun illumination are plotted in Fig. 4-24a. The minute efficiency registered for a control sample without a nanotube membrane proves that > 95% of the cell efficiency is from nanotube membranes. It may be noted that this is different in literature reports for nanotubes detached by chemical etching and attached with the

help of a 2 μm TiO_2 nanoparticle paste layer that substantially (30%) contributes to their observed efficiency. [23]

Table 4-6: Parameters obtained from characterization of J-V curve under 1 sun illumination for front-illuminated nanotube-based DSC undergo different anodization duration. Active area is 0.5 cm^2. FIF: front-illuminated cell on FTO; BIT: back-illuminated cell on Ti.

	thickness	V_{oc} (V)	ff(%)	J_{sc} (mA/cm^2)	η(%)
FIF6	24 μm	0.78	60	9.1	4.2
FIF4	16 μm	0.78	63	13.0	6.3
BIT4	16 μm	0.75	60	12.4	5.7
FIF3	13μm	0.79	59	11	5.1
FIF1	7.6 μm	0.80	56	10.2	4.6
FIF0.5	4.9 μm	0.80	60	8.3	3.9
Control sample	200 nm	0.81	60	0.55	0.27

Film thickness of our samples increases nearly proportional to anodization duration and the highest solar cell efficiency is obtained with a sample using the 16 μm thick membrane prepared by 4 h anodization (Fig. 4-24 and Table 4-6). Compare front-illuminated (FIT4) to back-illuminated (BIT4) nanotube cells where both of them are anodized for 4 h in Fig. 4-24a, the gain in short-circuit current for FIT4 is due to a better light harvesting of front-illumination design. A higher fill factor is found because the barrier layer is almost removed during the second anodization. (see Fig. 4-23) Similarly, a larger of V_{oc} may be attributed to the presence of a compact layer of TiO_2 that is coated on FTO to prevent recombination (refer to Fig. 3-5 and Fig. 5-10). However, the gain in overall light conversion efficiency is not as pronounced as expected, which is probably attributed to light scattering and absorption caused by buffer and adhesive layer. In principle, further optimization will allow the PCE (currently 72% at 510 nm) of the front-illuminated nanotube-based DSC to reach a plateau of ~80%.

The ability to transfer large membranes also renders possible studies of the dependence of solar cell efficiency on the size of the active area (using parts cut from

the same membrane). Cells with different active area show the same trend in the variation of efficiency with tube length and active area (Fig. 4-24b). Generally, the larger the active area, the lower the fill factor is. The output power of the cells with larger active area suffers from energy loss due to a higher series resistance. Among the samples with area of 0.5 cm^2 studied, open circuit voltage (Fig. 4-24c) and fill factors are almost independent of film thickness. Impedance spectroscopy is also used to characterize the front-illuminated nanotube-based dye-sensitized solar cells. To evaluate the best cell with optimum tube length, a transmission line model is employed to fit the impedance spectra of the cell in dark under bias range from V_{oc} to 600 mV. A clear Warburg diffusion element at the intermediate frequency range in Nyquist plot is a key characteristic for a valid fitting by transmission line model. As seen from Fig. 4-25b, a linear line with a slope of 1 represents the Warburg diffusion. This observation supports the accuracy of fitting results. From the analysis of bias-dependent impedance spectra in the dark (Fig. 4-25) we can conclude that the highest short circuit current (and thereby highest efficiency) obtained for the 16 μm sample is essentially due to the highest ratio of recombination resistance over charge transport resistance (Fig. 4-24d). In other words, the higher the charge collection efficiency, the higher the photo conversion efficiency of the cell. The trend of electron life time (calculated by $\tau=R_{ct}C_{\mu}$) with respect to the tube length is in accordance to that of V_{oc}.

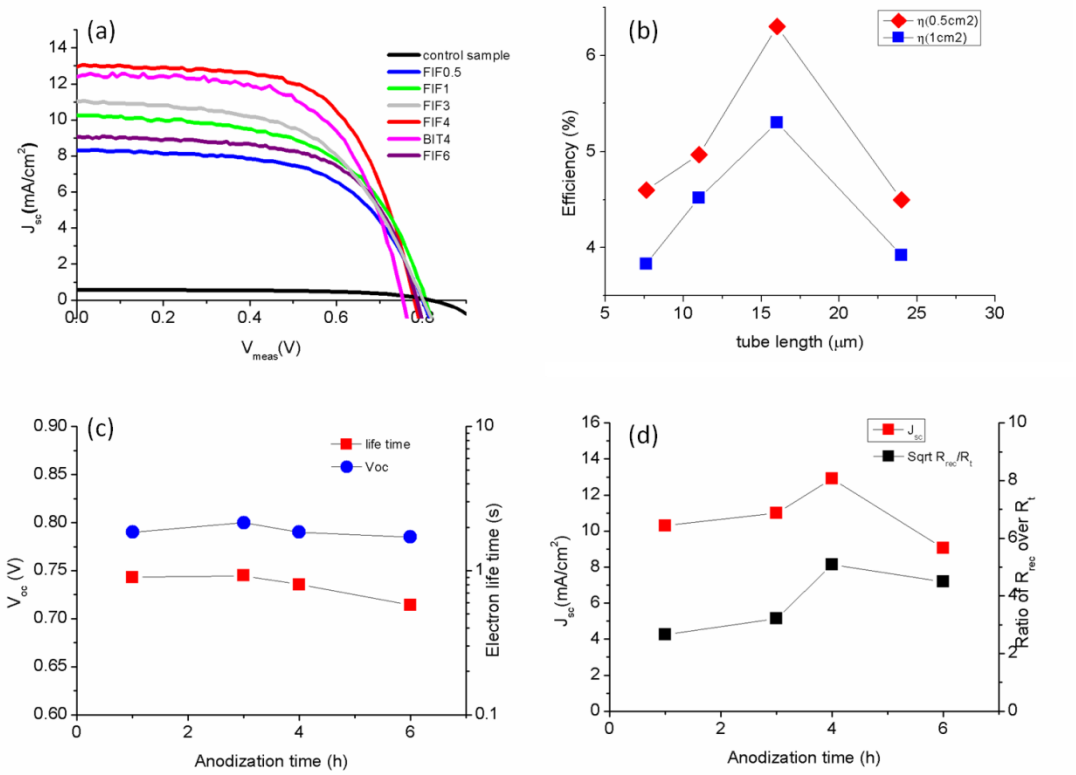

Figure 4-24: (a) J-V performance of front-illuminated nanotube-base dye-sensitized solar cells under standard test conditions; (b) cell efficiency and film thickness with respect to anodization time; (c) open circuit voltage and electron life time vs. anodization time; (d) correlations between short circuit current and the ratio of recombination/charge transport resistance. Front-illuminated DSCs abbreviated as FIF, back-illuminated devices as BIT. The number following this acronym specifies the duration of the first anodization in h. Fabrication process of back-illuminated reference cells follows the same procedure, except that the second anodization and membrane transfer steps are skipped.

The method of nanotube membrane detachment by two-step anodization and transfer described in this work is highly repeatable without the need for using acid or high power ultrasonic agitation, which both tend to deteriorate the quality the nanotube morphology. A mechanism is proposed to explain the detachment process. The flexible transfer method allows the membrane to be attached on various substrates. Using TiO_2 membranes transferred onto FTO, front-illuminated nanotube-based dye-

sensitized solar cells with high light conversion efficiency (up to 6.3%) and long electron lifetime are fabricated and characterised.

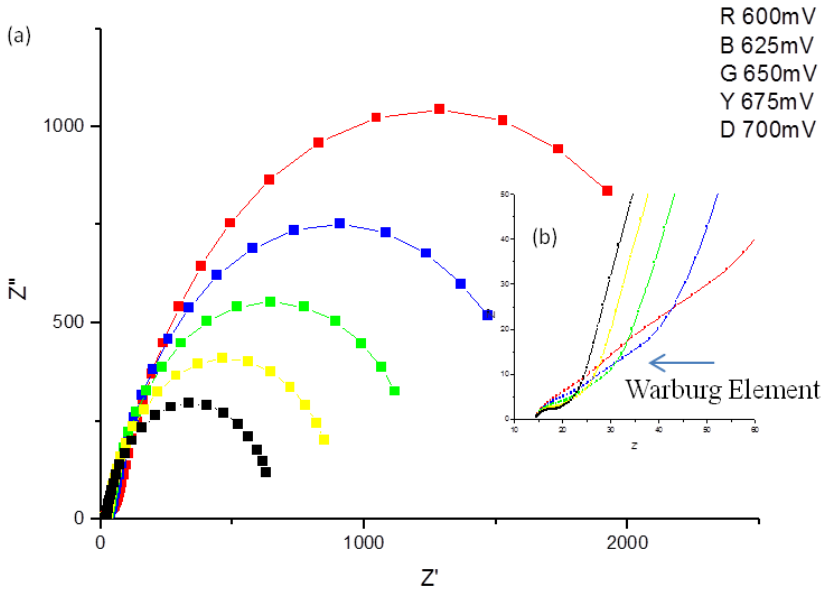

Figure 4-25: (a) Nyquist plot of front-illuminated nanotube-based DSC in dark with respect to negative bias on photo electrode from 700mV to 600mV; Inset picture (b) shows the magnified image of the same Nyquist plot in high frequency region, the Warburg phenomena represent the charge transport property of nanotube which is sensitive to bias as well.

References

1 K. Zhu, N.R. Neale, A. Miedaner, A. J. Frank, Nano Lett. 2007, 7, 69.

2 J. R. Jennings, A. Ghicov, L. M. Peter, P. Schmuki, A. B. Walker, J. Amer. Chem. Soc. 2008, 130, 13364.

3 O. K. Varghese, D. Gong, M. Paulose, K. G. Ong, E. C. Dickey, C. A. Grimes, Adv. Mater. 2003, 15, C662.

4 G. K. Mor, K. Shankar, M. Paulose, O. K. Varghese, C. A. Grimes, Nano. Lett. 2005, 5, 191.

5 B. O'Regan, M. Grätzel, Nature 1991, 353, 737-740.

6 L. K. Tan, K. K. Manippady, W. W. An, H. Gao, Appl. Mater. Interfaces 2010, 2, 498.

7 F. Fabregat-Santiago, E. M. Barea, J. Bisquert , G. K. Mor, K. Shankar , C. A. Grimes, J. Am. Chem. Soc. 2008, 130 , 11312.

8 K. L. Li, Z. B. Xie, S. Adams, Z. Kristallogr. 2010, 225, 173.

9 A. Ghicov, P. Schmuki, Chem. Commun. 2009, 20, 2791.

10 Z. B. Xie, S. Adams, D. J. Blackwood, J. Wang, Nanotechnol. 2008, 19 , 405701.

11 C. Ruan, M. Paulose, O. K. Varghese, G. K. Mor, C. A. Grimes, J. Phys. Chem. B 2005, 109,15754.

12 K. Zhu, S. R. Jang, A. J. Frank, J. Phys. Chem. Lett. 2011, 9, 1070.

13 M. Paulose, K. Shankar, O. K Varghese, G. K. Mor, B. Hardin, C. A. Grimes, Nanotechnol. 2006, 17, 1446.

14 C. H. Chen, K. C. Chen, J. L. He, Curr. Appl. Phys. 2010, 10, S176.

15 J. H. Park, T. W. Lee, M. G. Kang, Chem. Commun. 2008, 25, 2867.

16 B. X. Lei, J. Y. Liao, R. Zhang, J. Wang, C. Y. Su, D. B. Kuang, J. Phys. Chem. C 2010, 114, 15228.

17 Q. W. Chen, D. S. Xu, J. Phys. Chem. C 2009, 113, 6310.

18 L. L. Li, Y. J. Chen, H. P. Wu, N. S. Wang and E. W. G. Diau, Energy Environ. Sci. 2011, 4, 3420.

19 J. Lin, J. F. Chen, X. F. Chen, Electrochem. Commun. 2010, 12 , 1062.

20 G. K. Mor, O. K. Varghese, M. Paulose, K. Shankar, C. A. Grimes, Sol. Energy Mater. Sol. Cells 2006, 90, 2011.

21 S. Q. Li, G. M. Zhang, J. Ceram. Soc. Jap. 2010, 118, 291.

22 D. A. Wang, L. F. Liu, Chem. Mater. 2010, 22, 6656.

23 Q. W. Chen, D. S. Xu, J. Phys. Chem. C 2009, 113, 6310.

Chapter 5 *All-solid-state nanotube-based dye-sensitized hetrojunction cells*

The solution casting method to introduce hole transporting medium (HTM) is currently the most successful method for fabricating high efficient inorganic solid-state dye-sensitized heterojunction cell (SSDSC). The identification of a suitable deposition solvent with a moderate amount of solubility, controlled crystallization rate and good solution penetration into the mesostructured TiO_2 are three prerequisites for the feasibility of this method. Other than those, a hole-transporting medium with good stability and conductivity would be more suitable for the application in dye-sensitized heterojunction cells. Among the inorganic HTM, CuI and CuSCN are two candidates as both of them can be dissolved in a water-free solvent with a moderate amount of solubility. The valence band edges of both are higher than the HOMO level of dye molecule so that the holes generated from photo-excitation are transferred to the valence band of the HTM and finally collected at counter electrode through hopping mechanism. Of these two HTM candidates that are both employed in my experiments, CuI is the more conductive so that a higher efficiency can be achieved due to a higher short-circuit current [1]; CuSCN is less conductive but more stable, so that the cell does not degrade in a few hours after assembly (as is the case for CuI). A major challenge for both materials is that they tend to crystallize fast and consequentially penetration into the porous structure of

TiO_2 is usually poor. Optimization of the inorganic HTM and its application in front-illuminated nanotube-based SSDSCs are discussed in this chapter.

5.1 Preparation of a compact TiO_2 layer

A compact TiO_2 layer to prevent short-circuit of the cell is necessary for the functioning of the cell and particularly crucial to prevent a direct contact between hole-conductor and FTO in solid-state cells. Spray pyrolysis has been demonstrated to be suitable for growing the required layer of compact TiO_2 of less than 100nm thickness. A compact TiO_2 layer with this thickness is sufficiently insulating to prevent the cell from short-circuit, but still the additional resistance for the charge collection is still acceptable. The spray pyrolysis is usually conducted at 450 ℃ on a hotplate. The cleaned FTO substrate is covered by a protective aluminium foil with an opened window. The active layer is applied within the window defined area where a thin layer of compact TiO_2 is grown. To achieve reproducible results, a careful control of experimental parameters is very important. Besides the spray pressure which defines the size and uniformity of the mists, the height between nozzle and substrate, how fast to trigger the nozzle, and the air flow in fumehood have to been taken into account in order to grow a uniform thin layer. Still, this approach frequently ends up with a non-uniform film, with some parts not fully covered by a compact TiO_2 layer or with overly thick TiO_2 layers. Therefore, the reliability of this method makes it not suitable for fabricating solid-state DSCs in our lab. A more

elaborate apparatus with a computer-controlled operation of a custom-designed nozzle is more favourable for this experiment. [2,3]

Alternatively, spin coating is found to be more reproducible. In this approach, the optimized spin-coating solution is the prerequisite for a good quality film coating. Titanium isopropoxide is dissolved in absolute 2-propanol. Only freshly prepared solution can be used for this purpose, since the moisture level in Singapore is often more than 80% so that a stored solution would almost inevitably be contaminated by water. Additionally, glacial acetic acid (vol ratio given in Table 5-1) is added to the solution to prevent the hydrolysis of titanium isopropoxide. Triton X-100 is added to improve the film uniformity by improving the viscosity of the solution.

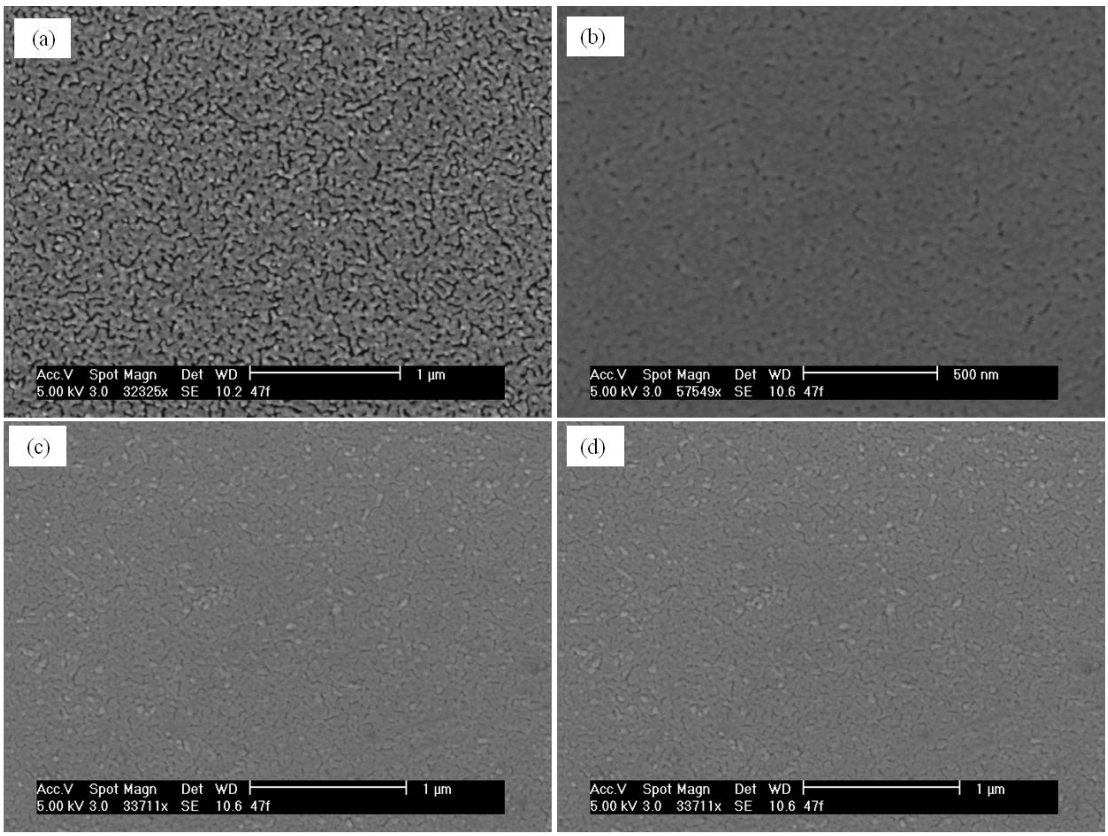

Figure 5-1: Top view of compact TiO_2 films produced by spin-coating by solutions with the compositions A-D given in Table 5-1: composition A (a); composition B (b); composition C (c); and composition D in (d).

In order to determine the optimized composition of the spin coating solution, a range of compositions (given in Table 5-1) has been studied. For all the solution a 2×2 cm^2 TiO_2 film is deposited by dropping 60 µl of the solution over 1 min on a cleaned FTO slide rotating with a fixed speed of 3000 rpm and annealing the film at 450 ℃ on the hotplate for 30 min.

From the top view SEM pictures of the films deposited using solutions with four different compositions, it is observed that the solution with composition B results in the most uniform film as seen in Fig. 5-1. From naked eyes, sample D appears more opaque indicating there is a moderate degree of hydrolysis process has taken place. Composition A, B and C lead to uniform films as judged from naked eyes, but only the film prepared by composition B turns out to be compact when investigated by SEM (as observed in Fig. 5-1b).

The thickness of the deposited layer prepared by spin-coating solution B is then measured at different spin-coating speeds. As discussed above, a compact film of TiO_2 of 100 nm is optimized for dye-sensitized solar cell application [2]. The film thickness can be expected to be inversely proportional to the spin-coating speed and the duration of the spin-coating process. According to the results shown in Table 5-2, only a minor variation of the average film thickness is observed for the samples prepared by different spin-coating speeds. For all the parameter choices the average thicknesses are in the range 92 – 131 nm. As expected, the highest film thickness is prepared by 3000 rpm while the thinnest film is prepared by 5000 rpm.

Table 5-1: Different compositions of spin-coating solution forming TiO_2 compact layer in volume ratio.

	$Ti(OC_3H_9)_4$	IPA	Glacial acetic acid	Triton X-100
Composition A	1	10	1	1
Composition B	1	10	1	2
Composition C	1	10	2	1
Composition D	1	5	1	1

Table 5-2: Measured thickness of the samples prepared by spin-coating method at different speed by surface profilometer.

Speed/rpm	Time (s)	Measured sample thickness (nm)				Avg (nm)	Stdev (nm)
3000	30	108	115	115	113	112.75	3.3
	60	113	103	106	107	107.25	4.2
4000	30	98	109	95	101	100.75	6
	60	110	90	90	97	96.75	9.4
5000	30	106	122	93	107	107	11.8
	60	107	76	126	106	103.75	20.7

With increasing speed it is also found that the standard deviation of the film thicknesses from 4 measurements of the same film systematically increases, so the slower speed of 3000 rpm yields the most uniform film with the lowest standard deviation. For still slower rotation it was found in a separate set of experiments that the film thickness increased considerably, so that the amount of solution employed

would have to be reduced accordingly, which again makes it more difficult to achieve a uniform coating. The tendency of growing a thinner film by a longer spin-coating time is not clearly observed. Based on these experiments, the optimized conditions for the deposition of the compact TiO_2 layer have been chosen: The compact layer is prepared by spin-coating using solution B, and the sample is spin-coated at 3000 rpm for 1 min.

5.2 Additive effect on hole-conductor CuI

In this section the fabrication process of CuI-based SSDSCs is introduced. CuI is first dissolved in pure acetonitrile overnight, and the solution is thereafter ultrasonicated and centrifuged. The solution casting deposition is conducted while placing the sample on a hotplate of 120 ℃. A pipette is used to withdraw 2 μl of clean solution so as to apply it on the active area of the sample. This process is repeated 20 times until the deposited film covers up the dye-coated TiO_2 mesoporous film. A thin layer of graphite powder is covered on top followed by an additional FTO glass to assemble the cell.

The resulting crystal size of CuI is very large as shown in Fig. 5-2 (a,b). A side view picture (Fig. 5-2c) of the sample shows that deposited CuI tends to grow to a large crystal size which is not suitable for pore-filling. This may explains the poor cell performance of CuI-based dye-sensitized solar cell demonstrated in Fig. 5-2d.

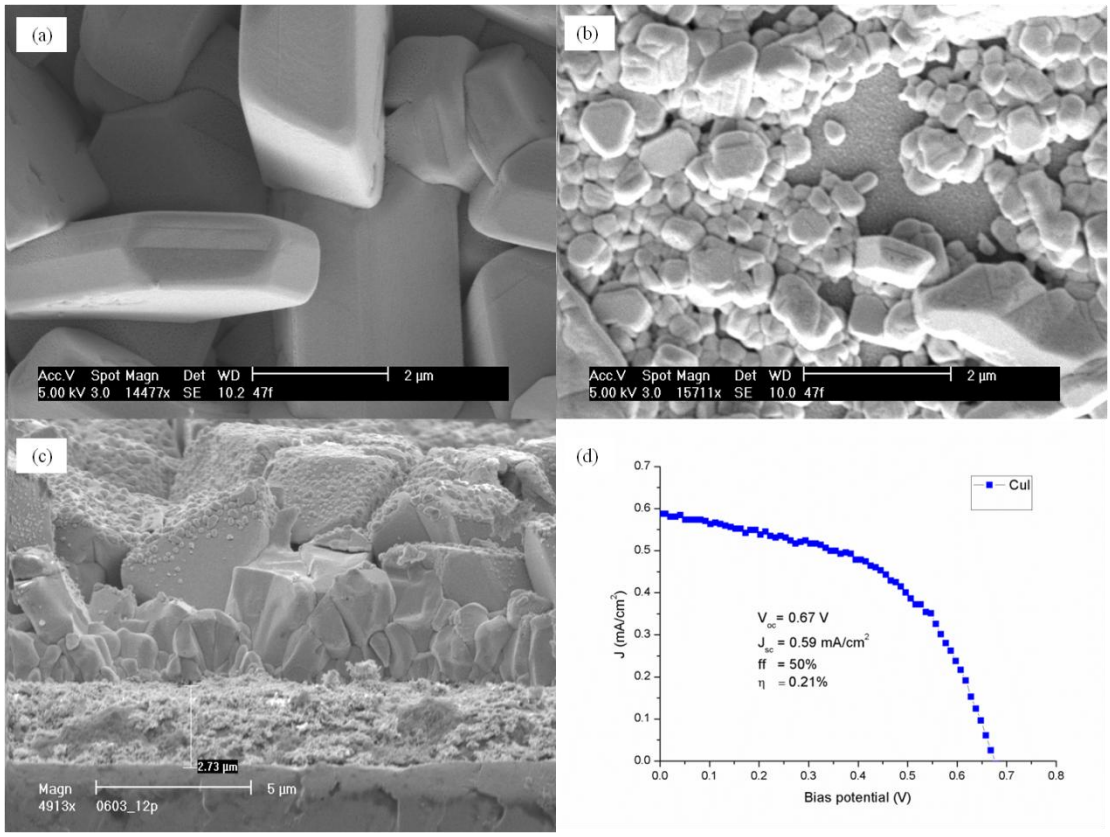

Figure 5-2: CuI on NP TiO_2 by solution castingof CuI from a acetonitrile solution. The top views (a,b) of the CuI indicate that the particle size is very large (typically ~5µm); CuI is nucleated at the top surface of TiO_2 instead of penetrating into (c); A SSDSC based on this film shows an efficiency of 0.21% under STC.

It has been reported that adding the ionic liquid 0.2mM 1-ethyl-3-methyl-imadazolium thiocyanate (EMISCN) is helpful to inhibit crystal growth so that smaller crystallites more suitable for penetration can be achieved [4]. When reproducing these experiments in our lab, it is confirmed that the particle size of deposited CuI from the solution with EMISCN as additive is considerably smaller as a typical value of the deposited CuI measured by SEM is close to 30 nm [4], but the majority of the deposited film remains in gel form instead of solid form, as the ionic liquid does not evaporate. Raising the temperature slightly (to 140 ℃) or reducing the concentration of EMISCN did not resolve this problem. Gold sputtering or graphite

powder cannot be used as counter electrode if EMISCN is added into CuI acetonitrile solution. Thus, the best efficiency reached in my experiments with CuI as the hole-conductor is only 0.21%, and the cell efficiency degraded within an hour to a negligible value. This is probably due to a fast oxidation of I^- to I_2 under ambient environment. Therefore we shifted our attention to CuSCN as the stability of this material in air is more promising for solar cell application.

5.3 Optimization of CuSCN hole-transporting medium

5.3.1 Preparation of hole-transporting medium

As discussed previously, compare with CuI inorganic HTM CuSCN is more stable without severe degradation or oxidation despite of a relatively lower conductivity. α-CuSCN, β-CuSCN, $Cu(SCN)_2$ and $Ni(SCN)_2$ are dissolved in 2-propyl sulphide (PS) [5] to produce saturated stock solutions two days before use. The approaches to fabricate α-CuSCN and $Ni(SCN)_2$ are documented in chapter 3. Briefly, α-CuSCN/$Cu(SCN)_2$ are precipitated [6] from LiSCN and $Cu(ClO_4)_2$ aqueous solutions with/without triethylammonium acetate buffer solution. The nature of the precipitate is confirmed by XRD. $Ni(SCN)_2$ is precipitated from NH_4SCN and $NiCl_2$ aqueous acetic acid solution (acid to water volume ratio 1:10). The precipitates are filtrated, rinsed and dried by vacuum oven at 80℃ overnight [7]. Triethylammonium thiocyanate (THT) [1,8] is prepared by mixing NH_4SCN with excess triethylamine at 100℃ with vigorous stirring. After completion of the reaction the bottom layer is sucked by a dropper (the density of THT is larger than that of the remaining

triethylamine), the optimized recipe for solution casting of the HTM is to add 0.2 mM THT into a mixture of α-CuSCN, $Ni(SCN)_2$ and β-CuSCN saturated solutions in PS (vol. ratio 1:1:10). The colour of above mentioned stock solutions are shown in Fig. 5-3. Additional 10% vol. PS is added to dilute the saturated solution to allow for good reproducibility.

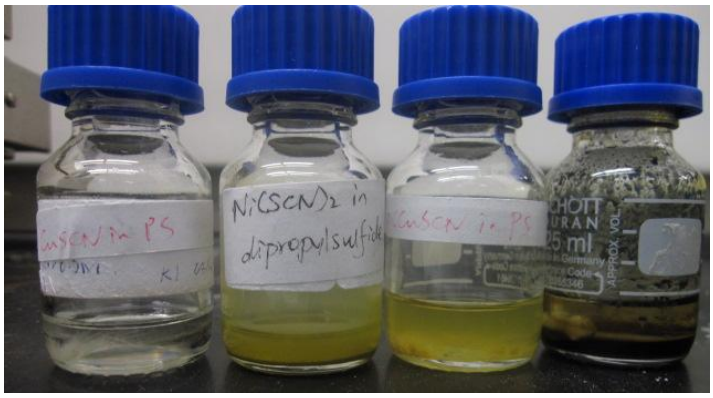

Figure 5-3: From left to right: 0.2 mg CuSCN (transparent), $Ni(SCN)_2$ (dark yellow), $Cu(SCN)_2$ (light yellow) and THT/CuSCN paste (transparent solution, but paste converts from white to dark after a few days) in propyl sulphide (PS) saturated solution.

The dye-coated photoelectrode is placed on a 45 ℃ pre-heated hotplate. The active area of the 5 μm thick photo-electrode is 0.25 cm^2. A drop (2.5 μl) of as-prepared solution is evenly spread on the titania layer. At least 10s are allowed in-between each casting to allow for the solution drop to penetrate into TiO_2, the solvent to evaporate and the HTM to nucleate. This process is repeated 50 times at 45 ℃; then the temperature is raised by 5 ℃ every five drops from the 50^{th} to the 70^{th} drop. This turned out to be crucial as the first 50 castings at a lower temperature allow for better pore-filling, while increasing the temperature at the later stage ensured a more complete coverage. The surface temperature of the hotplate is monitored by an infrared temperature sensor. The optimized number of drops and volume per drop

obviously varies with the active area and layer thickness. The samples are finally dried in a vacuum oven over night before measurement. After complete solvent evaporation, the non-active area is protected by a layer of scotch-tape; a thin layer of fine graphite powder is evenly spread and covered on top of the CuSCN layer. The graphite powder is then covered by another conductive glass slide and the cell is clamped by clips for a quick measurement or sealed by epoxy resin for stability tests.

The optimization of the CuSCN solution for casting method, for instance how much amount of THT and $Ni(SCN)_2$ leads to the best film with good quality, better pore-filling and enhanced conductivity, is explored in details in the next few sections.

5.3.2 THT additive and $Ni(SCN)_2$ doping effect

β-CuSCN is selected to be the hole-transporting medium for dye-sensitized heterojunction cell because of the position of the valence band, reasonable conductivity and transparency. Therefore, the optimization of CuSCN for SSDSC is based on balancing transparency and conductivity. Saturated $Cu(SCN)_2$, $Ni(SCN)_2$ or α-CuSCN PS solution is mixed with β-CuSCN saturated PS solution (1:10 vol.) to study their independent influences as additive on the conductivity of β-CuSCN. To minimize the geometry effect on resistance in the conductivity measurements, films of identical thickness are prepared by solution casting on quartz, and the distance between two mask-defined gold-sputtered electrodes is kept constant. $Cu(SCN)_2$ is a candidate used to study doping effects of CuSCN in the literature [9], and some related experiments are also given below. It is confirmed that there is a positive effect of $Cu(SCN)_2$ on the conductivity of β-CuSCN, but the stability of HTM becomes

worse. The conductivity of α-CuSCN is higher than that of β-CuSCN, but its valence band position does not match the HOMO level of the dye molecule. Therefore mixtures of α- and β-CuSCN have been explored. Still, increasing the α-volume ratio between the saturated α- and β-CuSCN solutions to more than 1:10 results in no additional enhancement in short-circuit current, because the deposited film becomes yellowish rather than transparent. $Ni(SCN)_2$ doping suffers from a similar problem. Moreover, it is found that, when the volume ratio between β-CuSCN and $Ni(SCN)_2$ saturated solutions increases from 10:1 to 10:5, the deposited film tends to crack. An impedance study of the effect of $Ni(SCN)_2$ doping on the conductivity of the HTM film is illustrated in Fig. 5-4. After considering film quality and transparency, the optimized ratio is found to be 10:1.

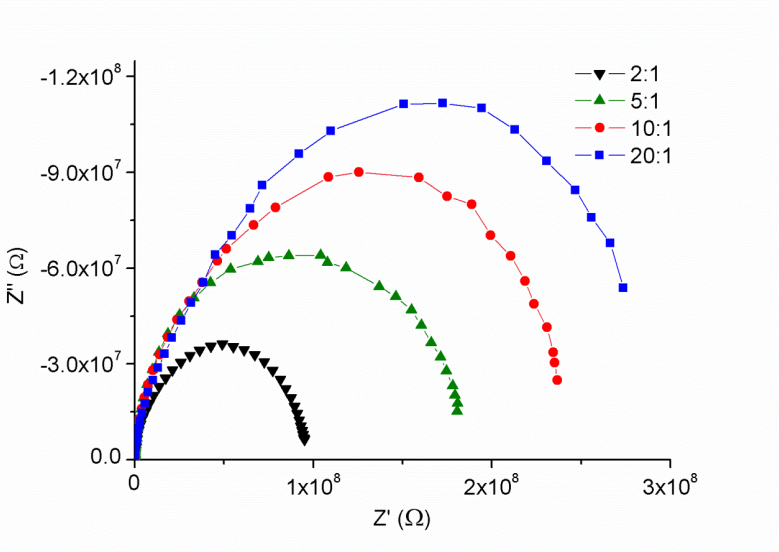

Figure 5-4: Conductivity measurements of a variety of CuSCN/$Ni(SCN)_2$ HTM with different compositions through symmetric cell by EIS. Samples are prepared by solution casting method where the ratio of CuSCN to $Ni(SCN)_2$ is controlled by mixing saturated CuSCN/$Ni(SCN)_2$ propyl sulphide solutions according to vol ratio. The labels of the different measurements refer to this volume ratio of the saturated CuSCN and $Ni(SCN)_2$ solutions. The film deposited is measured immediately after casting method on hotplate after all the solvent is dried observed by naked eyes.

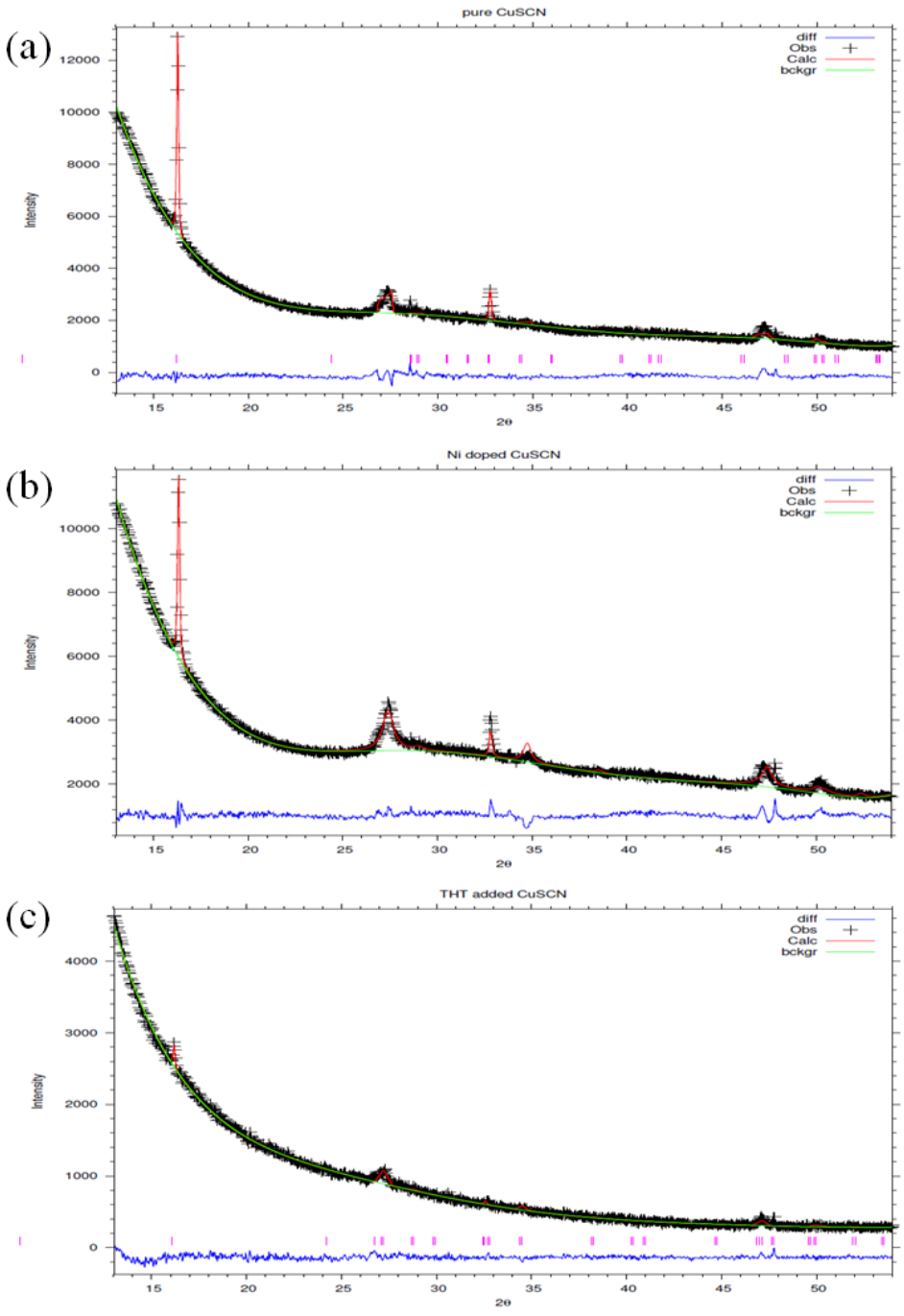

Figure 5-5: Powder X-ray diffraction pattern of solution casted sample of pure CuSCN on Si substrate (a); 1:10 $Ni(SCN)_2$ to CuSCN saturated solution; (c) 0.2 mM THT added CuSCN PS solution. The measured results are displayed in thin cross, calculated results are in red, background is in green and the difference are highlight in blue. There are only peak position shift in XRD pattern of THT additive and Ni doping in (b) and (c) compared to XRD pattern of pure beta CuSCN in (a).

Effects of $Ni(SCN)_2$ and THT on crystallinity and lattice parameters of as-deposited solution-cast β-CuSCN films are studied by Rietveld refinement of X-ray diffraction data in Fig. 5-5. We find as expected that doping leads to an expansion of the lattice constants from a = 3.62(2) Å, c = 32.88(8) Å, V = 373.85(8) $Å^3$ to a = 3.87(3) Å, c = 33.08(4) Å, V = 429.9(1) $Å^3$ for THT additive and a = 3.85(6) Å, c = 32.89(6) Å, V = 423.65(8) $Å^3$ for Ni^{2+} doping. At the same time the peaks of the doped samples exhibit a more pronounced broadening and less preferred orientation due to the reduced crystallites size that also leads to a more random crystallite orientation. A similar effect of THT on CuSCN is observed, this suggests that other than crystal growth inhibition, THT is also exhibited a doping effect. From the pronounced increase in the lattice constants (a = 3.87(3) Å, c = 33.08(4) Å, V = 429.9(1) $Å^3$) it can be seen that the THT acts as a dopant modifying the stoichiometry of the compound and hence the crystal structure. *Premalal et al.* [8] suggest based on their FT-IR and XRD studies that the additive THT leads to the deposition of CuSCN with enhanced p-type conductivity by replacing some of the Cu(I) ions by triethylamine coordinated Cu(I), accompanied by an incorporation of neutral $(SCN)_2$ into the structure. This might explain the pronounced volume expansion, but the increase in hole conductivity might require that the presumed interstitial $(SCN)_2$ oxidizes Cu(I) to Cu(II). At the same time THT acts as an adsorbent leading to an enhanced crystallite shape anisotropy (short axis along c) and thereby a strongly enhanced preferred orientation in the powder patterns. No second phase is observed in the refinement, but especially for the THT-doped sample the intensity of the Bragg peaks is reduced and a broad X-ray amorphous hump is observed in Fig. 5-5c.

To find the optimum doping among the options discussed above, we compared the effect of the different dopants on the impedance of the HTM film and the achievable short-circuit current of SSDSCs using these HTMs. Both $Cu(SCN)_2$ and $Ni(SCN)_2$ doping improve the conductivity of β-CuSCN as demonstrated in Fig. 5-6a. Similarly the addition of the high conductivity α-phase of CuSCN and of THT enhances the electronic conductivity, as obvious from the impedance spectra of the symmetric cells. It may be noted that the conductivity enhancement due to THT is even more pronounced than the effect of the doping by divalent cations. When assembling SSDSCs based on CuSCN with individual dopants or additives, only cells with THT-modified β-CuSCN exhibited a strong increase in the short-circuit current density (as the large crystallite size of doped or undoped films in the absence of THT prevents a penetration of CuSCN into the TiO_2 layer). Therefore the study is extended to investigate the effect of the other dopants on THT-modified β-CuSCN. Fig. 5-6b highlights the improvement in short-circuit current of SSDSC by the more conductive HTM when using a fixed amount of THT both to enhance conductivity and to improve pore-filling by the reduced crystallite size.

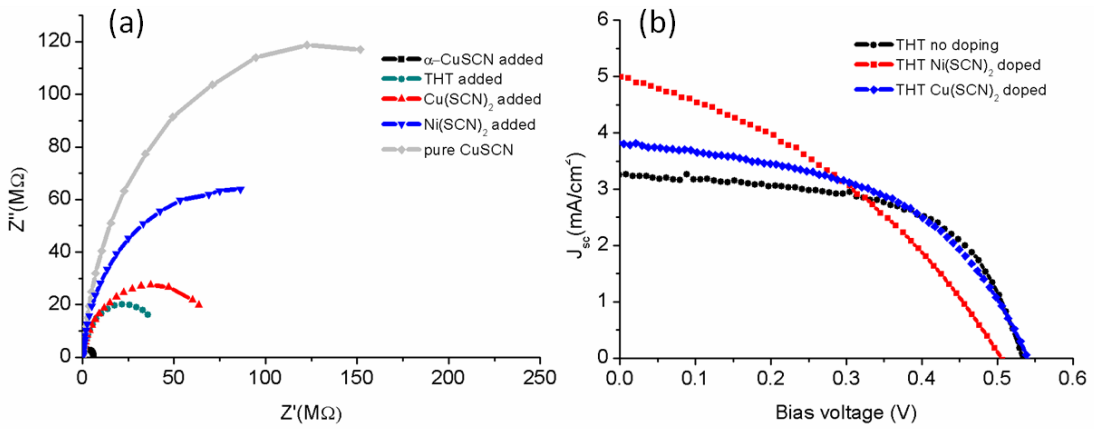

Figure 5-6: (a) EIS study of symmetric cells show an increase on conductivity of hole conducting materials by doping, which explains the increase of J_{sc}. (b) J-V curves of front-illuminated all-solid-state dye-sensitized solar cells using various doped solution via dropping methods.

The contribution of $Cu(SCN)_2$ doping to current enhancement is not stable; a decay in current is usually observed after long time exposure to illumination. The role of α-CuSCN is mainly to enhance conductivity as indicated in Fig. 5-6(a). So the optimized solution recipe contains 0.2 mM THT in a mixture α-CuSCN, $Ni(SCN)_2$ and β-CuSCN saturated PS solutions (vol. ratio 1:1:10) with additional 10 vol% PS added to allow good reproducibility.

5.3.3 Optimum solution volume and effect of drying in vacuum

Fig. 5-7 displays how the J-V curve measured under standard testing conditions is influenced by the THT additive and the amount of solution employed for the 5 μm thick film (with an area of 0.5 × 0.5 cm^2). For the sample prepared by casting 30 drops of the solution without THT, CuSCN tends to nucleate on the very top surface of TiO_2, so that the dye loaded surface is not fully utilized. Such a structure leads to

high V_{oc} (no shunts) but low J_{sc} (low active surface area). In contrast, 0.2 mM THT additive helps to modify the crystallization behaviour of CuSCN so that a better penetration is achieved. Thereby CuSCN fills the bottom of the TiO_2 layer first without forming an over-layer on top. This explains the increase in J_{sc} and decrease in V_{oc} (see black and blue curves) in Fig. 5-7 for the sample using 30 drops of the solution with the THT additive. When varying the amount of solution used from casting 30 to 70 drops, both J_{sc} and V_{oc} increase further supporting the validity of this hypothesis. The higher amount of solution allows achieving both a good penetration of CuSCN into the TiO_2 layer and the formation of a thin over layer of CuSCN that prevents local shunts. TiO_2 layer cannot be covered by CuSCN by insufficient solution casting while too many drops of casting will result in a thick CuSCN overlayer of high resistance. The optimum number of drops depends on the nanostructure of the TiO_2 film. For instance, an also 5 μm thick nanotubular TiO_2 film requires only 45 drops for the same active area. The optimized drops of casting solution for both nanoparticle and nanotube-based SSDSCs are summarized in Table 5-3. The significance of this droplet optimisation is discussed in section 5.3.4 along with the effect of nanotube length variation.

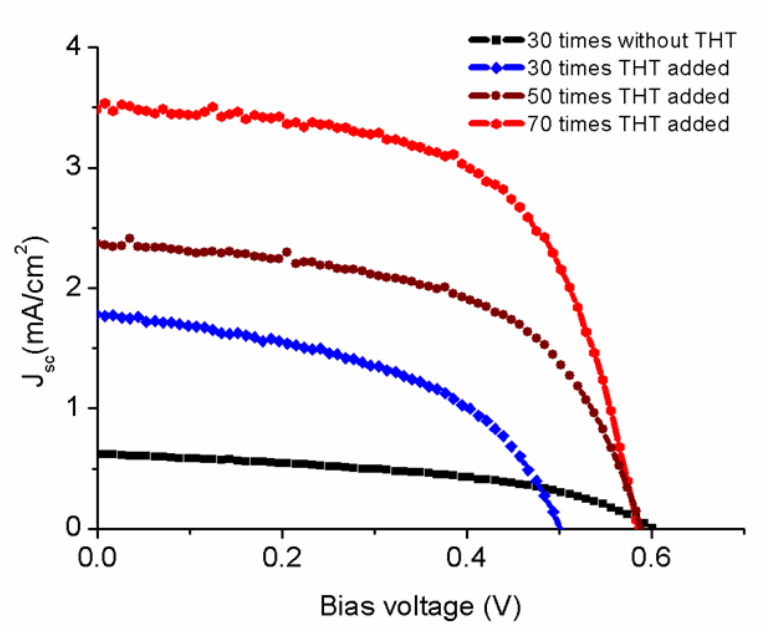

Figure 5-7: The effect of THT additive and number of drops for the casting of the optimised HTM solution on a 5 µm NP film.

Another very important experimental parameter for fabricating highly efficient SSDSC is the control of the drying process of the deposited CuSCN film in vacuum. There is no obvious crystallization detected by XRD after two days drying in vacuum so that we can conclude that the enhancement in conductivity is due to further solvent evaporation only. As shown in Fig. 5-8, the resistance of the deposited CuSCN film reduced considerably after two days drying in vacuum. The film is exposed to ambient atmosphere during the measurement. Thereafter the vacuum drying is continued for 5 more days. A subsequent test however showed a slight increase in the resistance. From this study, it appears helpful to store the film for two days in evacuated desiccators (with continuous evacuation by the vacuum pump) before assembly, while a longer storage becomes detrimental.

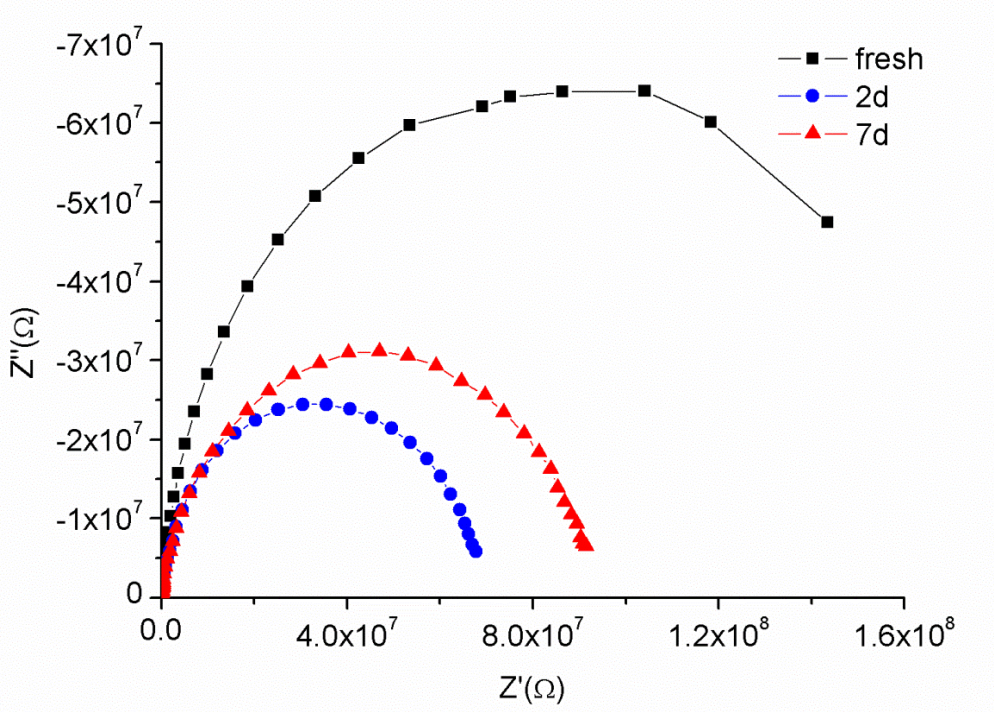

Figure 5-8: Vacuum drying effect on the conductivity of CuSCN film symmetric cell. Conductivity of the film is the highest after two days drying, however it drops after five more days drying.

5.3.4 Length effect of nanotube-based SSDSCs

The preparation of TiO_2 nanotubes (NT) on FTO is reported in our previous study.[10] Briefly, FTO glass is pre-coated with a compact layer of TiO_2 by spin-coating.[2] Titania nanotube arrays are fabricated by anodizing a Ti foil in NH_4F contained ethylene glycol and water mixture solution at 50 V. A second anodization of the same sample is conducted at 70 V with a higher initial ramp rate after annealing lead to the detachment of nanotube membrane. The detached membrane is transferred onto FTO in an isopropyl alcohol (IPA) containing Petri dish. The membrane is finally fixed onto FTO by infiltration of few drops of Titanium

isopropoxide IPA solution and followed by annealing. After $TiCl_4$ treatment, the sample is then dye soaked overnight in 0.5 mM solution of the cis-bis(isothiocyanato)bis(2,2'-bipyridyl-4,4'-dicarboxylato)-ruthenium(II) ("N3") dye in ethanol. Nanoparticle (NP) DSCs are produced by screen-printing using the commercial paste 18T (Dyesol).

The optimized solution is applied on NP & NT based SSDSCs respectively to study the thickness effect on photovoltaic performance. In harmony to earlier literature reports, [6] an optimized thickness to maximize the efficiency of NP cells is found to be ca. 5 μm. A further increase in thickness enhances the effective dye-loading yet causes severe recombination effects as given in Table 5-3. This limitation in the layer thickness and hence efficiency can be overcome by engineering the surface, the architecture and the interface between photo-electrode and hole-transporting medium. Increasing the charge-collection efficiency, and reducing the dark exchange current by slowing down the recombination process are thus possible ways to boost the performance of the SSDSC. The faster charge transport and slower recombination rate in titania nanotube membranes makes them competitive candidates for photo electrodes [11].

Table 5-3: The effect of the thickness of active layer on light conversion efficiency of nanoparticle-based and nanotube-based fresh-assembled solid-state dye-sensitized solar cells. Standard deviation is displayed inside the bracket among at least three samples for each condition. Since the porosity of nanoparticle is different from nanotube arrays, the optimized drops of casting solution are dependent on the thickness of the nanostructured TiO_2 layer.

	NP			NT	
Thickness	Efficiency	Drops	Length	Efficiency	Drops
2.5 µm	0.67(0.1) %	25~30	5 µm	1.31 (0.1)%	40~45
5 µm	1.14(0.2) %	45~50	7 µm	1.86 (0.15)%	55~60
7.5 µm	0.16(0.03) %	65~70	10 µm	0.62 (0.2)%	70~75

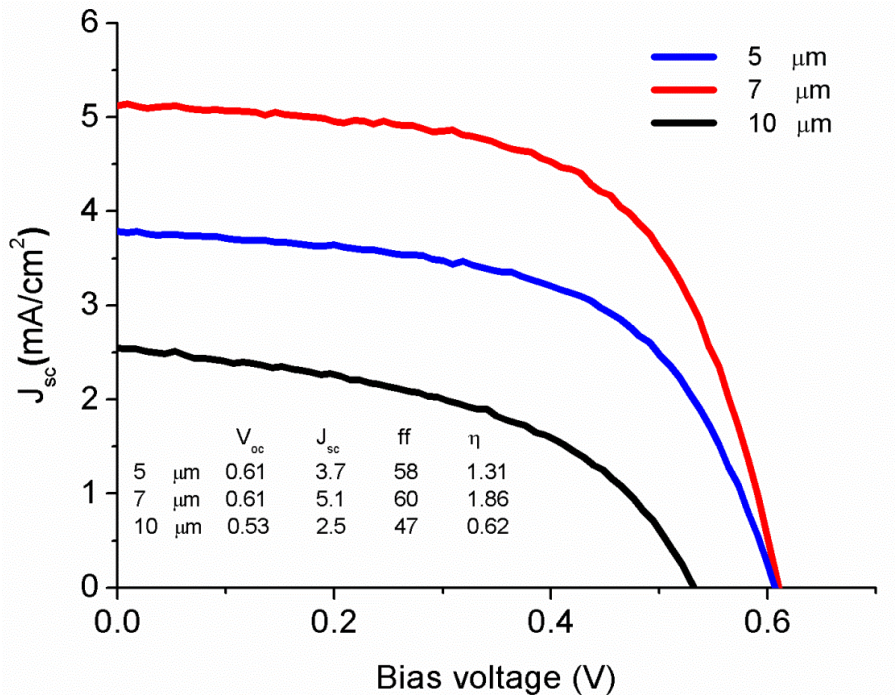

Figure 5-9: Length effect of nanotube-based SSDSCs with optimized CuSCN film by casting method. The measurement is conducted immediately after assembly under STC.

The characterisation of SSDSCs based on transferred nanotube membrane arrays of different thicknesses (see Fig. 5-9) in the frame of this project revealed that the optimum thickness of the nanotubular membrane is higher than the optimum

thickness for nanoparticular TiO_2 films discussed above. When the TiO_2 nanotube membrane thickness is increased to 7 µm, the photovoltaic performance of a nanotube-based cell increases to 1.9% (V_{oc} = 0.6 V, J_{sc} = 5.1 mA/cm^2, ff = 0.6), while further increase in tube length again leads to a massive drop in efficiency to 0.62% (V_{oc} = 0.53 V, J_{sc} = 2.5 mA/cm^2, ff = 0.62). As the optimum thickness of titania nanoparticle-based SSDSCs is found to be only 5 µm. A longer effective diffusion length in the NT-based cells is most likely responsible for this phenomenon, as open-circuit voltage decay and impedance fitting in dark suggest that there is a longer electron life time in nanotubes as seen in Fig. 5-10.

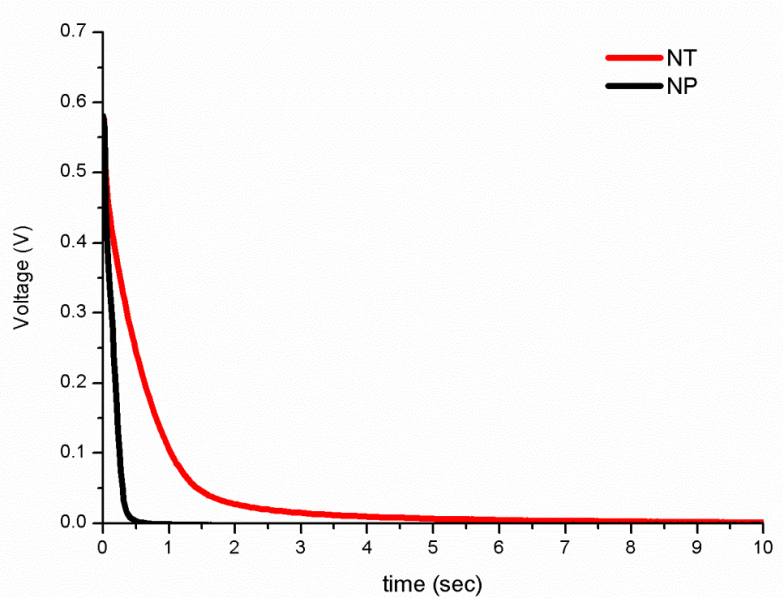

Figure 5-10: Open circuit decay curves of 5 µm nanoparticle and 5 µm nanotube-based SSDSCs.

In order to understand why the optimum TiO_2 layer thickness in nanotube SSDSCs is considerably larger than in nanoparticle-based SSDSCs, we investigated the CuSCN penetration depth. Cross section SEM images of ~5 µm thick titania nanotube on FTO before and after CuSCN deposition in Fig. 5-11 (a, b) demonstrate that the tubular

TiO_2 features are covered by a smoother layer of CuSCN. If assuming packing density of nanorod (accounting outer diameter of the nanotube) is 70%, an EDX analysis for a point close to the bottom of the nanotubes in Fig. 5-12 shows the Cu: Ti ratio is close to 1:1corresponding to full (100% by assuming that ID/OD of nanotube is 3:4) penetration of the CuSCN. While when the nanotube length extends to the 10 µm, Cu:Ti ratio near the bottom drops to 0.1:1. In comparison, *O'Regan et al.* [12] reported that for 5.8 µm thick nanoparticle titania films the degree of pore-filling by CuSCN is only ca. 65% and nearly 100% penetration is observed only for films of less than 2 µm in thickness. Thus the observed larger optimum thickness of SSDSCs employing nanotubular TiO_2 can be understood as a consequence of the obviously more complete penetration of the solid HTM into the nanostructured TiO_2 layers.

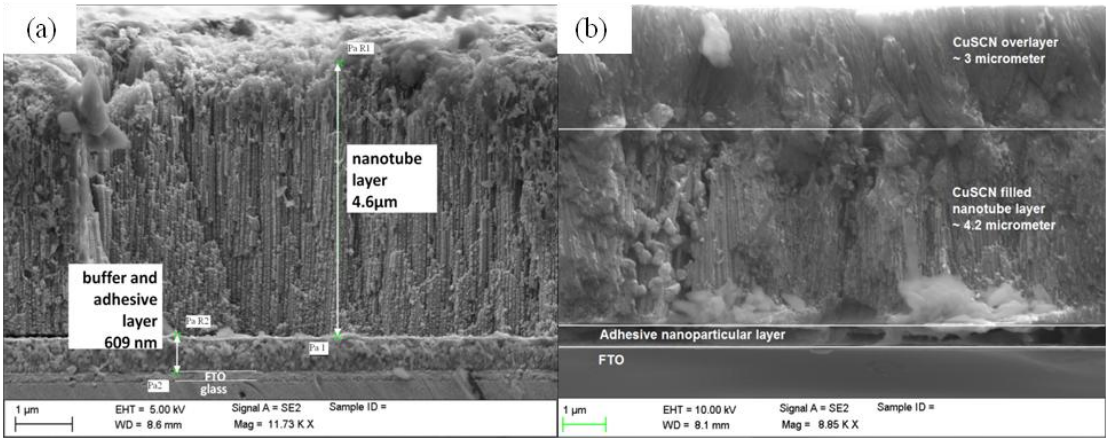

Figure 5-11: Side view of the same membrane attached on FTO (a) and after CuSCN deposition (b).

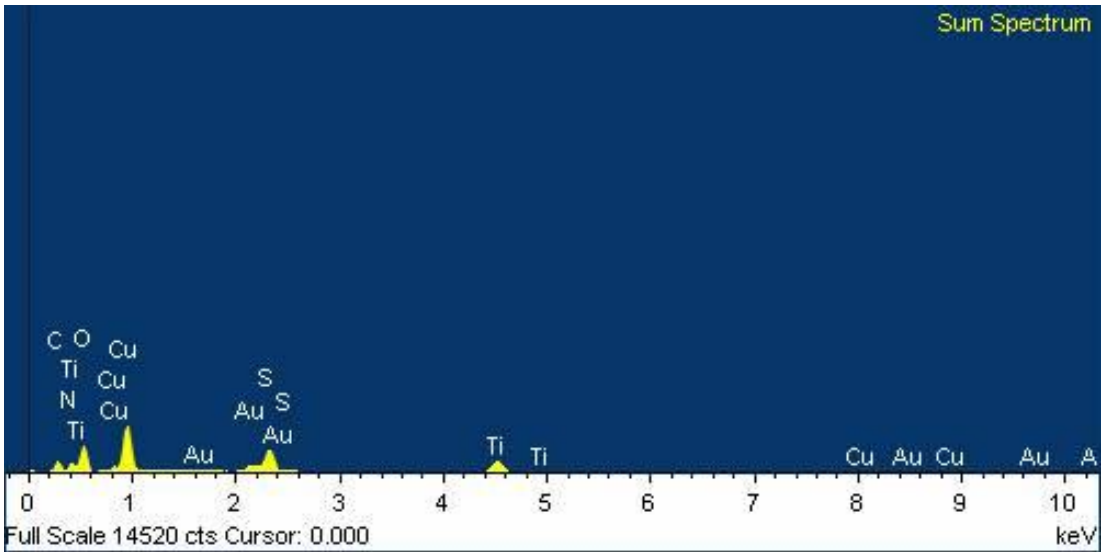

Figure 5-12: EDX scan of the region at the tube bottom in Fig. 5-11b near the nanotube/adhesive layer interface after CuSCN solution casting.

The difference in the degree of penetration when the same amount of CuSCN PS solution (40 drops, each drop ~1.8 µl) is applied to the titania nanotube membranes of various tube lengths is illustrated in Fig. 5-13. As seen from Fig. 5-13 (a, d, g), a ca. 2 µm CuSCN thick overlayer formed on the 5 µm nanotube membrane. Only a thin ~ 0.5 µm CuSCN overlayer is formed on 7 µm nanotube and there is no CuSCN overlayer visually detected on 10 µm nanotube. The results of the element mapping by EDX are displayed in Fig. 5-13, Cu and Ti is highlighted in yellow and red, respectively. The CuSCN penetration is discussed here based on the Cu mapping. For the 5 µm nanotube membrane, the TiO_2 tubes are essentially filled and there is a relatively thick CuSCN layer formation. The Cu mapping in Fig. 5-13 (b) is rather uniform along the nanotube length direction. For the 7 µm nanotube membrane, there is only a thin overlayer of CuSCN on top, indicated as a bright yellow ribbon in the Cu distribution map (Fig. 5-13e). This implies 40 drops of 1.8 µl CuSCN PS can just filled up the nanotube of 7 µm. Finally, a considerably weaker contrast in Cu

mapping for the nanotube of 10 µm shows that there is no overlayer formed in Fig.5-13h, i.e. all the CuSCN penetrated into the TiO_2 nanotubes. A rather complete filling may be assumed for the upper ca. 3 µm of the nanotubes only, while the gradual decrease in Cu concentration cannot only be traced back to the V-shape of the nanotube interior. Obviously the amount of CuSCN is not sufficient to ensure a complete filling of the nanotubes in this case, and the CuSCN also does not fill up the tubes from the bottom up to a certain level. Instead, it is spread on the nanotube walls and some of the CuSCN even reaches the bottom of the nanotubes.

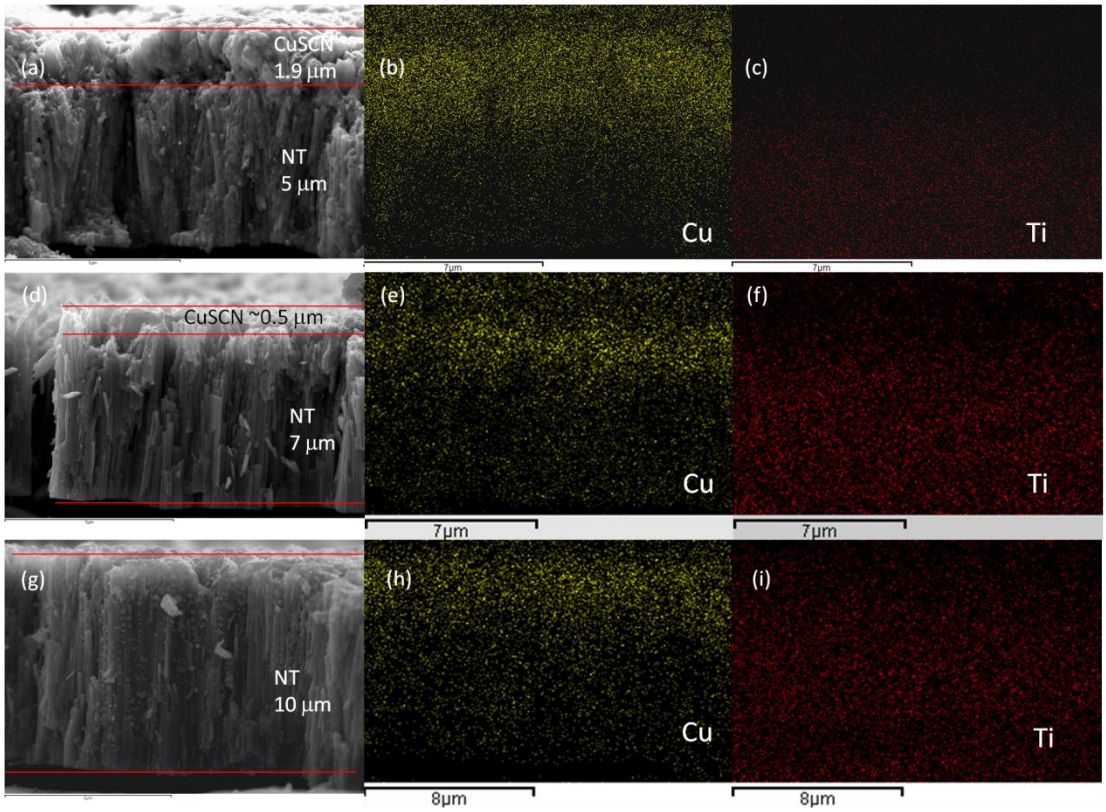

Figure 5-13: Side views of 40 drops of CuSCN solution cast into titania nanotube membranes of (a - c) 5 µm, (d - f) 7 µm or (g - i) 10 µm thickness: (a, d, g) SEM image; (b, e, h) Cu element scans; (c, f, i) Ti element scans.

The atomic ratio between Cu and Ti measured at the tube bottom is 1.09, 0.4 and 0.1 respectively in Fig. 5-13 (a, d, g). To assess the expected Cu/Ti atomic ratio for complete filling, the space filling for the packing of nanorods (outer diameter of nanotube) is taken as 70%, and the nanotube opening space is estimated by assuming an inner diameter to outer diameter ratio of 3/4 (neglect V-shape and estimate based on 90 nm/120 nm ID/OD for 1 h anodization at 50 V). Under these assumptions a complete filling would correspond to an atomic ratio between Cu to Ti of 1. The observed atomic ratio of 1.09 thereby indicates a practically complete filling for the 5 µm layer and the lower values for longer nanotubes indicate a gradual decrease in CuSCN penetration. Although 40 drops do not correspond to the optimized solution casting conditions for the 7 and 10 µm thick layers, we can still observe that the CuSCN penetration on elongated tube arrays is incomplete. Therefore, the ~ 7 µm thick layers seems to represent the optimum compromise between the increase of efficiency with increase of the surface area available for dye loading and the decrease by incomplete hole-conductor penetration and more prominent recombination processes.

5.3.5 Stability test and temperature effect

The stability of the SSDSC is another issue that requires further attention. Although there is no electrolyte leakage in this system, cell performance is often found to drop due to dye degradation or HTM oxidation after a few days. [13] Here, we present a stability test of both nanoparticle-based and nanotube-based SSDSC to investigate the

influence of the optimized casting solution and light illumination on stability and performance of the cell.

5.3.5.1 Nanoparticle SSDSC

The stability test of a SSDSC using 18T NP of 5 μm thick and CuSCN shows that a properly sealed cell can yield a lasting performance. The photovoltaic performance data presented in Fig. 5-14a is obtained by the first measurement on the respective day (i.e. without light soaking). On the 17th day, J_{sc} starts to climb with a slight decrease in V_{oc}. This observation can be tentatively explained as progressive drying of solvent as well as a moderate degree of oxidation. Oxidation of Cu^{+} to Cu^{2+} increases the hole concentration. [14] As a consequence both the hole conductance and the recombination process are promoted. This is in agreement with the observation from the Nyquist plots shown in Fig. 5-14d: fitting of the corresponding equivalent circuit models reveals that both charge transport resistance and recombination resistance shrink after illumination (compare fresh sample with sample on 27th day). This explains why an increase in J_{sc} after light soaking (due to higher conductance) is always accompanied by a decrease in V_{oc} (due to faster recombination).

The effect of light soaking has been monitored in detail by measuring a typical cell ten times consecutively on the 21st day. Results are shown in Fig. 5-14b. Since each measurement takes *ca.* 100 seconds, it effectively reveals the tendency of how photovoltaic performance changes over 16 min (the source meter typically scans from -0.1 V to 0.6 V, 100 pts recorded with 1000 ms as an interval) under practically

continuous illumination. In contrast to a previous literature report by O'Regan and Schwartz [13], we find that the cell performance (J_{sc} in particular) keeps increasing under illumination up to a plateau value. So it can be concluded that the HTM optimized and fabricated by our treatment method is highly stable under illumination.

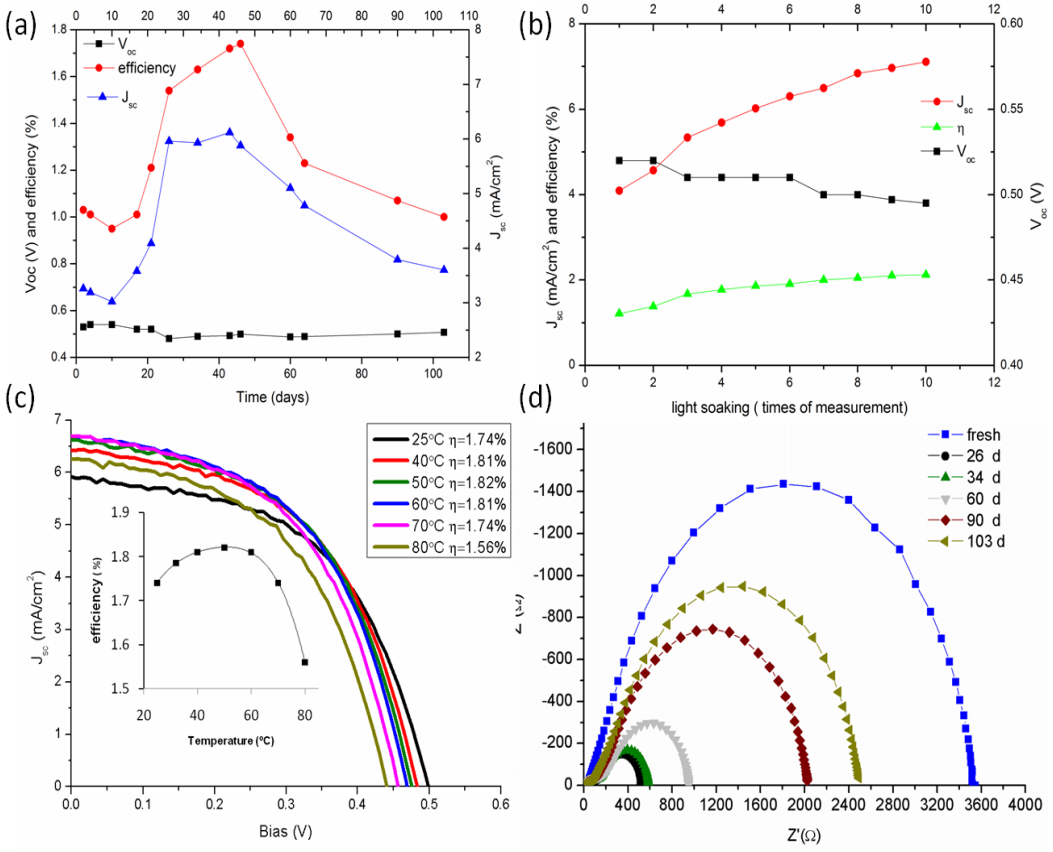

Figure 5-14: Photovoltaic performance of a nanoparticle-based SSDSC is summarized in stability test during 110 days in (a); Cell performance can be enhanced by light soaking, a typical example on 21st day in (b); Temperature effect on cell performance, a typical example measured on 46th day in (c); Impedance spectra in dark at V_{oc} are exhibited in (d). Samples were stored in a sealed petri-dish in an evacuated desiccator during 110 days, except for the duration of the tests.

To distinguish this light soaking from the effect of temperature on SSDSCs we also studied the latter separately. Results in Fig. 5-14c show that the optimum working condition for SSDSCs is in the range of 40~60 ℃. Since the temperature of the cell

after the above-mentioned continuous illumination experiment reached only 32 ℃, we can safely conclude that the observed performance improvement is mainly due to the light soaking and independent of the temperature effect in Fig. 5-14b. (That should only lead to a marginal relative enhancement by 3%).

Electrochemical impedance spectroscopy [15] in dark at V_{oc} is employed to monitor the cell stability. As seen in Fig. 5.14d, we find that the fresh cell shows the largest recombination resistance and hence the longest electron life time. This is in accordance with the highest V_{oc} measured (listed in Table 5-4). The subsequent reduction in both recombination and charge transport resistance can be linked to the accumulated effect of intense light illumination. If there are long time intervals in between illuminations, the effect seems to gradually diminish over time. From the 26^{th} day onwards, the recombination resistance gradually increases which corresponds to the increase of V_{oc} listed in Table 5-4 (A part of this increase may have been caused by the heat treatment on day 46, see below).

Table 5-4: Stability effect on the parameters obtained from J-V curve under illumination.

days	Efficiency (%)	V_{oc} (V)	J_{sc} (mA/cm^2)	FF (%)
2	1.03	0.53	3.26	56.7
4	1.01	0.54	3.19	52.8
10	0.95	0.54	3.02	53.2
17	1.01	0.52	3.58	52.3
21	1.21	0.52	4.09	50.9
26	1.54	0.48	5.96	48.2
34	1.63	0.49	5.93	50.5
43	1.72	0.49	6.12	51.2
46	1.74	0.50	5.88	51.5
60	1.34	0.49	5.10	48.5
64	1.23	0.49	4.78	47.3
90	1.07	0.50	3.79	50.1
103	1.00	0.51	3.60	49.5

The key photovoltaic parameters in stability test of the cell performance over 110 days are also summarized in Table 5-4. The highest efficiency is obtained when the measurement is taken on 46th day after assembly. Because achieving a reliable sealing of SSDSCs proved to be difficult (and is considered beyond the scope of this thesis) the few well-sealed samples are subject to various studies. Thus, the sample used for the long-term stability test is also used for the light soaking test on the 21st day and a temperature effect test on the 46th day. Although the trend of cell performance shown in Fig. 5-14 is not subject to stability alone, we still can conclude that our optimized Ni-doped CuSCN HTM is highly suitable and capable of long-term stable performance under outdoor conditions. (Both continued light illumination and temperature increase up to about 60 ℃ as to be expected on a rooftop boost the cell performance).

An analogous stability study for front-illuminated nanotube-based SSDSCs is discussed in the following section.

5.3.5.2 Nanotube SSDSC

In order to further improve the efficiency of nanotube-based SSDSCs via utilizing longer nanotube arrays, other than optimizing the composition of the casting solution (discussed in section 5.3.4), coating of a thin insulating layer is explored as a possible way to slow down the recombination process. To clear organic residues before dye-coating and facilitate better dye anchoring samples were exposed to UV light (Jelight 42-220 UVO cleaner, 28000 μW/cm^2 at 254 nm) for 1 min. To this end, the UV-treated sample is immersed in 100 mM aluminium tri-*tert*-butoxide IPA solution at

50 ℃ for 40 min. The sample is then rinsed by D.I. water and IPA. The cleaned sample is heated again at 450 ℃ for another 30 min. Similar to the finding by O'Regan [6], we observe that Al_2O_3 coating (by a treatment with concentrated 100 mM aluminium tri-*tert*-butoxide IPA solution) increases the open-circuit voltage while reducing the short-circuit current. Attempts with more diluted aluminium tri-*tert*-butoxide IPA solution did not reliably produce an Al_2O_3 coating. Since the objective of this study is mainly to study whether such an Al_2O_3 coating is effective in increasing the optimum length of FI-NT-SSDSC, only SSDSCs employing the 7 μm and 10 μm thick nanotube membranes are tested.

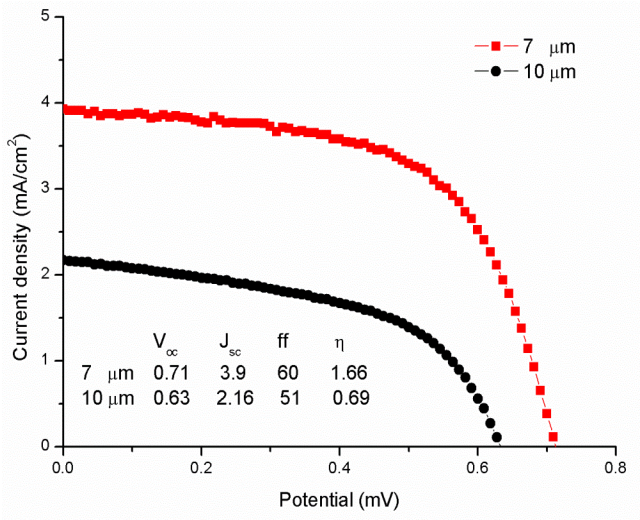

Figure 5-15: Length effect of nanotube-based SSDSCs treated 100 mM aluminium tri-*tert*-butoxide IPA solution. The measurement is conducted immediately after assembly under STC.

As seen in Fig. 5-15 the optimum nanotube length is still 7 μm after Al_2O_3 coating. While the coating is effective in the sense that V_{oc} increases, this cannot compensate the decrease in J_{sc}, so that overall efficiency drops from 1.86% to 1.66%. For a 10 μm nanotube-based SSDSC, the enhancement in V_{oc} due Al_2O_3 coating dominates so that the cell efficiency is slightly improved. (Compare Fig. 5-9 to Fig. 5-15,

efficiency increases from 0.62% to 0.69%) The aluminium tri-*tert*-butoxide IPA solution is vulnerable to moisture contamination that can result in inhomogeneous coating where thick coatings can block parts of the TiO_2 nanotubes. As the moisture level in Singapore is usually above 80%, it is inevitable to expose the stock solution to moisture. Therefore, the preparation of the stock solution should be conducted in a glove box. The concentration of the aluminium tri-*tert*-butoxide in IPA solution and the duration of the solution treatment control the morphology (or thickness) of Al_2O_3 coating layer together.

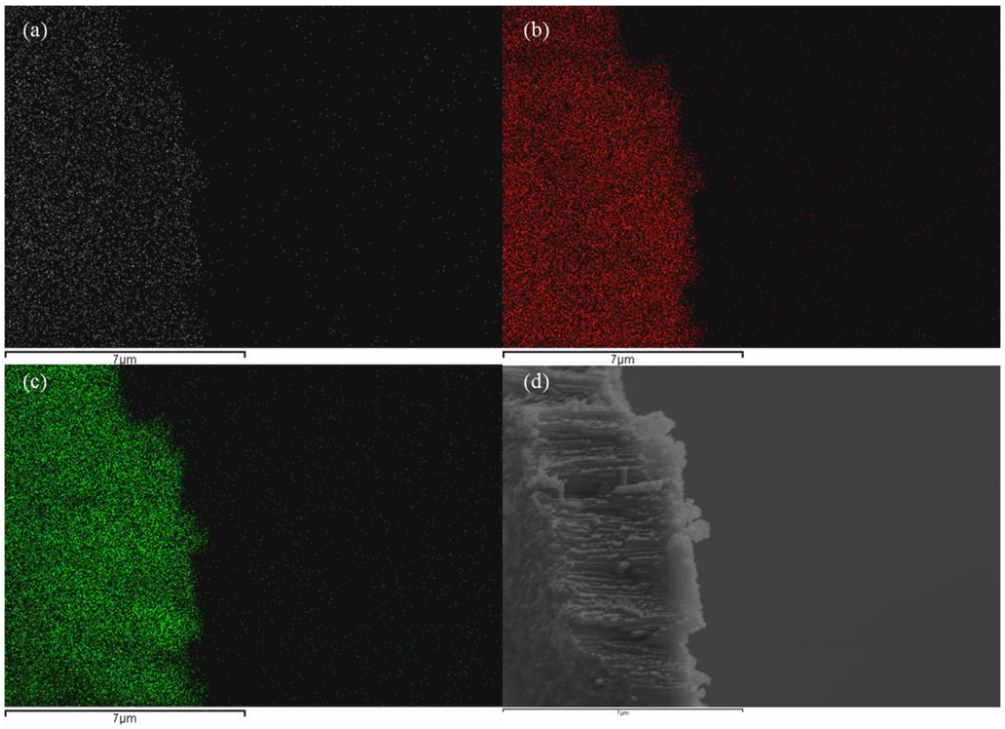

Figure 5-16: EDX elements mapping of Al_2O_3 coated nanotube arrays. The mapping pictures in (a): Al, (b): Ti and (c): O captures the element distribution in (d).

The morphology of Al_2O_3 coating is inspected in Fig. 5-16. The EDX mapping of the Al_2O_3 coated nanotube arrays reveals the atomic ratio between Ti and Al is 18:1. The coating appears to be evenly distributed along the tube length direction. Similar to Ti

and O distribution, the Al distribution also matches the outline of the nanotubes in the corresponding SEM micrograph Fig. 5-16d. However, a zoomed in picture in Fig. 5-17b shows that the coating is still segregated (as compared to Fig. 5-17a for TiO_2 without coating) and that TiO_2 nanotube is not uniformly covered. This implies that either the stock solution is still somehow contaminated by the moisture or the solution thermal treatment condition is not optimized. In future, optimization of coating a uniform thin layer of Al_2O_3 on TiO_2 is a topic worthy of study.

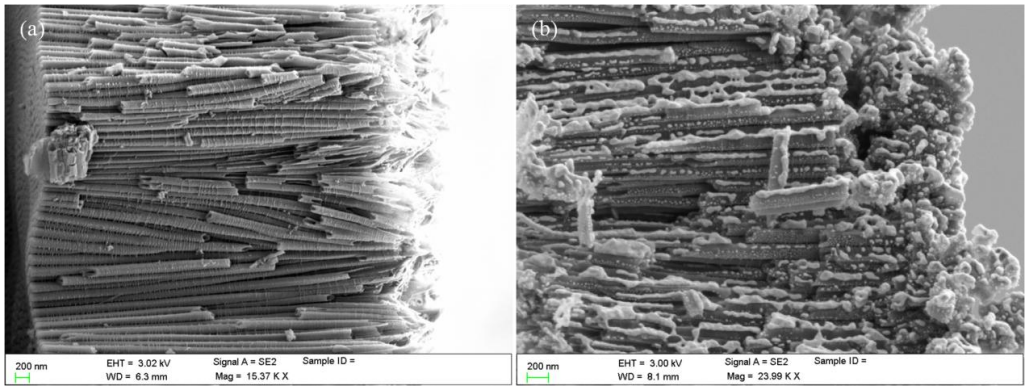

Figure 5-17: Side view of nanotube arrays by anodizing Ti foil for 1 h: before Al_2O_3 coating (a) and after Al_2O_3 coating (b).

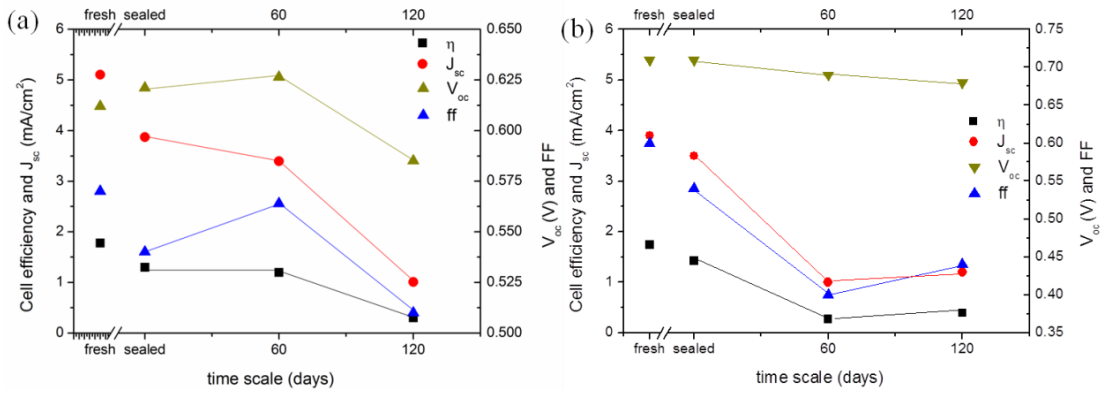

Figure 5-18: Stability test of 7 µm long nanotube-based SSDSCs over four months, the cell performance dropped after sealing. The cell without Al_2O_3 coating (a) is considered as stable over two months after seal; the performance Al_2O_3 coated cell (b) drops a lot in the first two months, it is probably due to non-uniform coating peeled off after two months.

A stability test of nanotube-based SSDSCs is presented in Fig. 5-18a comparing results for uncoated and Al_2O_3-coated nanotube membranes. After sealing the front-illuminated nanotube-based SSDSCs fabricated by our method show a stable efficiency for at least two months. The slightly reduced performance after sealing might be due to mechanical deformations during the curing of the epoxy. Thereafter the cell performance is reduced by only 7% over two months before an obvious degradation is observed over the following two month period.

The effect of Al_2O_3 coating on the cell stability is also illustrated in Fig. 5-18b. A drastic drop in cell performance is observed over the first two months, Since V_{oc}, J_{sc} as well as fill factor are all showing a large extent of decrease, the degradation mechanism is suspected to be different from the one for samples without Al_2O_3 coating. For fresh assembled SSDSC the effect of Al_2O_3 coating on cell performance is similar to an earlier report for nanoparticle-based SSDSCs, which did however not include a stability test [6].

The lower short-circuit current and higher open-circuit voltage for freshly-coated Al_2O_3-coated cells can be explained by the higher internal resistance and a higher recombination resistance as observed from the impedance spectroscopy results given in Fig. 5-19a. Accordingly, the electron life time in Al_2O_3 coated sample is longer (cf. Fig. 5-19b) which corresponds to its higher open-circuit voltage. The performance of a cell with Al_2O_3 coating is however not as stable as the cell without coating. Nyquist and Bode plots of the impedance measurement results for the cells with and without coating are shown in Fig. 5-19 (a, b), the corresponding plots for the cells after two months aging are shown in Fig. 5-19 (c, d). There is an enlarged high-

frequency arc and a slightly reduced low-frequency arc for aged nanotube-based SSDSC in Fig. 5-19c. The high frequency arc represents charge transport in CuSCN and low frequency arc represents charge recombination between electrons in TiO_2 and holes in CuSCN (see Fig. 2-13b).

So regardless of Al_2O_3 coating, the photovoltaic performances of nanotube-based solid-state dye-sensitized solar cells both suffers from a little bit of degradation over 2 months due to minor oxidation of CuSCN to $Cu(SCN)_2$ and dye degradation over time. The former increases the change of electron-hole recombination and the later adversely influence the light absorption. Volume shrinkage of CuSCN as a consequence of the solvent evaporation may reduce the contact between CuSCN and dye-coated TiO_2. The three effects mentioned result in a drop in V_{oc}, J_{sc} and fill factor respectively.

Al_2O_3-coated SSDSCs show a reduced stability over two months. Therefore, in addition to the above mentioned adverse effects that take place, the drop in all key photovoltaic parameters indicates that the non-uniform Al_2O_3 coating most likely peels off during the test (cf. Fig. 5-19b). This peeling off may be worsened by the drying of CuSCN. The photoelelectrochemically active dye-coated area shrinks as the dye-molecule anchored on the peeled off Al_2O_3 surface no longer contribute and CuSCN may come into direct contact with TiO_2, enhancing the recombination rate. As the bonding of the dye molecules on Al_2O_3 surfaces will be weaker than on TiO_2, there may additionally be a substantial detachment of dye molecules exposing the oxide surface to direct contact with HTM. During drying, remains of CuSCN propyl-sulfide solution will crystallize and the growth of the CuSCN may results in the direct

contact between HTM and TiO_2. This hypothesis is supported by the fact that V_{oc}, J_{sc} and FF all seem to decrease on a comparable timescale. Moreover, impedance plots in Fig. 5-19 harmonize with the hypothesis. An extra peak (red circle in Fig. 5-19d) located in the frequency range of about 100 Hz indicates a new charge transfer process taking place, which might corresponds to processes at the (bare) TiO_2/CuSCN interface. This provides a further indication for the proposed explanation as the electron life time of electrons transfer from bare TiO_2 to CuSCN should be shorter than the one from dye-Al_2O_3 coated TiO_2 to HTM.

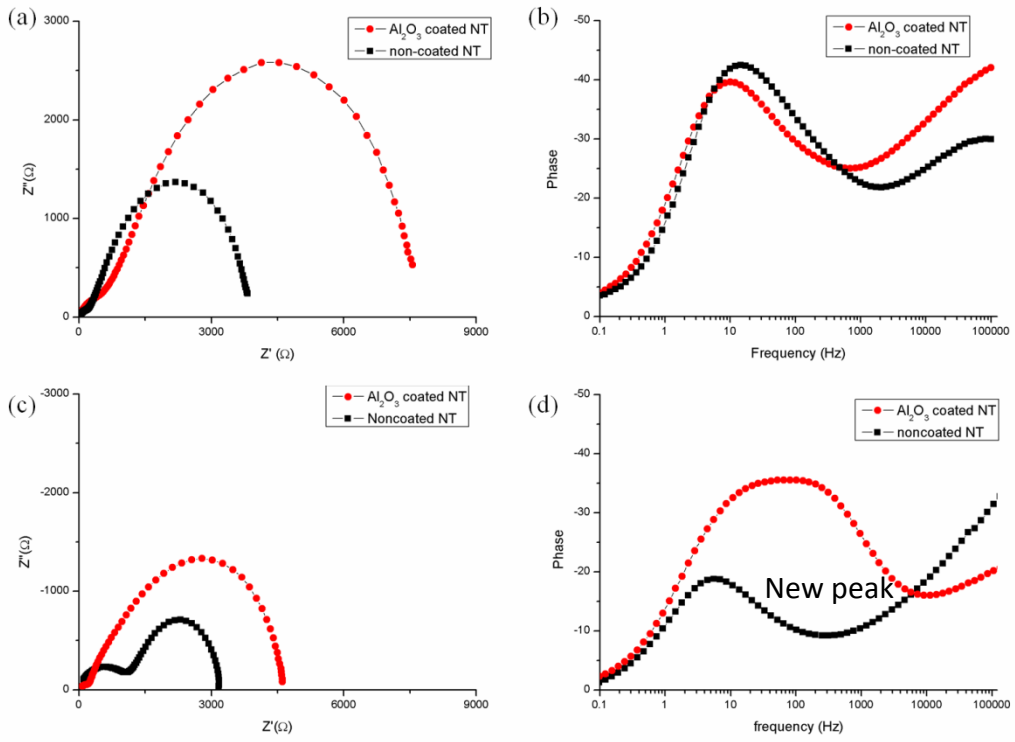

Figure 5-19: Al_2O_3 coating effect on impedance spectroscopy in dark of fresh 7 µm NT SSDSCs in (a: Nyquist plot, b: Bode phase plot) and Al_2O_3 coating effect on impedance spectroscopy in dark of 2 month aged 7 µm NT SSDSCs in (c: Nyquist plot, d: Bode phase plot). The measurement is conducted in dark at minus 500 mV.

In summary, both NP-based and NT-based front-illuminated SSDSCs are fabricated using $Ni(SCN)_2$ doped CuSCN. The photovoltaic performances of NT-based and NP-based cells of optimum thickness are comparable. NT cells show better promise as the optimum length of 7 μm is longer. A typical NP-cell was selected for stability test and found to be highly stable over the 46 days of performance monitoring: the efficiency started to increase after 17 days. The photovoltaic performance increases under light illumination, and the optimum working temperature of a SSDSC is ca. 50 ℃. The stability test of NT SSDSCs without Al_2O_3 coating is comparable to NP SSDSCs. This is the first report of the stability test of front-illuminated TiO_2 nanotube-based all-solid-state dye-sensitized solar cells. It shows a promising and long-lasting photovoltaic performance. The Al_2O_3 treated SSDSCs are not stable after the cell is assembled; this is tentatively explained as the peeling of Al_2O_3 coating layer which makes the TiO_2 directly exposed to CuSCN.

References

1 Q. B. Meng, K. Takahashi, X. T. Zhang, I. Sutanto, T. N. Rao, O. Sato, A. Fujishima, H. Watanabe, T. Nakamori and M. Uragami, Langmuir, 2003, 19, 3572.

2 B. Peng, G. Jungmann, C. Jager, D. Haarer, H. W. Schmidt and M. Thelakkat, Coordination Chem. Rev. 2004, 248, 1479.

3 L. Kavan, M. Grätzel, Electrochim. Acta 1995, 40, 643.

4 G. R. A. Kumara, A. Konno, K. Shiratsuchi, J. Tsukahara and K. Tennakone, Chem. Mater. 2002, 14, 954.

5 G. Kumara, A. Konno, G. K. R. Senadeera, P. V. V. Jayaweera, D. De Silva and K. Tennakone, Sol. Ener. Mater. and Sol. Cells 2001, 69, 195.

6 B. O' Regan, S. Scully, A. C. Mayer, E. Palomares and J. Durrant, J. Phys. Chem. B 2005, 109, 4616.

7 K. P. Sarma, R. K. Poddar, Transition Met. Chem. 1984, 9, 135.

8 E. V. A. Premalal, G. Kumara, R. M. G. Rajapakse, M. Shimomura, K. Murakami and A. Konno, Chem. Comm. 2010, 46, 3360.

9 V. P. S. Perera, M. K. I. Senevirathna, P. Pitigala, K. Tennakone, Sol. Ener. Mater. and Sol. Cells 2005, 86, 443.

10 K. L. Li, Z. B. Xie, S. Adams, Electrochimica acta 2012, 62, 116.

11 P. Chen, J. Brillet, H. Bala, P. Wang, S. M. Zakeeruddin and M. Grätzel, J. Mater. Chem. 2009, 19, 5325.

12 B. O'Regan, F. Lenzmann, F. Muis, R. Wienke, J. Chem. Mater. 2002, 14, 5023.

13 B. O'Regan, D. T. Schwartz, Chem. Mater. 1998, 10, 1501.

14 B. O'Regan, D. T. Schwarts, AIP Conf. Proc. 1997, 404, 129.

15 B. Mahrov, A. Hagfeldt, F. Lenzmann and G. Boschloo, Sol. Ener. Mater. and Sol. Cells 2005, 88, 351.

Conclusion

The fabrication of nanotube by anodizing a Ti foil in NH_4F containing ethylene glycol solution is optimized for the application of dye-sensitized solar cells. Experimental conditions such as electrolyte composition, electrolyte additive, applied potential, initial ramp rate, anodization duration are systematically studied and optimized. The charge transport rate of electrons in TiO_2 nanotubes is found to be at least one order larger than that in nanoparticular TiO_2. The fast charge transport can be correlated to the doping effect when TiO_{2-x} is introduced during anodization over time. An oxygen deficient region is created at the metal-oxide interface when the nanotube grows in length. The optimum anodization time and hence the optimum length of nanotubes is determined by the balance between the gain in electron transport rate due to a more pronounced oxygen deficiency x and the rise in recombination losses with nanotube length. The length effect of nanotube on DSC performance is studied to pinpoint this optimum thickness of 20 μm. The larger optimum thickness in the case of nanotube membranes when compared to nanoparticle layers is mainly due to the considerably faster electron transport rate. For back-side illuminated nanotube-based DSCs this leads to a light conversion efficiency of 4.6%.

In order to exploit the advantage of the nanotube structure, the front-illuminated cells design if favourable to solve the light-absorption issue of back-illuminated cells (where light needs to travel through counter electrode and the redox electrolyte system before being harvested). A reliable and highly reproducible method

is developed to produce and transfer nanotube arrays onto a transparent and conductive substrate for photovoltaic devices. The method is flexible to fabricate nanotube membranes with a wide range of thicknesses from 5 μm onwards. The range of transferable membranes that become available by this method matches with the desirable thicknesses required for both dye-sensitized solar cells using liquid electrolytes and all-solid-state dye-sensitized heterojunction cells. The mechanism of this reliable nanotube detachment method is studied in depth, leading to an efficient way to safely transfer high-quality membranes onto a variety of substrates such as quartz, Si or FTO. To demonstrate the feasibility of the method, front-illuminated nanotube-based dye-sensitized solar-cells using this method are realised and reach an efficiency of 6.3% with liquid electrolytes (of which at least 6.1% originate from the transferred membrane). The analysis of impedance spectra shows that the photovoltaic performance of the cells follows the same trend with respect to the ratio of recombination resistance over charge transport resistance.

Due to the unique tubular structure of titanium nanotube membranes produced by Ti foil anodization, they are highly suitable for fabricating all-solid-state dye-sensitized solar cells. Both conductivity and pore-filling of the hole transporting medium CuSCN is optimized by $Ni(SCN)_2$ doping, in combination with using α-CuSCN and THT as additives. 0.2 mM THT in a mixture of CuSCN, $Ni(SCN)_2$ and α-CuSCN propyl sulphide saturated solution (with 10 vol% propyl sulphide to dilute the stock solution before use) is found to be the most promising and reproducible composition for solution casting method in the application of solid-state DSC. When using this optimized solution, casting on a hotplate at 40 ℃ (i.e. at a much lower

temperature than previously suggested in the literature) is found to be highly reproducible and recommended for the penetration into active layer and slow nucleation of CuSCN on TiO_2. The optimum number of solution drops depends not only on the thickness but also on the mesostructure of the nanotube arrays. To produce the best front-illuminated nanotube-based SSDSCs (FI-NT-SSDSCs), 60 drops (each of 1.8 μl) of the optimised solution are deposited on the 7 μm nanotube membrane.

In order to understand the stability of the hole-transporting medium the photoelectrochemical performance of a range of SSDSCs is monitored over 4 months. The length effects on photovoltaic performance of both nanotube-based and nanoparticle-based fresh and aged cells are studied. Front-illuminated nanotube-based cells (1.8% under AM1.5 1 sun illumination) outperform the nanoparticles-based cells (1.1% under AM1.5 1 sun illumination) when the characterization is conducted immediately after cell assembly. The better performance is attributed to a longer optimum length of 7 μm with a higher light harvesting. Both nanotube and nanoparticles cells are compared also with respect to their long term stability. A typical nanoparticle-cell is found to be highly stable over the 46 days of performance monitoring: the efficiency started to increase after 17 days. The photovoltaic performance increases under light illumination, and the optimum working temperature of a SSDSC is ca. 50 ℃. The later gradual degradation over a subsequent 2 months period was mainly caused by exposing the cell to high temperatures during additional thermal aging tests conducted on day 46.

An analogous stability test of nanotube-based SSDSCs yields comparable results to nanoparticles-based SSDSCs over the first two months. Al_2O_3 coated nanotube-based SSDSCs are, however, found to be less stable; this is tentatively traced back to the peeling of Al_2O_3 coating layer which exposes the TiO_2 directly to CuSCN.

In summary, the method of fabricating high-performing and stable CuSCN based inorganic hole-transporting medium by solution casting method is optimized. Precise control over experimental conditions allows for a good penetration and suppressed nucleation of CuSCN. A reliable nanotube membrane transfer method is developed to fabricate front-illuminated nanotube-based dye-sensitized solar cells with promising light conversion efficiency. The application of the optimized CuSCN hole-transporting medium in front-illuminated nanotube-based solid-state dye-sensitized solar cells is proven to be highly stable both under light illumination and thermal aging for two months. Our front-illuminated nanotube-based all-solid-state dye-sensitized solar cell is a good demonstration of high-performance, highly-stable, and cost-effective photovoltaic device.

Future works

Although the front-illuminated nanotube-based solid-state dye-sensitized solar cells developed in this work are highly stable with promising photovoltaic performance, there is still a room for further optimization.

A better understanding is required why the optimum length of both back/front-illuminated nanotube-based dye-sensitized solar cells is limited even in cases where the charge collection efficiency of the cell remains close to 100% according to impedance data in dark. A new characterization method may have to be developed that permits an independent validation of the transmission line fitting model. A universally valid approach to monitor charge transport/transfer in DSCs both in dark and under illumination would be desirable. The optimum length limit can also be attributed to light absorption. Either a modification of film morphology on photoelectrode or an improvement of electrolyte transparency is needed to reduce light absorption in other cell components than the dye monolayer. Alternatively, other recombination protection layers than the investigated Al_2O_3 coatings may have to be explored to suppress the charge loss without adversely affecting short-circuit current and long term-stability of the cells.

Other than solution casting method, CuSCN can be electrodeposited into mesostructured TiO_2 to have a better filling and contact. Some preliminary experiments have been conducted in our group recently to explore electrodeposition of CuSCN using KSCN/$Cu(BF_4)_2$ in pure ethanol solution into titania nanotube. The deposited HTM fills the tube from bottom up and the thickness of filled layer is strongly correlated to the deposition time. However, the progressive slowing down of

the deposition when the nanotube layer is almost filled up may pose a problem for industrial application. As it takes a much longer time to form an overlayer of CuSCN on top of TiO_2, a combination between bottom-up electrodeposition with top-down solution casting method to balance the pore-filling and deposition time should be explored.

Another very important field for further work in SSDSCs is the choice and deposition of the sensitizers. Especially long time electrodeposition of dye-coated TiO_2 tends to cause a degradation or detachment of the sensitizing dye monolayer. A replacement of dye molecules by inorganic semiconductor quantum dots in all-solid-state solar cell system may be a promising strategy to address this issue. Optimized quantum dots may yield a higher extinction coefficient and exhibit an improved stability both during electrodeposition and during cell operation.

As the use of energy is more demanding nowadays, more clean and sustainable energy source are needed to benefit ourselves as well as protecting our planet. All-solid-state dye-sensitized solar cells attract a lot of attentions and more and more scientists are devoting themselves in this research topic. The results shown in this thesis demonstrate its great potential in both photovoltaic performance and stability. Among a variety of photovoltaic devices the work in this thesis and the work outlined above based on our findings shows that front-illuminated nanotube-based all-solid-state dye-sensitized solar cells have a strong potential to become a highly stable low-cost solution.

Publication list

Article in Journal:

K. L. Li, Z. B. Xie and S. Adams, "A reliable TiO_2 nanotube membrane transfer method and its application in photovoltaic devices". *ELECTROCHIMICA ACTA*, 2012, 62, 116-123.

K. L. Li, Z. B. Xie and S. Adams, "Fast charge transport of titania nanotube arrays in dye-sensitized solar cells". *ZEITSCHRIFT FUR KRISTALLOGRAPHIE*, 2010, 225, 173-179. (Germany).

K. L. Li, S. Adams, "Optimization of CuSCN Solution Casting for High Stability All-Solid-State Dye-Sensitized Solar Cells". *Nanoscience and Nanotechnology Letters*, 2012, 4, 750-755. (United States).

L. D. Sun, Md. A. Hossain, H. Yao, K. L. Li, S. Adams, Q. Wang, "Fabrication of TiO_2/CuSCN Bulk Heterojunctions by Profile-Controlled Electrodeposition". *Journal of the Electrochemical Society*, 2012 159(5): D323-D327.

Conference/Oral

K. L. Li, S. Adams, "High efficiency front-illuminated nanotube-based dye-sensitized solar cells". *Symposium GG: Titanium Dioxide nanomaterials*. Mater. Res. Soc. Symp. Proc., vol. 1352 (2011): DOI: 10.1557/opl.2011.1011. Pittsburgh: MRS. (Materials Research Society Spring Meeting 2011, 25 - 29 Apr 2011, San Francisco, United States) oral, published.

K. L. Li, Z. B. Xie and S. Adams, "Effect of Dye Monolayer Organization on Dye-Sensitized Solar Cell Performance". *Proc. E-MRS Fall 2010* (2010). Strasbourg: E-MRS. (E-MRS Fall 2010 Meeting, 13 - 17 Sep 2010, Warsaw, Poland) oral, published.

K. L. Li, Z. B. Xie and S. Adams, "Electron Transport in highly ordered anatase nanotube arrays for dye sensitized solar cells". *ICMAT 2009 & IUMRS ICA 2009* (2009) (ICMAT 2009 & IUMRS ICA 2009, 28 Jun - 3 Jul 2009, Singapore) oral, published.

K. L. Li, Z. B. Xie and S. Adams, "High efficiency dye-sensitized solar cells with ordered nanostructures". *ECSSC XII - XIIth European Conference on Solid State Chemistry* (2009) (ECSSC XII - XIIth European Conference on Solid State Chemistry, 20 - 23 Sep 2009, Muenster, Germany) oral, published.

Conference/Poster

K. L. Li, S. Adams, "Front-illuminated Nanotube-based Solid State Dye-sensitized Solar Cells". *Proc. of ICMAT 2011 Symposium M* (2011). Singapore: MRS-S. (International Conference on Materials for Advanced Technologies, 26 Jun - 1 Jul 2011, Suntec City, Singapore) poster, published.

K. L. Li, S. Adams, "Front-illuminated nanorod-based Dye Sensitized Solar Cell". *Proc. 4th MRS-S conference on Advanced Materials* (2010): 15. Singapore: MRS-S. (4th MRS-S conference on Advanced Materials, 17 - 19 Mar 2010, Singapore) poster, published.

R, Prasada Rao, K. L. Li, S. Krishnamoorthy and S. Adams, "Electrochemical performance of Nanostructured Li_2S/Silicon Rechargeable Batteries". *MRS-S Trilateral Conference on Advances in Nanoscience* (11 - 13 Aug 2010, IMRE, Singapore) presented, not published.

S. Adams, K. L. Li, Z. B. Xie, "Organisation of Anatase TiO_2 – Dye Solvent Interface and its Impact on the Performance of Dye-sensitized Solar Cells". *5th Asian Conference on Electrochemical Power Systems* (17 - 20 Sep 2010, NUS, Singapore) presented, not published.

K. L. Li, S. Adams, "Front-Illuminated Nanotube-Based Dye Sensitized Solar Cell". *5^{th} Asian Conference on Electrochemical Power Systems* (17 - 20 Sep 2010, Singapore) presented, not published.

S. Adams, K. L. Li, Z. B. Xie, "Dye Organisation on anatase surfaces and performance of Dye Sensitized Solar Cells". *6th Conference of the Asian Consortium on Computational Materials Science* (6 - 9 Sep 2011, Singapore) Accepted for poster presentation.

R, Prasada Rao, K. L. Li and S. Adams, "Anodized TiO_2 in rechargeable Lithium Batteries". *International Conference on Materials for Advanced Technologies* (26 Jun - 1 Jul 2011, Singapore) poster, published.

R, Prasada Rao, K. L. Li and S. Adams, Reddy M. V. and B V R Chowdari, "Electrochemical performance of anodized TiO_2 Nanotubes for rechargeable Lithium Batteries". *Materials Research Society* (25 - 29 Apr 2011, Moscone West Convention Center, San Francisco, United States) 122. Submitted.